

# Evidence of bimodal physical properties of intervening, optically-thin C III absorbers at $z \sim 2.5$

T.-S. Kim<sup>1,2\*</sup>, R. F. Carswell<sup>3</sup> & D. Ranquist<sup>2,4,5</sup>

<sup>1</sup>*Osservatorio Astronomico di Trieste, Via G. B. Tiepolo, 11, 34143, Trieste, Italy*

<sup>2</sup>*Department of Astronomy, University of Madison-Wisconsin, WI 53706, USA*

<sup>3</sup>*Institute of Astronomy, University of Cambridge, Madingley Road, Cambridge CB3 0HA*

<sup>4</sup>*Department of Astrophysics & Planetary Sciences, University of Colorado, Boulder, CO 80309, USA*

<sup>5</sup>*Department of Physics and Astronomy, Brigham Young University, Provo, UT 84602, USA*

Accepted; Received

## ABSTRACT

We present the Voigt profile analysis of 132 intervening C IV+C III components associated with optically-thin H I absorbers at  $2.1 < z < 3.4$  in the 19 high-quality UVES/VLT and HIRES/Keck QSO spectra. For  $\log N_{\text{C IV}} \in [11.7, 14.1]$ ,  $N_{\text{C III}} \propto N_{\text{C IV}}^{1.42 \pm 0.11}$  and  $\langle N_{\text{C III}}/N_{\text{C IV}} \rangle = 1.0 \pm 0.3$  with a negligible redshift evolution. For 54 C IV components tied (aligned) with H I at  $\log N_{\text{H I}} \in [12.2, 16.0]$  and  $\log N_{\text{C IV}} \in [11.8, 13.8]$ , the gas temperature  $T_b$  estimated from absorption line widths is well-approximated to a Gaussian peaking at  $\log T_b \sim 4.4 \pm 0.3$  for  $\log T_b \in [3.5, 5.5]$ , with a negligible non-thermal contribution. For 32 of 54 tied H I+C IV pairs, also tied with C III at  $\log N_{\text{C III}} \in [11.7, 13.8]$ , we ran both photoionisation equilibrium (PIE) and non-PIE (using a fixed temperature  $T_b$ ) Cloudy models for the Haardt-Madau QSO+galaxy 2012 UV background. We find evidence of bimodality in observed and derived physical properties. High-metallicity branch absorbers have a carbon abundance  $[\text{C}/\text{H}]_{\text{temp}} \geq -1.0$ , a line-of-sight length  $L_{\text{temp}} \leq 20$  kpc and a total (neutral and ionised) hydrogen volume density  $\log n_{\text{H, temp}} \in [-4.5, -3.3]$  and  $\log T_b \in [3.9, 4.5]$ . Low-metallicity branch absorbers have  $[\text{C}/\text{H}]_{\text{temp}} \leq -1.0$ ,  $L_{\text{temp}} \in [20, 480]$  kpc and  $\log n_{\text{H, temp}} \in [-5.2, -4.3]$  and  $\log T_b \sim 4.5$ . High-metallicity branch absorbers seem to be originated from extended disks, inner halos or outflowing gas of intervening galaxies, while low-metallicity absorbers are produced by galactic halos or the surrounding IGM filament.

**Key words:** cosmology: observation – intergalactic medium – quasars: absorption lines

## 1 INTRODUCTION

Observational constraints on the interaction between galaxies and their surrounding medium are important for improving our understanding of how galaxies obtain their gas supply, grow over cosmic times and enrich their surroundings. In the current standard, simplified  $\Lambda$ -CDM (cold dark matter) picture, the distribution of CDM grows hierarchically out of the initial density fluctuation by gravity, forming intersecting filamentary and sheet-like structures (Navarro et al. 1996; Bullock et al. 2001). The intergalactic medium (IGM), mostly consisting of hydrogen and helium, follows the underlying dark matter distribution. Eventually, the IGM cools down to form galaxies at the center of CDM halos located at the density peaks in the filamentary struc-

ture. In return, galaxies and quasars photoionise the IGM and eject processed materials into the halo and the IGM through galactic winds. Galactic winds enrich the IGM, suppress star formation in galaxies and heat the gas around them, while the intergalactic gas continuously falls into the CDM halos and the large-scale gaseous filaments. This ongoing process results in a complicated cosmic web of gas, galaxies and underlying CDM (Cen et al. 1994; Davé et al. 1999; Keres et al. 2005; Oppenheimer & Davé 2009; Steidel et al. 2010; Wiersma et al. 2010; Cen & Chisari 2011; van de Voort et al. 2011; Shen et al. 2013).

Observational constraints on the relationship between the properties of surrounding gas and galaxies thus provide important tests for models of structure formation, galaxy formation/evolution, and past and ongoing star formation. The IGM is a diffuse, warm photoionised plasma, and the properties we may infer are the physical gas density, temper-

\* E-mail: kim@oats.inaf.it

ature, metallicity and line-of-sight length. These properties as a function of impact parameters, the projected distance from a galaxy to the absorbing gas, are one of the observational goals in the IGM study. Nonetheless, even without time-intensive deep galaxy surveys around QSO sightlines to estimate impact parameters, obtaining the IGM gas properties is still in its own right well worthwhile to constrain theoretical predictions.

The IGM is well observed through rich absorption lines blueward the Ly $\alpha$  emission line in the spectra of background QSOs, therefore often referred as “absorbers” or “absorption lines”. The majority of these lines are due to the resonance line transition by diffuse intervening neutral hydrogen H I with the H I column density at  $\log N_{\text{H I}} \in [12, 17]^1$ , often referred as the Ly $\alpha$  forest regardless of its metal association. There is also a small contribution from metal transitions, which is mostly associated with H I absorbers at  $\log N_{\text{H I}} \geq 14$  (Cowie et al. 1995; Songaila 1998; Ellison et al. 2000). Due to its high temperature and a low density, the Ly $\alpha$  forest does not have in-situ star formation. Therefore, metals associated with the low-density forest should have been transferred from somewhere. The most promising candidate with the most abundant observational support is galactic-scale outflows driven by supernovae.

Bipolar galactic outflows are ubiquitous both at high and low redshifts (Strickland et al. 1998; Martin 2005; Shapley et al. 2006; Strickland & Heckman 2009; Rupke & Veilleux 2013). High- $N_{\text{H I}}$  systems with  $\log N_{\text{H I}} \geq 17$  are directly associated with intervening galaxies at both high and low redshifts (Bergeron 1986; Steidel & Hamilton 1992; Le Brun et al. 1997; Fynbo et al. 2010; Werk et al. 2013), while the association with galaxies of the Ly $\alpha$  forest is less clear (Wakker & Savage 2009; Rudie et al. 2013; Liang & Chen 2014). Despite the large scatter, absorption strengths of both H I and metals are anti-correlated with impact parameters (Lanzetta & Bowen 1990; Lanzetta et al. 1995; Chen et al. 2001; Wakker & Savage 2009; Steidel et al. 2010; Tumlinson et al. 2011; Bordoloi et al. 2014; Liang & Chen 2014). The H I gaseous halo is larger than metal-enriched halo, with the latter being about  $\sim 200$  kpc (Brooks et al. 2011; Cen & Chisari 2011; Shen et al. 2013). In addition, Bouché et al. (2012) found that their 11 Mg II absorber-galaxy pairs at  $z \sim 0.1$  follow a different absorption strength–impact parameter relation between the absorbers closer to the minor axis and the major axis, evidence of an outflow origin of Mg II absorbers. Similarly, Lehner et al. (2013) found a bimodal metallicity distribution in the 28 absorbers with  $\log N_{\text{H I}} \in [16.2, 18.5]$  at  $z < 1$  and interpreted the bimodality due to galactic winds and inflowing gas, respectively.

In general, cosmological numerical simulations have successfully reproduced the observations. They predict that bipolar outflows originated in the disk disperse a metal-enriched gas into the halo along the minor axis of star-forming galaxies at larger distance than the

major axis, since the interstellar medium (ISM) density in the disk is lower along the minor axis. When the line of sight passes through closer to galaxies, i.e. at small impact parameters, the absorption system has a higher metallicity, with more metal species at a wider range of ionisation states and greater absorption strengths including H I (Aguirre et al. 2001; Cen & Chisari 2011; van de Voort et al. 2011; Oppenheimer et al. 2012; Shen et al. 2013; Barai et al. 2013). These simulations also suggest that some fraction of metals escapes from halos of parents galaxies into the intergalactic space. The escaped metals become associated with low- $N_{\text{H I}}$  absorbers often at  $\geq 2$  virial radii, and even in the IGM filaments without any galaxies within 0.5–1 Mpc. The details of this process depend on when and where galactic outflows occur and how galactic outflows and infalling gas interact with each other.

For an absorbing gas produced by a single element, i.e. the majority of the IGM H I gas, there exists no robust observational constraint on the physical properties, except for an upper limit on the gas temperature from the absorption line width. When more than two elements having a very different mass display a similar profile with each other, implying they are produced by the same gas, the temperature and non-thermal motion of the gas can be directly estimated from comparing their absorption line widths. When there exist more than 2 ionic transitions from the same metal element, such as C IV, C III and C II, a simple assumption on the ionisation mechanism such as photoionisation and collisional ionisation can be applied to derive other gas properties, if a radiation field to which absorbers are exposed can be provided. Note that only a range of the carbon abundance can be estimated from the photoionisation assumption if only H I and C IV are available.

The most commonly used tracer of metals associated with the Ly $\alpha$  forest is C IV doublet  $\lambda\lambda 1548.204, 1550.778$  (Cowie et al. 1995; Schaye et al. 2003)<sup>2</sup>, since its rest-frame wavelength longer than H I Ly $\alpha$   $\lambda 1215.670$  places C IV redward the Ly $\alpha$  emission line of the QSO, free of the forest H I blends. Although C II  $\lambda 1334.532$  can be outside the Ly $\alpha$  forest, it is usually detected with high- $N_{\text{H I}}$  absorbers (Cowie et al. 1995; Boksenberg & Sargent 2015). While C III  $\lambda 977.020$  is commonly found for low- $N_{\text{H I}}$  absorbers, its much shorter rest-frame wavelength often locates it in the wavelength regions severely contaminated by high-order H I Lyman lines and of less reliable continuum placement.

The observational difficulty to detect C III and a lack of C II of the forest H I often leave C IV the sole metal ion used to infer the physical structure of the low- $N_{\text{H I}}$  forest. The carbon abundance based on the H I and C IV profile fitting at  $\log N_{\text{H I}} \geq 14.5$  has been estimated to be  $\sim 10^{-2.5}$  solar with a large scatter in photoionisation equilibrium (PIE) (Cowie et al. 1995; Hellsten et al. 1997; Rauch et al. 1997; Simcoe et al. 2004). On the other hand, the statistical pixel optical depth analysis of H I and C IV probing lower- $N_{\text{H I}}$

<sup>1</sup> The logarithmic value of a quantity  $Q$  is expressed unitless as being divided by its unit before converted into the logarithmic value, such as  $\log N_{\text{H I}} = \log(N_{\text{H I}}/\text{cm}^{-2})$ . When the unit is noted for clarity, it is listed inside the bracket.

<sup>2</sup> While the most abundant cosmic metal element is oxygen, the O VI doublet  $\lambda\lambda 1031.926, 1037.616$  occurs inside the dense forest region, therefore it is difficult to detect a clean O VI associated with low- $N_{\text{H I}}$  absorbers at  $z \sim 3$ . In addition, no other transitions of oxygen such as O IV  $\lambda 787.711$  are covered at  $z \sim 3$  in the ground-based optical spectra.

ends than the profile fitting analysis estimates that the median forest carbon abundance is  $\sim 10^{-3.5}$  solar with a over-density and  $z$  dependence (Schaye et al. 2003).

Theories indicate that C IV associated with the forest is produced by a radiatively cooling non-equilibrium gas once shock-heated by supernovae-driven galactic outflows and/or hot stars, and that it is now exposed to the external UV background radiation produced by QSOs and galaxies (Wiersma et al. 2009; Cen & Chisari 2011; van de Voort et al. 2011; Oppenheimer & Schaye 2013). When an initially hot gas cools radiatively below  $\sim 10^{6.7}$  K, the gas is no longer in collisional ionisation equilibrium (CIE) and it remains over-ionised due to cooling occurring faster than recombination. Presence of radiation to a radiatively cooling non-CIE gas reduces a gas cooling rate at the gas temperature  $T \sim 10^4 - 10^5$  K by a large factor, which changes the thermal and ionisation states of the gas (Wiersma et al. 2009; van de Voort et al. 2011; Oppenheimer & Schaye 2013). By comparison, for a low-density gas in CIE without any external radiation, C IV peaks at  $T \sim 10^5$  K. The ionisation fraction of a given metal element is only a function of the gas temperature and the ratio of C III and C IV is about 1 at  $T \sim 10^5$  K (Gnat & Sternberg 2007). For a low-density PIE gas, the C IV fraction rapidly increases from  $T \sim 10^{5.4}$  K to  $T \sim 10^{4.9}$  K, then becomes rather independent of  $T$  at  $T \leq 10^{4.9}$  K. The ratio of C III and C IV is  $\sim 1$  at  $T \sim 10^{4.2} - 10^{5.0}$  K (Oppenheimer & Schaye 2013).

Here we present the results from a detailed Voigt profile analysis and photoionisation modelling of optically-thin H I absorbers associated with C IV and C III at  $2.1 < z < 3.4$ . The selected C IV components have  $\log N_{\text{C IV}} \in [11.7, 14.0]$ , which is a much lower  $N_{\text{C IV}}$  range than the galaxy-galaxy pairs study by Steidel et al. (2010) at  $z \sim 2.3$ ,  $\log N_{\text{C IV}} \geq 13.5$  and most studies based on the absorption strength-impact parameters. Being optically thin, i.e.  $\log N_{\text{H I}} \leq 17.2$ , these C III-selected absorbers do not require any complicated radiative transfer effect as is the case for optically thick Lyman limit absorbers. Comparing the predicted column densities based on photoionisation modelling with the observed ones enables us to test the basic assumption on the IGM physics such as photoionisation and hydrostatic equilibrium. It also provides a more robust estimate of the predicted physical properties of the C IV-enriched low- $N_{\text{H I}}$  gas, which is less well constrained observationally and can shed a light on the enrichment mechanism in the low-density universe. We have found evidence that optically-thin H I absorbers aligned (or tied in the profile fitting analysis to be specific) both with C IV and C III can be classified into two populations as high- and low-metallicity branch absorbers at the boundary of carbon abundance of one tenth of solar. Each branch follows its own different scaling relation between various observed and derived physical parameters.

This paper is organised as follows. Section 2 describes the sample, and gives details of the Voigt profile fitting analysis. The direct observables of the C III absorbers including the gas temperature are presented in Section 3. The extensive photoionisation modellings are summarised in Section 4, using the photoionisation code Cloudy version c13.03 (Ferland et al. 2013). The main findings on bimodality in observed/derived physical parameters of optically-thin

**Table 1.** Analysed QSOs

QSO	$z_{\text{em}}^{\text{a}}$	$z_{\text{C III}}^{\text{b}}$	S/N <sup>c</sup>	Inst.
Q0055–269	3.656	2.663–3.390	32, 53, 20	UVES
PKS2126–158	3.280	2.669–3.208	90, 168, 61	UVES
HS1425+6039	3.180	2.865–3.110	85, 68, 15	HIRES
Q0636+6801	3.175	3.000–3.105	70, 70, 7	HIRES
Q0420–388	3.115	2.850–3.045	120, 120, 52	UVES
HE0940–1050	3.082	2.776–3.014	80, 110, 52	UVES
HE2347–4342	2.873	2.257–2.710 2.770–2.809	100, 96, 50	UVES
HE0151–4326	2.781 <sup>d</sup>	2.180–2.710	81, 150, 45	UVES
Q0002–422	2.768	2.159–2.705	87, 137, 38	UVES
PKS0329–255	2.704	2.248–2.643	39, 70, 20	UVES
Q0453–423	2.657	2.136–2.595	65, 115, 20	UVES
HE1347–2457	2.612 <sup>d</sup>	2.135–2.552	69, 83, 30	UVES
Q0329–385	2.435	2.151–2.378	45, 75, 13	UVES
HE2217–2818	2.413	2.128–2.355	86, 120, 11	UVES
Q0109–3518	2.405	2.149–2.348	68, 139, 22	UVES
HE1122–1648	2.404	2.162–2.346	118, 227, 15	UVES
HE0001–2340	2.264	2.144–2.211	96, 74, 11	UVES
PKS0237–23	2.222	2.122–2.167	138, 169, 13	UVES
PKS1448–232	2.219	2.122–2.168	77, 122, 7	UVES

<sup>a</sup> The redshift is measured from the observed Ly $\alpha$  emission line of the QSOs.

<sup>b</sup> Only the region with  $S/N \geq 5$  per pixel is analysed.

<sup>c</sup> The first, second and third number is the S/N per pixel in the central parts of the analysed Ly $\alpha$  forest, C IV and C III regions, respectively.

H I+C IV+C III absorbers are presented and discussed in Sections 5 and 6, and summarised in Section 7.

## 2 QSO SAMPLE

### 2.1 Data

A total of 19 QSO spectra were used to search for C III, with the 17 spectra taken with the UVES on the VLT and the remaining 2 spectra with the HIRES on Keck. These spectra were chosen from the larger sample analysed in Kim et al. (2015), to include only the spectra covering a longer wavelength region useful for the C III search. The Kim et al. (2015) sample was chosen to study the low-density IGM, i.e. containing no strong damped Ly $\alpha$  systems and not many Lyman limit systems in one sightline, from the UVES and HIRES archives and includes only the QSO spectra with the high signal-to-noise ratio (S/N) and the long, continuous wavelength coverage to cover high-order H I Lyman series. The details on the data treatment can be found in Kim et al. (2015).

The resolution is  $\sim 6.7 \text{ km s}^{-1}$  (or  $R \sim 45,000$ ) and the wavelength is in the heliocentric velocity frame. To avoid the proximity effect, wavelength regions within  $5000 \text{ km s}^{-1}$  of the QSO Ly $\alpha$  emission line were excluded in each case. No further exclusion was done, e.g. in the regions near a sub-damped Ly $\alpha$  absorber. As the C III rest-frame wavelength  $977.020 \text{ \AA}$  is around Ly $\gamma \lambda 972.536$ , it is located in the shorter wavelength region usually having a lower S/N. Therefore, only the wavelength region with  $S/N \geq 5$  per pixel was

included in the C III search. Table 1 gives the basic properties of the spectra and the redshift range searched for C III. For the rest of this study, the listed S/N is per pixel. All the atomic wavelengths are in the rest frame, unless stated otherwise.

## 2.2 Voigt profile fitting

### 2.2.1 Basic assumptions

The most physically useful approach where high resolution, high S/N spectra of QSOs are available is to decompose absorption profiles into several discrete components, assuming Voigt profiles for each component. The profile fitting analysis provides redshifts, column densities in  $\text{cm}^{-2}$  and line widths in  $\text{km s}^{-1}$  (as the Doppler parameter or the  $b$  parameter). For a Maxwellian velocity distribution, the  $b$  parameter ( $= \sqrt{2}\sigma$ , where  $\sigma$  is the standard deviation) is related to the temperature and the non-thermal motion of the gas:

$$b^2 = \frac{2kT}{m_M} + b_{\text{nt}}^2, \quad (1)$$

where  $k$  is the Boltzmann constant,  $T$  is the thermal gas temperature in K,  $m_M$  is the atomic mass of the element M and  $b_{\text{nt}}$  is the Gaussian non-thermal line width in  $\text{km s}^{-1}$ . The thermal line width is  $b_{\text{th}}^2 = 2kT/m_M$ . When two different elements give rise to lines which have a similar profile shape and so the absorbing material in which they arise is probably co-spatial, Eq. 1 can be used to estimate a thermal and non-thermal contribution in the gas motion (Carswell et al. 2012; Dutta et al. 2014).

### 2.2.2 The search and the profile fitting of C III $\lambda$ 977

To search for C III  $\lambda$  977 and to measure the line parameters, we used the same line lists of 19 QSOs analysed by Kim et al. (2015). These lists are complete in the redshift range for which high-order Lyman lines of higher- $z$  H I absorbers affect the C III region of interest. In order for further physical analysis to be meaningful, such as photoionisation modelling, C III and C IV have to be produced in the same gas cloud. We assumed that the ion components having the same velocity structure are co-spatial.

For every C IV component associated with optically-thin H I, we searched for narrow lines at the expected C III  $\lambda$  977 positions based on the velocity structure of C IV. If the expected C III candidates occur inside saturated lines or are severely blended with other lines, these C III candidates were discarded. Only when C III candidates are clean and/or blends around the candidates can be securely estimated from other identified and fitted lines, these were flagged as potential C III components. This means that all the C III components corresponding to a multi-component C IV absorber are not necessarily clean. Even when part of multi-component C III profiles is clean, the line parameters of clean components could be still obtained and useful.

The C III candidates were then re-fitted with VPFIT version 10.2 (Carswell & Webb 2014), using its default rest-frame wavelengths and the oscillator strengths. To satisfy a condition of being co-spatial, when the C III and C IV components have similar redshifts (within  $1.5 \text{ km s}^{-1}$  of each

other), their redshifts and Doppler parameters were constrained to be the same. For velocity differences larger than that value, it was not generally possible to get good fits for sharp lines if the redshifts were constrained in that way.

The redshifts and Doppler parameters of any H I components clearly corresponding to C III and C IV within  $15 \text{ km s}^{-1}$  were also tied to their values, but for H I the Doppler parameter was constrained so that the temperature  $T \geq 0$  and  $b_{\text{nt}} \geq 0$  (see Eq. 1). Note that tying one H I component with the corresponding C IV sometimes significantly changes the line parameter of other nearby, tied/untied H I components in multi-component H I absorbers, i.e. a consequence of the Voigt profile fitting results not being unique, nor objective (Kirkman & Tytler 1997; Kim et al. 2013). In addition, not all H I components within  $15 \text{ km s}^{-1}$  from C IV can be tied successfully. Where an appropriate H I component is measured, the best-fit values of  $T$  and  $b_{\text{nt}}$  were determined by VPFIT. The value  $15 \text{ km s}^{-1}$  was adopted for similar reasons to the C III/C IV difference limit. It is larger here because the H I lines are almost invariably broader than both the C IV and C III lines, and generally have a larger redshift error (the median is  $\sim 8 \text{ km s}^{-1}$ ). If a single H I component is aligned with a C IV component within  $15 \text{ km s}^{-1}$ , but there are another nearby, strong C IV components within the associated H I line width, then it is not physically meaningful to include more H I components to be associated to all the C IV components. Therefore, we did not tie H I and C IV in this case.

During the fitting process the continuum level was adjusted as necessary to obtain a good fit to the data. The non-zero flux level of saturated lines often shown in the UVES spectra was also taken into account. This line-fitting-and-continuum-adjustment iteration was repeated until a satisfactory fit was achieved with the normalised  $\chi^2 \lesssim 1.3$ .

In addition to C III  $\lambda$  977, a search was made for corresponding C II  $\lambda\lambda$  1334.532, 1036.336. When detected these were fitted in the same way as the C III line. This generally gave only upper limits to the C II column density for systems where the Lyman limit is optically thin.

The detection limit for any line depends on the local S/N and the  $b$  parameter. For C III  $\lambda$  977, it is more complicated since C III is located in heavily blended regions with an uncertain continuum placement. Therefore, we use a lower-end  $N_{\text{C III}}$  of fitted C III components as a representative detection limit, though because of blending with Lyman forest lines the real limit will be higher in some individual cases. As for C II, we take the median upper limit of C II in absorption-free C II regions, as a majority of our C IV+C III pairs are not associated with C II. Representative detection limits are  $\log N_{\text{H I, lim}} \sim 12.5$ ,  $\log N_{\text{C IV, lim}} \sim 11.8$ ,  $\log N_{\text{C III, lim}} \sim 11.7$  and  $\log N_{\text{C II, lim}} \sim 12.0$ , although occasionally lower column density systems are found in high S/N regions.

## 2.3 Description of the C III sample

### 2.3.1 Examples of C III absorbers

Figure 1 presents a velocity plot (the relative velocity  $v$  versus the normalised flux) of four C III absorbers in our sample. The left panel shows a clean, *certain* C III absorber whose component structure is the same as the one of H I and C IV. The second panel illustrates an *uncertain* C III component

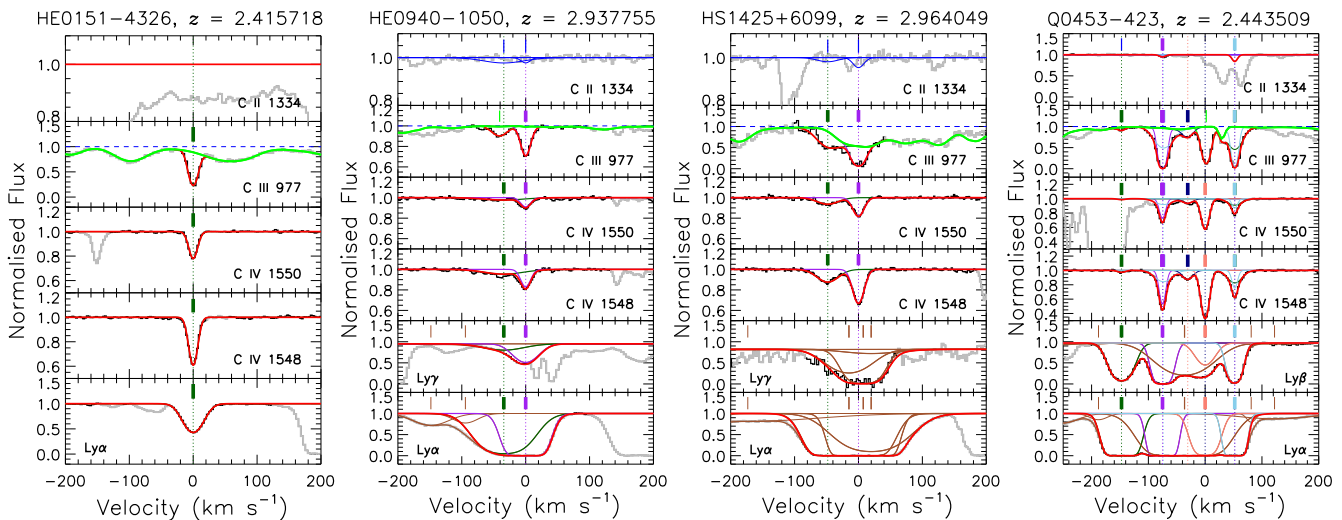


**Figure 1.** The relative velocity  $v$  versus normalised flux of 4 C III absorbers. The zero relative velocity is set to be at the C IV flux minimum, which is also set to be the redshift of a C III absorber. The redshift and the QSO name are listed on top of each panel. The black histogram is the observed spectrum, while the coloured, smooth profile is the generated profile from the fitted line parameters. The centroid of each components marks with thick vertical ticks. Thick ticks of a same colour indicate the tied components. The blue-coloured smooth profile indicates upper limits. Uncertain C III components are indicated with a thin green tick. The thin brown H I profile indicates an individual H I component near the region of interest, while the thick brown H I profile is the absorption profile from all the shown H I components. Metal lines are not shown to make a plot less complicated. The thick red H I profile delineates only the H I components in the velocity range covered by C IV and C III in the plot. The thick green curve in the C III panel shows the *working* continuum used in the VPFIT C III fit. This is a combination of the final continuum, high-order Lyman lines, Lyman limit continuum depression and metal lines, while in some cases H I Ly $\alpha$  near the expected C III is also included in order to remove a contribution of its broad wing, but never on top of C III. *Left panel:* a certain, clean C III absorber. The redshift and line width of H I, C IV and C III are tied. This absorber is suitable for the photoionisation modelling. *Second panel:* C III at  $v = 0$  km s $^{-1}$  has the same velocity structure with H I and C IV at  $v = 0$  km s $^{-1}$ . However, C III at  $v = -41$  km s $^{-1}$  is shifted by  $7 \pm 11$  km s $^{-1}$  from C IV at  $v = -34$  km s $^{-1}$  and has a narrower  $b$ . *Third panel:* C III is blended with other absorptions. Since the absorption from high-order Lyman lines is well constrained, indicated with the dark green profile, C III in red profile is also reasonably well measured. *Fourth panel:* the C IV absorptions at  $v = -75$ , and  $+52$  km s $^{-1}$  display a narrow component on top of a much broader component, while H I at the same relative velocity does not suggest the same component structure. The narrow C IV component was assigned to the seemingly single H I component. Refer to the online version for clarity.

at  $v = -41$  km s $^{-1}$ . It is shifted by  $7 \pm 11$  km s $^{-1}$  from the certain C IV at  $v = -34$  km s $^{-1}$ . The large velocity difference and the different profile shape suggests that the component at  $v = -41$  km s $^{-1}$  is not likely to be C III. Even if its identification is correct, the velocity shift implies that C III and C IV are not produced by the same gas, thus not suitable for the photoionisation modelling to derive any physical parameters. The third panel illustrates a C III absorber blended with high-order Lyman lines. The thick green profile indicates the contribution from the blended lines by high-order H I lines and identified metal lines. The red profile delineates the entire C III absorption profile around the region. As blending in this case is well constrained from the high-order H I fit including all the identified metal lines, the C III line parameters are also reasonably well measured.

The fourth panel of Fig. 1 shows an example of two C IV components at the same relative velocity. The C IV absorption at  $v = +52$  km s $^{-1}$  displays a narrow component on top of a much broader component. On the contrary, the H I component at the same relative velocity does not indicate the same two-component structure. At  $v = +52$  km s $^{-1}$ , the broader C IV  $b$  parameter is 16.6 km s $^{-1}$ , while the single H I  $b$  parameter is 13.0 km s $^{-1}$ . For a gas producing both H I and C IV absorptions under the same gas physical condition, a

C IV  $b$  parameter cannot be larger than a H I  $b$  parameter. A thermally broadened H I produced by the same C IV gas with  $b_{\text{C IV}} = 16.6$  km s $^{-1}$  should have  $b_{\text{H I}} = 57.5$  km s $^{-1}$ .

Interestingly, the opposite type of absorption profile occurs occasionally at lower redshifts where blending is negligible so that the component structure can be seen more clearly. For example, the  $z = 0.22601$  O VI absorber toward HE0153-4520 has a narrow H I component on top of a broader component, with the latter being associated with a single, broader O VI (Savage et al. 2011). If the overall physical conditions of metal-enriched intervening gas does not change significantly with redshifts, in the case of our C III absorber, a strong blending in H I could have caused us to miss any broader H I coexisting with the broader C IV component. However, the current data do not require a broader H I. Here the narrow C IV component was assigned to the apparent, single H I component. Similarly, the C IV absorption at  $v \sim -75$  km s $^{-1}$  has the narrow and broader components almost on top of each other. The velocity difference is only  $2 \pm 2$  km s $^{-1}$ , so forcing them to have the same redshift is easily possible. Again, the narrow C IV component was tied with the apparent, single H I component.

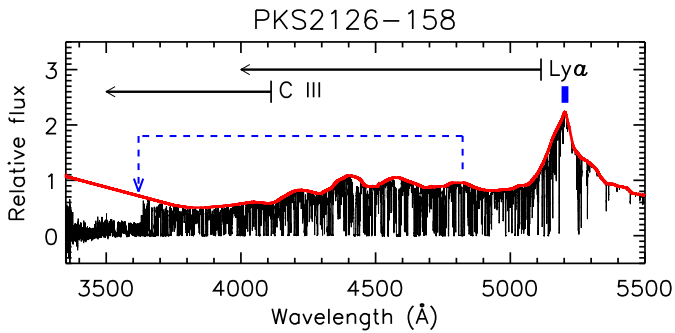


**Figure 2.** The wavelength vs the relative flux of PKS2126–158. The overlaid red curve is the final continuum, which was extrapolated at  $\leq 3466$  Å. The top arrows indicate the useful wavelength ranges for C III and H I. For H I we exclude the proximity effect zone within  $5,000 \text{ km s}^{-1}$  of the Ly $\alpha$  emission, which is indicated with the tick blue vertical tick at  $5203$  Å. C III corresponding to H I is then at  $\leq 4112$  Å. In this object several high- $N_{\text{H I}}$  absorbers depress the continuum of the QSO blueward their observed Lyman limit. Blue dashed line illustrates one such absorber at  $z \sim 2.967$ , shown with a vertical line at Ly $\alpha$  connected to the downward arrow at the Lyman limit depression at  $\sim 3622$  Å.

### 2.3.2 Selecting the clean C III components

C III  $\lambda 977$  is a single line which falls in the Ly $\alpha$  forest region. Consequently, a careful choice of C III components is required to compile a sample where the Lyman forest contamination is less severe, and so reliable C III line parameters may be determined.

(i) Figure 2 is an example where the C III is in a wavelength region where the continuum of the background QSO is depressed due to Lyman continuum absorption from high-column density H I systems. The continuum placement around C III regions below such depressions is difficult to determine and is unreliable. If the continuum placement around the C III region is highly uncertain despite the available high-order Lyman lines, these C III components were discarded.

(ii) Any C III component displaying a velocity difference larger than  $1.5 \text{ km s}^{-1}$  from the corresponding C IV component was classified as uncertain and not used in the analysis. The velocity difference could be caused by many things, such as inaccurate wavelength calibration in the low-S/N C III region, incorrect identification or unrecognised weak blending. It can also be due to a physical origin such as the C IV-producing gas not being co-spatial with the C III-producing gas, e.g. if C IV is produced in the outer transition region of a hot-temperature gas cooling rapidly and C III is in a cool, dense core. With the excellent wavelength calibration of UVES and HIRES spectra within  $1 \text{ km s}^{-1}$  uncertainty, inaccurate wavelength calibration is not a likely cause.

(iii) When there exists no obvious absorption in the expected C III position, upper limits were calculated, following the procedure described in Jorgenson et al. (2014). C III components with upper limits were included in the further analysis.

(iv) Fitted C III components were also checked for saturation, based on the flat-bottomed core of a line profile. We note that  $N_{\text{C III}}$  of a flat-bottomed-core profile is not necessarily a lower limit, as VPFIT looks for a best-fit  $N_{\text{C III}}$ , un-

like the apparent optical depth analysis (Savage & Sembach 1991). However, when a C III component has a boxy shape, we note its  $N_{\text{C III}}$  as a lower limit.

(v) Since C IV is usually found in high-S/N spectral regions and C III in low-S/N regions, sometimes a C III corresponding to a C IV component in an absorption wing or in a broad profile is not required, i.e. no need of C III for a certain C IV. Moreover, some expected C III components occurs in severely blended regions. In such cases, we did not estimate upper limits of C III components, since upper limits are not very meaningful. Without a corresponding certain C III, these C IV components were not included in the analysis.

(vi) Since the H I absorbers were selected to be optically thin in the Lyman continuum, most C IV components in the sample do not have an associated C II. When C II  $\lambda\lambda 1334.53$  or  $1036.33$  is not detected in absorption-free regions, upper limits for  $N_{\text{C II}}$  are also estimated.

All the blending possibilities and the continuum placement uncertainties were taken into account when C III  $\lambda 977$  was selected and profile-fitted. Unfortunately the C III line is a singlet, so there is no obvious way to recognise weak H I Ly $\alpha$  blending on top of C III. The requirement that C III has the same redshift and Doppler parameter as C IV helps somewhat, but does not guarantee a clean or robust C III identification. As a result, any C III column density in the sample could well be an upper limit only.

With no other selection criterion except the apparent cleanness of C III, our C III selection might be considered biased in favour of narrower C III over broader. We searched for a corresponding C III component candidate to a corresponding, detected C IV component, regardless of the C IV line width. With a “tied” profile fit, a validity of C III component fits depend mostly on blending with H I with confusion introduced by continuum uncertainty and a low S/N.

Blending by H I should be random in each analysed C III region, since the  $z$  and  $N_{\text{H I}}$  distributions of H I Ly $\alpha$  can be considered to be random over a small redshift range (Hu et al. 1995; Kim et al. 2001). In addition, a strong H I blending would not produce a similar C III profile shape as C IV. If H I blending does not change the C III profile shape, it is likely to be weak, i.e.  $N_{\text{C III}}$  would not be affected by a large factor. As our C III sample is mostly unsaturated and narrow, the fitted C III column density should not be far off from the true C III column density.

Continuum uncertainty and a low S/N are mostly against a detection of weak and broad C III components. However, as long as H I blending is weak, a “tied” profile fit and a known C IV velocity structure enable us to obtain all the corresponding C III components, regardless of line widths. We iterated the tied fits several times with a slightly different continuum adjustment each time and found a best-fit for a given C III absorber in order to minimise the selection bias against weak and broad C III. We note that not all analysed C III regions have a low S/N and a highly uncertain continuum placement. The continuum placement uncertainty in the C III region is generally up to 5 to 10%, since we have fitted all the available H I Lyman series and identified metal lines affecting the C III region. When C III is fairly unblended or blending is well-characterised, the continuum uncertainty is less than 5%. Any small continuum adjustments at this level do not change the fitted column

density of C III more than  $\sim 0.1$  dex. We discarded any C III located in a region having a large continuum uncertainty.

Weak H I blending and continuum uncertainty would increase the scatter in any correlation involving with  $N_{\text{C III}}$ , but would not alter any obvious trends between real physical parameters.

### 2.3.3 The final C III sample

As our main interest is the low-density absorbing gas, only C IV systems associated with Lyman continuum optically-thin H I absorbers at  $\log N_{\text{H I}} < 17.2$  were chosen to look for relatively clean C III. From 19 QSOs, a total of 53 C IV systems was selected, consisting of 155 C IV components. Out of 155, 23 C IV components were found to be associated with a blended or a shifted C III. Therefore, any analysis involving C III is restricted to 132 tied (or aligned) C III+C IV component pairs. Of these, 104 have clean C III (not saturated, nor upper limits), in 4 it is saturated and in 24 only upper-limits could be obtained. In this work, we use the term C IV system in a conventional sense, *i.e.* an isolated, possibly complex, C IV absorption feature. Examples are shown in Fig. 1. In general, a continuous C IV absorption profile associated with optically-thin H I absorbers spans less than  $500 \text{ km s}^{-1}$ . Components refer to the individually fitted absorption lines at some specific redshift as determined by VPFIT.

Although C IV and C III have associated H I, these do not always show the same velocity structure. In part this is due to the fact that H I has a larger thermal width than C IV and C III for the same temperature, and it is more difficult to separate these broader lines into distinct components. The number of the tied H I+C IV component pairs from 155 C IV components in 53 C IV systems is 54, *i.e.* about 35% of the analysed C IV sample. Recall that we tied components only if the velocity difference between the corresponding C III and C IV (H I and C IV) components is less than  $1.5 \text{ km s}^{-1}$  ( $15 \text{ km s}^{-1}$ ), as explained Section 2.2.2.

Out of 54 tied H I+C IV pairs, 33 pairs also have a tied C III component, while 17 and 4 pairs have a upper-limit and a blended/uncertain C III component, respectively. Since the latter does not have a clean associated C III detected, they are not in the sample of 132 C IV+C III pairs, but included only in the analysis of the temperature and non-thermal motion in Section 3.

The tied H I+C IV component pairs are further classified into 2 subclasses, certain and uncertain. Even if an isolated C IV component is well-aligned with a cleanly separable H I component, the pair is labelled uncertain if C IV is located in the low-S/N spectral region since the C IV line parameters are then not well-determined, *e.g.* the  $z = 2.572434$  pair toward HE2347–4342. In addition, when a weak C IV component exists nearby with a strong C IV component clearly tied with a single H I component, this pair is also classified as uncertain. For example, the two H I+C IV pairs at  $v = -75$  and  $+52 \text{ km s}^{-1}$  in the fourth panel of Fig. 1 are both classified as uncertain. There are 40 certain and 14 uncertain tied H I+C IV pairs.

Figure 3 displays the redshift distributions of 53 C III systems and 132 C IV+C III components in our sample. About 40% of the C III absorbers is at  $2.3 < z < 2.5$ . An apparent deficiency of C III systems at  $z \sim 2.6$  is an observational bias, caused by a lower number of QSOs covered at

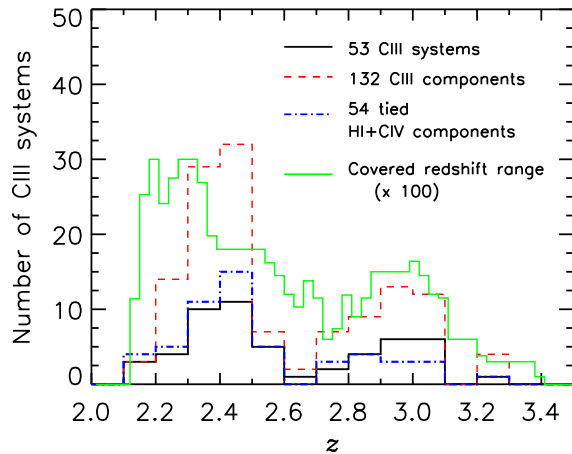


**Figure 3.** Redshift distributions of 53 C III systems, 132 C III components including 24 upper limits and 108 detected C III components, and 54 tied H I+C IV pairs. The green histogram shows the covered redshift range by 19 QSOs multiplied by 100 times for clarity. Without incompleteness correction for C III recovery rate mainly due to blending and low-S/N, the number of C III absorbers is *not* a physically-meaningful detection rate.

that redshift range. We note that there is no incompleteness correction for C III which might have been missed because of heavy blending, low-S/N or unreliable continuum placement. Therefore, the redshift distribution of analysed C III in Fig. 3 should *not* be used as a physically meaningful number density evolution of C III absorbers with redshift.

Table 2 lists the line parameters of H I, C IV, C III and C II components in our 53 C III systems, including uncertainty and upper-limit components. The entire Table 2 and the velocity plot of entire 53 C III systems similar to Fig. 1 are published electronically. The velocity plots also include uncertain C III components marked with a thin light green tick. These have either a significantly shifted velocity centroid or are located in the profile wing for which the fitted line parameter is very uncertain. These are not included in the further analysis. Unless stated otherwise, all the analyses in this study are based on individual components.

## 3 COLUMN DENSITY AND DOPPLER PARAMETER DISTRIBUTIONS

Using the fitted ion column densities and Doppler parameters of H I, C IV and C III given in Table 2, we examine their distributions and look for any correlations between them.

### 3.1 The H I+C IV+C III sample

First, in order to see whether or not our C III sample represent a typical set of IGM absorbers, we consider the Doppler parameter vs column density distributions for C IV and H I for our selected samples and compare these with the distributions for the populations as a whole. Figure 4 shows the  $\log N_{\text{C IV}} - \log b_{\text{C IV}}$  distribution of C IV for those with associated C III, set against 431 C IV components with  $\log N_{\text{C IV}} \in [11.5, 15.0]$  at  $2.1 < z < 3.4$  from the 19 QSOs

**Table 2.** The line parameters of C III absorbers <sup>a</sup>

# <sup>b</sup>	Ion	$\Delta v^c$ (km s <sup>-1</sup> )	$z_{\text{abs}}^c$	$b^d$ (km s <sup>-1</sup> )	$\log N$
Q0055-269, $z = 3.256208$ , $[-40, +120]$ km s <sup>-1</sup> , <sup>e</sup>					
x	C IV	$-17 \pm 9$	3.255963	$12.6 \pm 2.0$	$12.92 \pm 0.09$
1	C IV	$0 \pm 3$	3.256208	$9.0 \pm 0.8$	$13.02 \pm 0.07$
	C III			9.0	$13.13 \pm 0.11$
x	H I	$6 \pm 17$	3.256300	$34.1 \pm 3.0$	$15.18 \pm 0.08$
2	C IV	$30 \pm 7$	3.256628	$10.8 \pm 2.2$	$12.63 \pm 0.09$
	C III			10.8	$12.45 \pm 0.16$
x	H I	$49 \pm 16$	3.256899	$14.4 \pm 3.5$	$14.49 \pm 0.24$
3	C IV	$51 \pm 3$	3.256940	$11.4 \pm 1.2$	$12.95 \pm 0.04$
	C III			11.4	$13.01 \pm 0.04$
4	C IV	$81 \pm 2$	3.257359	$10.8 \pm 0.8$	$12.76 \pm 0.03$
	H I			$24.7 \pm 0.9$	$13.93 \pm 0.02$
	C III			10.8	$12.54 \pm 0.06$
	C II			25.6	$\leq 12.55$

<sup>a</sup> Only the beginning of the entire table is shown. The full version of this table is available electronically on the MNRAS web page.

<sup>b</sup> The tied component is grouped with a group number. A component marked with “x” indicates a component with no other corresponding ions or a uncertain C III component with a certain C IV.

<sup>c</sup> The relative velocity is centred at the C IV flux minimum. Only the  $z$ -reference-ion C IV has an error.

<sup>d</sup> For a tied fit, only the reference ion C IV is provided with a fit error for the tied parameters  $z$  and  $b$ .

<sup>e</sup> The relative velocity ranged over which useful C III components are found.

listed in Table 1 including C IV associated with optically-thick absorbers. As can be seen from the figure, those components for which only upper limits could be measured for C III tend to correspond to lower C IV column densities, while the few saturated C III lines correspond to higher C IV column densities. Given that the current sample consists of 132 C III+C IV components pairs, only about 31% (132 out of 431) of all the C IV components are suitable for any further analysis. Note that this is not an actual C IV+C III association rate, however, it may be taken as a lower limit. Unlike C IV, blending of C III  $\lambda 977$  with Ly $\alpha$  forest lines reduces the effective S/N. Therefore, C III is not always be detected at the nominal limit for the S/N where it occurs.

As with C IV, we may examine the  $N_{\text{H I}}-b_{\text{H I}}$  diagram for the H I components. This is shown in the left panel of Fig. 5, with gray data points indicating 3956 H I components in the 19 QSOs with  $\log N_{\text{H I}} \in [12.2, 17.0]$  at  $2.1 < z < 3.4$ . The H I components highlighted here are those 54 components which have well-aligned associated C IV with or without detected C III. For these, we estimate the temperature  $T$  and turbulent Doppler parameter  $b_{\text{nt}}$  by constraining the redshifts to be the same and tying the Doppler parameters using Eq. 1. In order to distinguish it from the gas temperature derived from a photoionisation model, we note the temperature calculated from the line widths by VPFIT as  $T_b$  in this study.

Four green crosses represent a H I+C IV pair dominated by non-thermal broadening, as discussed in Section 3.3. They do not seem to occur in any preferred area, although

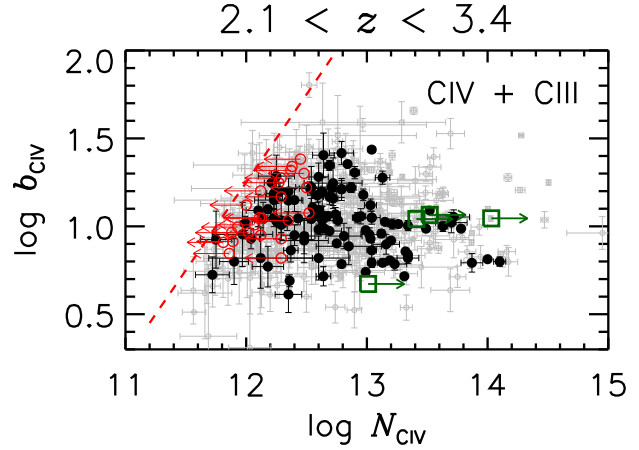


**Figure 4.** The  $\log N_{\text{C IV}}-\log b_{\text{C IV}}$  distribution. Filled circles, red open circles and green open squares indicate C IV associated with 104 clean, 24 upper-limit and 4 lower-limit C III regardless of association with a well-aligned H I. Grey open circles show the distribution of 431 C IV components from the 19 QSO spectra in the redshift range listed in Table 1. The dashed line indicates the C IV detection limit. Refer to the online version for clarity.

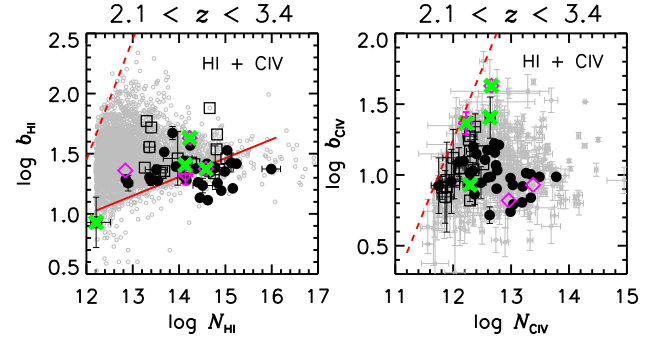


**Figure 5.** *Left panel:* The Doppler parameter vs column density distribution of H I for the same redshift range as in Fig. 4. Grey open circles indicate the distribution for 3956 H I components with  $\log N_{\text{H I}} \in [12.2, 17.0]$  from the 19 QSOs, shown without errors for clarity. These are from the high-order Lyman fit using all the available high-order lines to obtain more robust line parameters of saturated lines used in the current study, including the tied parameter fits. Filled circles indicate 33 H I components with well-aligned C IV and C III with errors where these are larger than the symbol size. Open squares denote the 17 well-aligned H I+C IV components with C III upper limits, and magenta open diamonds are the 4 such components with blended C III. The dashed line indicates the H I detection limit, while the red solid line shows the cut-off  $b$  as a function of  $N_{\text{H I}}$  at  $\langle z \rangle = 2.4$  taken from Rudie et al. (2012). Green crosses represent the non-thermally broadened components, which have the gas temperature less than 5000 K. Some of the grey data points below the cutoff- $b$  line will be unidentified metal lines. *Right panel:*  $N_{\text{C IV}}$  vs  $b_{\text{C IV}}$  of 54 tied H I+C IV pairs overlaid with 431 C IV components at  $\log N_{\text{C IV}} \in [11.5, 15.0]$  as shown in Fig. 4. The symbols have the same meaning as in the left panel. Refer to the online version for clarity.

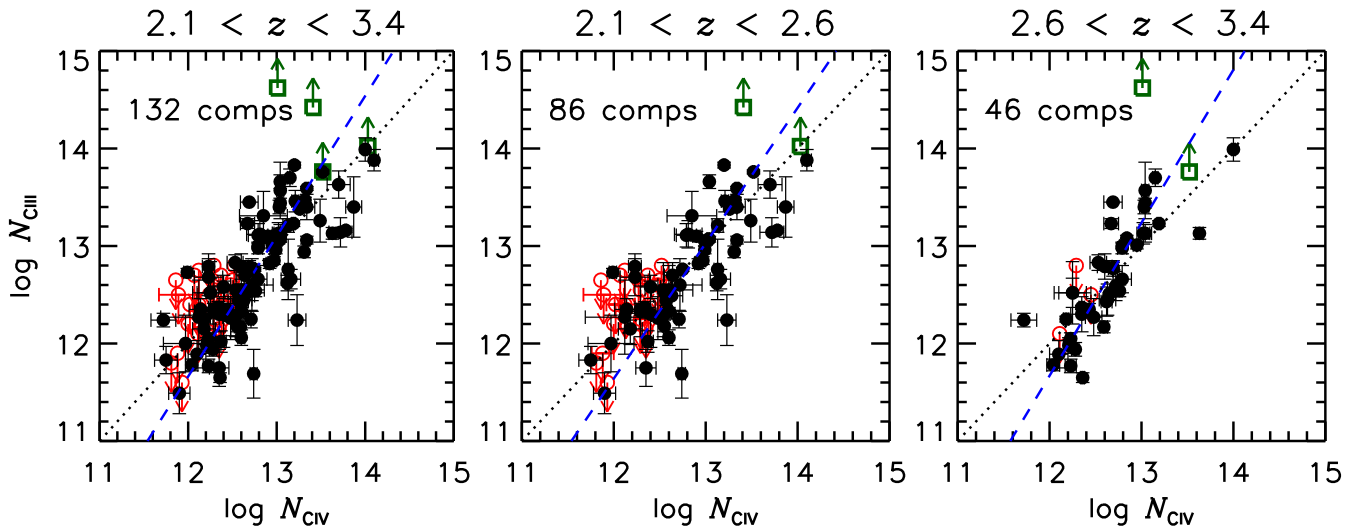


**Figure 6.** The  $N_{\text{CIV}}-N_{\text{CIII}}$  relation at three redshift ranges. Filled circles, red open circles and green squares indicate 104 clean, 24 upper-limit and 4 lower-limit C III components, respectively. Only errors larger than the symbol size are displayed. Dotted lines indicate a one-to-one relation. Dashed lines represent a robust least squares fit:  $\log N_{\text{CIII}} = A + B \times \log N_{\text{CIV}}$ , while  $A = (-5.61 \pm 1.44, -5.03 \pm 2.06, -7.16 \pm 2.44)$  and  $B = (1.44 \pm 0.11, 1.39 \pm 0.16, 1.57 \pm 0.19)$  at  $2.1 \leq z \leq 3.4$ ,  $2.1 \leq z \leq 2.6$  and  $2.6 \leq z \leq 3.4$ , respectively.

it could be caused by a small-number statistics. All of them have a low temperature at  $T_b \leq 5000$  K.

Only  $\sim 1\%$  (54 out of 3956) of all the H I components can be used for estimating the gas temperature and non-thermal motion in this study. This low fraction is mainly because a majority of low- $N_{\text{HI}}$ , intervening H I have no associated C IV above the detection limit. In addition, the fraction is further reduced by the requirement that C III be measurable, since the tied H I+C IV sample is taken from the C IV+C III sample.

The lower cutoff- $b$  as a function of  $N_{\text{HI}}$ ,  $\log b_{\text{HI}} = 1.244 + 0.156 \times (\log N_{\text{HI}} - 13.6)$  at  $\langle z \rangle = 2.4$  (Rudie et al. 2012), is shown in the left panel of Fig. 5. This cutoff- $b_{\text{HI}}$  line is important as it is often used to estimate the IGM gas temperature (Schaye et al. 2000; Ricotti et al. 2000; Rudie et al. 2012; Bolton et al. 2014). The Rudie et al. (2012) minimum  $N_{\text{HI}}-b_{\text{HI}}$  relation also appears to fit well for the general Ly $\alpha$  forest in this study. Almost all of our tied H I+C IV pairs in the  $N_{\text{HI}}-b_{\text{HI}}$  plane lie close to the cutoff- $b$  line, except a few pairs above the red solid line. Except 4 H I+C IV pairs dominated by a non-thermal broadening (green crosses), the tied H I+C IV pairs without C III (open squares) have a temperature at  $\log T_b = 4.3-5.5$ . For the H I+C IV pairs with C III, the temperature spans a lower  $T_b$  range at  $\log T_b = 3.9-5.5$ , with 73% having  $\log T_b \leq 4.5$ . This implies that some of H I+C IV pairs with C III upper limits is due to a higher temperature. Indeed, many outliers above the red solid line are  $N_{\text{CIII}}$ -upper-limit pairs.

Unlike the C IV+C III pairs, the H I+C IV pairs do not sample a wide range of column density and  $b$  value of H I. Although there is no well-defined one-to-one relation between  $T$  and  $b$  or between the volume density and  $N_{\text{HI}}$ , a lack of tied pairs with a larger  $b$  or a smaller  $N_{\text{HI}}$  implies that our tied pairs do not include a higher-temperature gas and a lower density gas, but sample a gas within a limited physical condition. This is in part caused by the observational bias, since a larger thermal width of H I compared to C IV

does not allow to recognise closely adjacent H I components as precisely as C IV in a multi-component C IV absorber.

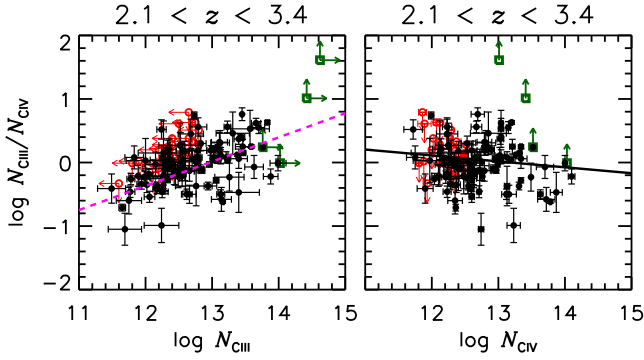
Unlike H I in the left panel, C IV in the tied H I+C IV pairs in the right panel of Fig. 5 displays a wider range of column density and  $b$ . Combined with the  $N_{\text{HI}}-b_{\text{HI}}$  distribution, C IV components of the tied pairs is not expected to show very well-correlated relations with H I components, i.e.  $N_{\text{CIV}}$  is not a well-behaved function of  $N_{\text{HI}}$ .

### 3.2 Correlations between $N_{\text{HI}}$ , $N_{\text{CIV}}$ and $N_{\text{CIII}}$

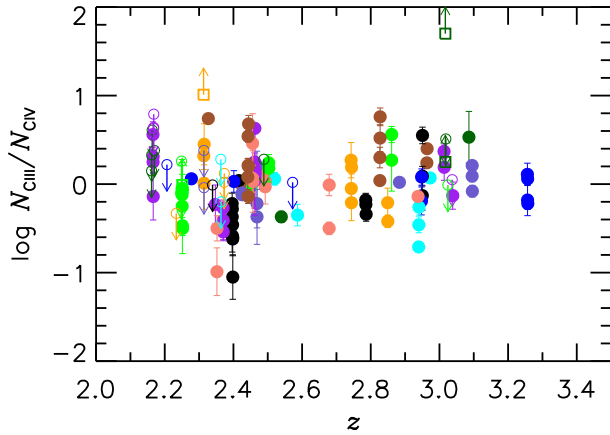
A straightforward quantity to consider is the  $N_{\text{CIV}}-N_{\text{CIII}}$  relation. For the collisional ionisation equilibrium (CIE), the ratio of two ions depends on the gas temperature. For the photoionisation equilibrium (PIE), the ratio depends largely on the ionisation parameter, the ionising photon flux divided by the gas density.

Figure 6 illustrates the  $N_{\text{CIV}}-N_{\text{CIII}}$  relation for three different redshift ranges,  $2.1 \leq z \leq 3.4$ ,  $2.1 \leq z \leq 2.6$ , and  $2.6 \leq z \leq 3.4$ , along with least-squares fits for clean C III detections only, i.e. excluding upper limits and lower limits. The division redshift is simply chosen from Fig. 3, which shows an apparent dip in the number distribution of C III systems at  $z \sim 2.6$  due to the observational bias. There are no indications of any redshift evolution of the  $N_{\text{CIV}}-N_{\text{CIII}}$  relation. For a given  $N_{\text{CIV}}$ , the spread in  $N_{\text{CIII}}$  is  $\sigma \sim 0.3$  dex, when fitted to a Gaussian.

For the full redshift range,  $N_{\text{CIII}} \propto N_{\text{CIV}}^{1.42 \pm 0.11}$  at  $\log N_{\text{CIV}} \in [11.7, 14.1]$ . However, at  $\log N_{\text{CIV}} \sim 14$ ,  $N_{\text{CIII}}$  is lower than expected from the dashed line, suggesting that the log-linear relation between  $N_{\text{CIII}}$  and  $N_{\text{CIV}}$  might well break down at higher  $N_{\text{CIV}}$ . However, given only a few C IV components at  $\log N_{\text{CIV}} \geq 13.6$ , any firm conclusions cannot be drawn. At the same time, due to a lack of enough data at high- $N_{\text{CIV}}$  ends, a one-to-one relation could be a good approximation between  $N_{\text{CIV}}$  and  $N_{\text{CIII}}$ . A lack of high- $N_{\text{CIV}}$



**Figure 7.**  $N_{\text{CIII}}/N_{\text{CIV}}$  as a function of  $N_{\text{CIII}}$  (left panel) and of  $N_{\text{CIV}}$  (right panel) at  $2.1 < z < 3.4$ . All the symbols are the same as in Fig. 6. The magenta dashed line in the left panel represents a least-square fit of clean C III detections excluding lower and upper limits:  $\log N_{\text{CIII}}/N_{\text{CIV}} = (-4.94 \pm 0.16) + (0.38 \pm 0.01) \times \log N_{\text{CIII}}$ . In the right panel, the solid line is a least-square fit:  $\log N_{\text{CIII}}/N_{\text{CIV}} = (1.23 \pm 0.18) + (-0.09 \pm 0.01) \times \log N_{\text{CIV}}$ .



**Figure 8.**  $N_{\text{CIII}}/N_{\text{CIV}}$  as a function of  $z$  at  $2.1 < z < 3.4$ . Filled symbols are the C IV+C III pairs with cleanly detected C III. Open symbols with upward and downward arrows indicate the C IV+C III pairs with lower-limit C III and upper-limit C III, respectively. The pairs belonging to the same system are coded with the same colour. Refer to the online version for clarity.

components is in part due to the fact that the number density of higher- $N_{\text{CIV}}$  components is smaller (Kim et al. 2013).

Even though  $N_{\text{CIII}}$  increases faster than  $N_{\text{CIV}}$ ,  $N_{\text{CIII}}$  is lower than  $N_{\text{CIV}}$  at  $\log N_{\text{CIV}} \leq 13$  and is higher at  $\log N_{\text{CIV}} \geq 13$ . Therefore, the mean  $N_{\text{CIII}}/N_{\text{CIV}}$  is  $< N_{\text{CIII}}/N_{\text{CIV}} > = 1.0 \pm 0.3$  at  $2.1 < z < 3.4$  for the C IV components aligned with the clean C III components. If the C III+C IV gas is in CIE,  $< N_{\text{CIII}}/N_{\text{CIV}} > \sim 1$  suggests the gas temperature of  $\sim 10^5$  K (Gnat & Sternberg 2007). For the PIE gas,  $< N_{\text{CIII}}/N_{\text{CIV}} >$  indicates  $T \sim 10^{4.2-5}$  K (Oppenheimer & Schaye 2013).

Figure 7 displays  $N_{\text{CIII}}/N_{\text{CIV}}$  as a function of  $N_{\text{CIII}}$  (left panel) and of  $N_{\text{CIV}}$  (right panel), respectively. In the left panel,  $N_{\text{CIII}}/N_{\text{CIV}}$  increases with  $N_{\text{CIII}}$  as expected, since  $N_{\text{CIII}}$  increases faster than  $N_{\text{CIV}}$ . On the other hand,  $N_{\text{CIII}}/N_{\text{CIV}}$  seems to suggest a weak decrease with  $N_{\text{CIV}}$  in the right panel (solid line). This is mainly caused by the data points having a lower  $N_{\text{CIII}}$  than the log-linear

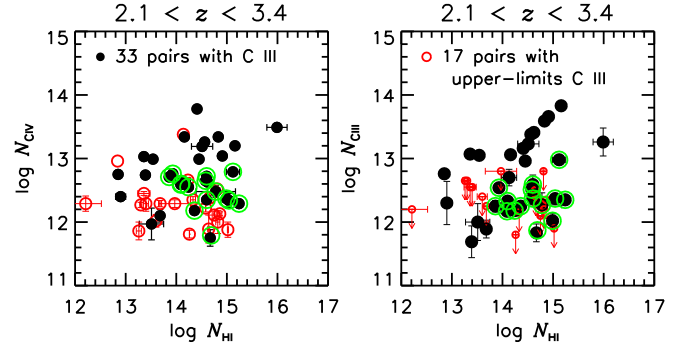


**Figure 9.**  $N_{\text{HI}}-N_{\text{CIV}}$  (left panel) and  $N_{\text{HI}}-N_{\text{CIII}}$  (right panel) of the tied H I+C IV+C III components at  $2.1 < z < 3.4$ . Filled circles and open red circles are the 33 and 17 H I+C IV pairs with clean C III and upper-limit C III, respectively. No lower-limit C III is associated with a well-aligned H I. Data points embedded with a larger green open circle are low-metallicity branch absorbers discussed in Section 5. Refer to the online version for clarity.

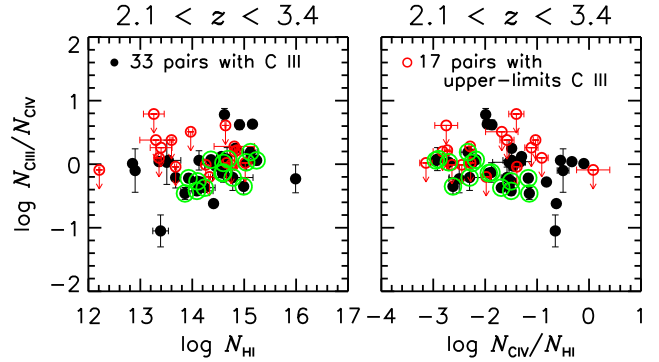


**Figure 10.**  $N_{\text{CIII}}/N_{\text{CIV}}$  as a function of  $N_{\text{HI}}$  (left panel) and as a function of  $N_{\text{CIV}}/N_{\text{HI}}$  (right panel) at  $2.1 < z < 3.4$ . All the symbols have the same meaning as in Fig. 9. Refer to the online version for clarity.

relation at  $\log N_{\text{CIV}} \sim 14$  as seen in Fig. 6. The same data points are scattered at  $\log N_{\text{CIV}} \in [13.0, 14.2]$  and  $\log N_{\text{CIII}}/N_{\text{CIV}} \in [-1.0, 0.0]$  in the right panel. This leads to a weak decrease of  $N_{\text{CIII}}/N_{\text{CIV}}$  with  $N_{\text{CIV}}$ .

The redshift evolution of  $N_{\text{CIII}}/N_{\text{CIV}}$  is presented in Fig. 8. Filled and open symbols indicate the C IV+C III pairs with clean C III and C III limits, respectively. There is a large spread of  $\sim 1$  dex in  $N_{\text{CIII}}/N_{\text{CIV}}$  even within the same system, as commonly seen in the high- $N_{\text{HI}}$  absorbers, cf. Boksenberg & Sargent (2015). This suggests that the C IV-bearing gas components within a system have a range of internal conditions.

There are only a small number of tied H I+C IV+C III components, so the  $N_{\text{HI}}-N_{\text{CIV}}$  and the  $N_{\text{HI}}-N_{\text{CIII}}$  relations are poorly constrained and are effectively scatter plots (Fig. 9). However, when tied C III trios shown as filled circles are grouped into 2 classes as high-metallicity branch absorbers and low-metallicity branch absorbers introduced in Section 1 and discussed in Section 5, there seems a trend. For high-metallicity branch absorbers (clean, filled circles),  $N_{\text{HI}}$  roughly increases with  $N_{\text{CIV}}$  and  $N_{\text{CIII}}$ . On the other hand, low-metallicity branch absorbers embedded with a larger green open circle show no correlation.

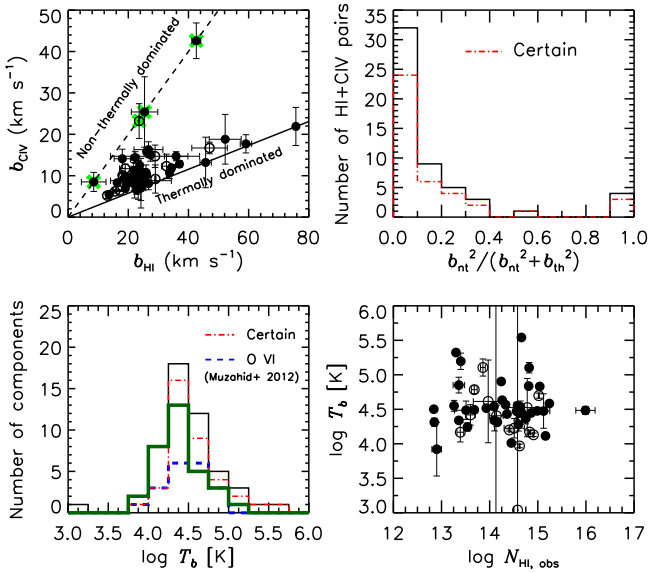


**Figure 11.** Gas temperature and non-thermal  $b$ ,  $b_{\text{nt}}$ , of the 54 tied H I+C IV pairs. Filled and open circles indicate the 40 certain pairs and the 14 uncertain pairs as described in Section 2.3.3. *Upper left:*  $b_{\text{HI}}$  vs  $b_{\text{CIV}}$ . Green crosses are the pairs as in Fig. 5 and have  $T_b \leq 5000$  K. *Upper right:* the ratio between the non-thermal energy and the total (thermal plus non-thermal) energy,  $b_{\text{nt}}^2 / (b_{\text{nt}}^2 + b_{\text{th}}^2)$ , for the full (solid histogram) and certain (red dot-dashed histogram) samples. *Lower left:* the gas temperatures for the full (solid histogram) and certain (red dot-dashed histogram) samples. The thick green histogram is for the 33 pairs with a detected C III excluding lower limits. The overlaid blue dashed histogram is taken from Muzahid et al. (2012) for O VI at  $z \sim 2.3$ . Only the H I+O VI pairs whose velocity difference is less than  $10 \text{ km s}^{-1}$  are included. *Lower right:* the gas temperature as a function of  $\log N_{\text{HI}}$ . The four non-thermally broadened absorbers are not included.

In Fig. 10, the detected data points on the  $N_{\text{HI}} - N_{\text{CIII}}/N_{\text{CIV}}$  plane (left panel) and on the  $N_{\text{CIV}}/N_{\text{HI}} - N_{\text{CIII}}/N_{\text{CIV}}$  plane (right panel) suggest no correlation. Since the upper limits on both planes have the values similar to the detected ones, the lack of correlation between these quantities is reasonable. This means that both  $N_{\text{CIV}}$  and  $N_{\text{CIII}}$  increase with  $N_{\text{HI}}$  in a roughly similar way, even with the larger scatter at higher  $N_{\text{CIII}}$  and  $N_{\text{CIV}}$  seen in Fig. 7.

### 3.3 The gas temperature and the non-thermal motion

A comparison of the Doppler parameters of C IV and H I for the 54 tied H I+C IV pairs is shown in Fig. 11 (upper left panel). Table A1 lists the line parameters of individual tied components, their derived gas temperature  $T_b$  and non-thermal  $b_{\text{nt}}$  parameter.

A majority of the pairs are close to being thermally dominated, while the 4 pairs are turbulently broadened. These 4 tied pairs are at  $z = 2.937304$  toward HE0940–1050,  $z = 2.787112$  toward HE2347–4342,  $z = 2.456208$  toward PKS0329–255 and  $z = 2.248307$  toward Q0329–385 with the gas temperature of  $\leq 92$  K,  $\leq 12830$  K,  $\leq 538$  K and  $\leq 385$  K, respectively. These pairs have the same  $b$  value for H I and C IV, therefore, the gas temperature cannot be

constrained at all. With  $b = 42.6, 23.6, 25.4$  and  $8.5 \text{ km s}^{-1}$ , respectively, the non-thermally broadened absorbers seem to prefer a larger  $b$ , but with only 4 absorbers, no firm conclusion cannot be drawn.

The non-thermal and thermal contributions to the H I+C IV pairs are more clearly seen in the upper-right panel, which shows the histogram of the ratio of the non-thermal energy to the total energy,  $b_{\text{nt}}^2 / (b_{\text{th}}^2 + b_{\text{nt}}^2)$ . For about 59% of the H I+C IV pairs (32 out of 54), the non-thermal energy is less than 10%. The median  $b_{\text{nt}}$  and  $b_{\text{th}}$  are  $7 \text{ km s}^{-1}$  and  $22 \text{ km s}^{-1}$ , respectively. When  $b_{\text{CIV}} \geq 20 \text{ km s}^{-1}$ , there is a possibility that a seemingly single-component C IV breaks into many weaker components in a higher-S/N spectrum, in which case a contribution by non-thermal broadening could be smaller.

The lower-left panel shows the distribution of the gas temperature for both the full and “certain” samples. While a broader H I or C IV component could reveal a multi-component nature in much higher-S/N spectra,  $\log T_b \geq 5$  is also expected since intergalactic C IV is produced by radiatively cooling gas once shock-heated to  $\log T_b \geq 7$  and now exposed to the UVB (Cen & Chisari 2011; Shen et al. 2013).

For the 54 tied pairs, the mean temperature of the full and certain samples is  $\langle \log T_b \rangle = 4.27 \pm 1.00$  and  $\langle \log T_b \rangle = 4.25 \pm 1.14$ , respectively. The median temperature is  $\log T_{b,\text{med}} = 4.47$  and  $\log T_{b,\text{med}} = 4.48$  for the full and certain samples, respectively. When excluded 4 non-thermally broadened pairs, for the full sample,  $\langle \log T_b \rangle = 4.52 \pm 0.33$  and  $\log T_{b,\text{med}} = 4.48$ . Considering a large error, our mean temperature of the 54 pairs is consistent with the one,  $\langle \log T_b \rangle = 4.58$ , found by Rauch et al. (1996) from the 26 C IV+Si IV pairs at the similar redshifts. When excluded non-thermal pairs, our mean temperature of the 50 pairs is in better agreement with the Rauch’s mean temperature, although C IV+Si IV pairs typically sample a higher- $N_{\text{HI}}$  absorber than typical H I+C IV pairs without associated Si IV.

Since our H I+C IV pairs do not have any unusual selection criterion apart from being kinematically simple, we may assume that this small number of pairs is a representative of typical optically-thin C IV-bearing gas found in the spectra of high- $z$  QSOs. The  $T_b$  distribution is well-approximated by a Gaussian peaking at  $\log T_b \sim 4.43$  with  $1\sigma = 0.27$  and  $\log T_b \sim 3.5$ – $5.5$ . Considering that C IV peaks at  $\log T \sim 5$  in CIE, the observed temperature distribution implies that the H I+C IV gas samples both photoionised and collisionally ionised C IV. This C IV temperature distribution is very similar to the simulated result for  $\log N_{\text{CIV}} \in [12, 14]$  at  $z = 2.6$  by Cen & Chisari (2011). The H I+C IV+C III trios excluding lower-limit  $N_{\text{CIII}}$  components account for only 61% (33 out of 54) of the total sample, but show a similar  $T_b$  distribution.

For comparison, the lower-left panel also shows the temperature estimates from the observed  $b$  parameters of aligned H I+O VI at  $z \sim 2.3$  taken from Muzahid et al. (2012). Muzahid et al.’s O VI temperature distribution is very similar to our C VI temperature distribution. This is not what is expected from simulations, which predicts that O VI is produced by higher temperature gas than C IV (Cen & Chisari 2011). However, the detection of high temperature, and hence broad, O VI lines in the Ly $\alpha$  forest is difficult, since

they are more likely to be misidentified as H I. This bias may be responsible for part of the discrepancy.

The lower-right panel of Fig. 11 displays  $\log T_b$  as a function of  $N_{\text{H I}}$ . It shows that the gas temperature does not correlate with  $N_{\text{H I}}$ , which is expected from the optically thin PIE gas. We have found that there is no noteworthy correlations between  $b_{\text{nt}}$ ,  $T_b$ ,  $z$ ,  $N_{\text{C IV}}$  or  $N_{\text{C III}}$ .

In summary, our data suggest that most of the tied low- $N_{\text{H I}}$  absorbers located around the cutoff- $b$  line are thermally broadened, with a small contribution from turbulent motion. The result also confirms that the cutoff- $b$  line is a valid tool to probe the IGM temperature. H I+C IV pairs display a wide range of the temperature at  $\log T_b \in [3.5, 5.5]$ , with a few non-thermally broadened pairs with  $\log T_b \leq 3.7$ . The temperature distribution peaks at  $\log T_b \sim 4.4$ , implying that a majority of C IV is photoionisation dominated.

## 4 PHOTOIONISATION MODELLING

### 4.1 Basic assumptions

The narrow line width of the low-density Ly $\alpha$  forest implies that photoionisation is the dominant ionisation mechanism rather than collisional ionisation (Bergeron & Stasińska 1986; Haehnelt et al. 1996). Theories reproducing the general observed properties of the H I forest also predict that the forest is photoionised by the external UV background (UVB) contributed both from QSOs and galaxies, assuming it in photoionisation equilibrium (Bergeron & Stasińska 1986; Cen et al. 1994; Haehnelt et al. 1996; Theuns et al. 1998; Schaye et al. 2000; Schaye 2001; Davé et al. 2010).

There are several critical pre-requirements for the photoionisation modelling to be valid. First, all the absorption lines of interest should be produced in the same gas. Thus, for a constant gas temperature through the region, ionic absorption components can be used only when their velocity structure is the same. Second, the absorption lines should be properly resolved and deblended so that reliable column densities and line widths can be determined. Third, there should exist a H I component clearly associated with other ionic transitions of interest. The ratio of ionic column densities is insensitive to the metallicity and  $N_{\text{H I}}$  for the ionization parameter  $-3.0 \leq \log U \leq 0$ , a  $U$  range for typical Ly $\alpha$  absorbers. However, as one of our scientific interests is to estimate the carbon abundance,  $N_{\text{H I}}$  is necessary to break the degeneracy. Fourth, more than two ionic transitions of the same metal species should be present. In general, the metallicity and the gas density (or the ionisation parameter  $U$ ) are unknown. When only one ionic transition is available, a different combination of the metallicity and density predicts the same column density. Additional ionic transitions break this degeneracy.

These requirements imply that photoionisation modelling should be applied only on clean, individual *components*, as opposed to total column densities obtained by adding up all the components of an absorption system. If a physical condition of gas producing each component of a multi-component system is similar, the total column densities of the system can be used, i.e. the derived physical parameters of the system approximate the average of the individual components. However, there is no solid physical

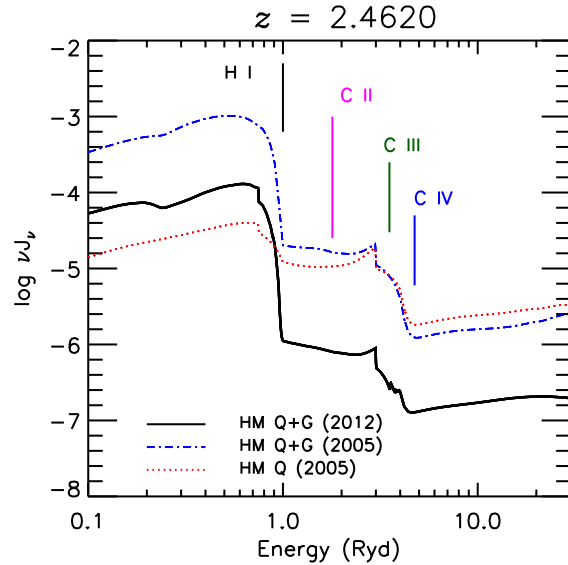


**Figure 12.** Examples of three UV background radiation fluxes  $J_\nu$  as a function of the frequency  $\nu$  in Rydbergs at  $z = 2.4620$  used for Cloudy modelling. Our fiducial HM Q+G 2012 is shown as the solid curve, while the Cloudy-default HM Q+G 2005 and the HM Q 2005 are the blue dot-dashed and the red dotted curves, respectively (see Section 4.2). The ionisation potential of each ion of interest is marked with a long vertical line: 1 Ryd (13.6 eV) for H I, 4.74 Ryd for C IV, 3.52 Ryd for C III and 1.79 Ryd for C II.

reason to assume that each component is produced by gas under a similar gas density, temperature and carbon abundance. In fact, the large spread in  $N_{\text{C III}}/N_{\text{C IV}}$  within a given system as shown in Fig. 8 hints that a physical condition might be different among components in the same system.

Of the 155 C IV components in our sample, only the 54 components (35%) have well-aligned H I, and of these only the 33 components have H I, C IV and detected C III (no lower limits) components at the same relative velocity. Of the 33 trios, the  $z = 2.456208$  trios toward PKS0329–255 is non-thermally broadened with  $T_b \leq 538$  K. With a detected high-ion C IV and such a low gas temperature, this absorber is likely to be out of photoionisation equilibrium with the external UV background. Therefore, this trio is excluded in the further photoionisation analysis. Four trios of the 32 also show clean, un-saturated C II. This provides more stringent constraints and a check on the validity of the photoionisation modelling:  $z = 2.462358$  (Q0002–422),  $z = 2.462044$  (Q0002–422),  $z = 2.444109$  (Q0453–423) and  $z = 2.442644$  (Q0453–423). About one third of C II-free components is associated with Si IV (sometimes Si III and Si II as well), while the rest is Si IV-free, as listed in the last columns of Table A2 and A3.

### 4.2 Cloudy modelling

We used the photoionisation code Cloudy version c13.03 (Ferland et al. 2013). The gas was assumed to be a uniform slab in thermal and ionisation equilibrium with a constant density exposed to the external UVB. The Cloudy-default solar abundance pattern is assumed, with a solar carbon

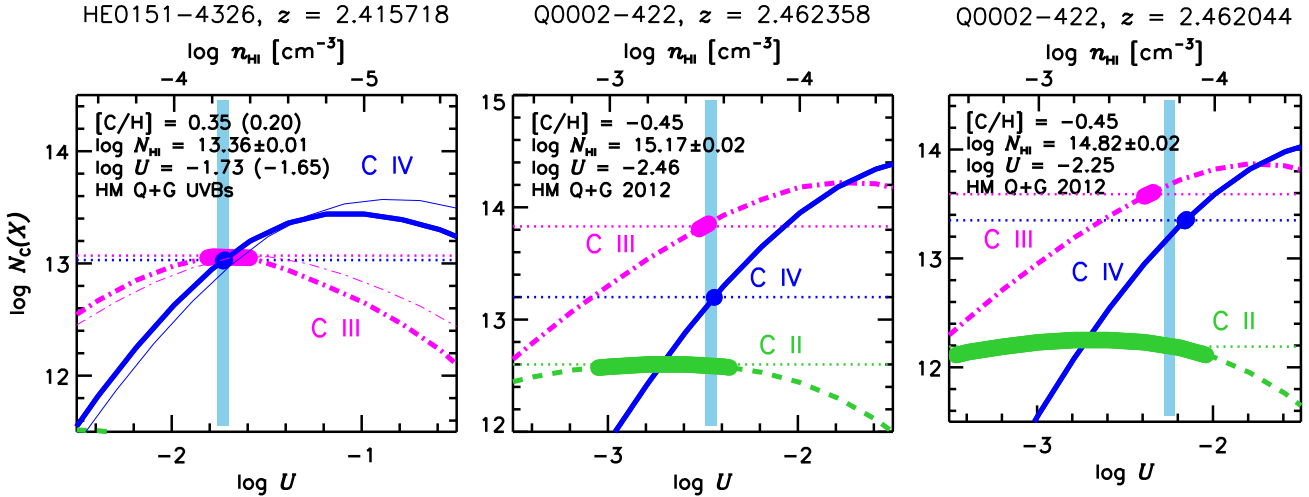


**Figure 13.** Three examples of Cloudy-predicted column densities  $\log N_c(X)$  as a function of ionisation parameter  $U$ , where  $N_c(X)$  is the predicted column density of C IV, C III and C II for different UVB background radiations. Cloudy-predicted  $N_c(\text{C IV})$ ,  $N_c(\text{C III})$  and  $N_c(\text{C II})$  are shown as solid blue, dot-dashed magenta and dashed green curves, respectively. The allowed column density range from the observations is indicated by thicker curves and the horizontal dotted lines with the same colour as the curves. The sky-blue-shaded region is the best-fit  $U$  value for observed column densities. *Left panel:* the  $z = 2.415718$  absorber toward HE0151-4326. Cloudy-predicted column densities for the HM Q+G 2012 (HM Q+G 2005) are shown as thick (thin) curves. *Middle panel:* the  $z = 2.462358$  absorber toward Q0002-422 for the HM Q+G 2012. The best-fit  $\log U = -2.46$  matches the observed  $N_{\text{C IV}}$ ,  $N_{\text{C III}}$  and  $N_{\text{C II}}$  within the allowed error ranges simultaneously. *Right panel:* the  $z = 2.462044$  absorber toward Q0002-422, the worst case in our sample. No  $U$  is found to match the observed carbon ions simultaneously.

abundance of  $(\text{C}/\text{H})_{\odot} = -3.61$ . The carbon abundance is expressed as  $[\text{C}/\text{H}] = \log(\text{C}/\text{H}) - \log(\text{C}/\text{H})_{\odot}$ .

The fiducial UVB was chosen to be the latest Haardt-Madau (HM) UVB 2012 version contributed both by QSOs and galaxies (Q+G) (Haardt & Madau 2012). The main observational inputs for theoretical UVB models, such as the relative contributions of QSOs and galaxies and the UV photon escape fraction as a function of redshift, are still poorly known, and this leads to large uncertainties in the models (Bolton et al. 2005; Shapley et al. 2006; Faucher-Giguère et al. 2008; Siana et al. 2010; Haardt & Madau 2012; Barger et al. 2013). Therefore, we also used the Cloudy-default HM UVB 2005 version for QSOs-only (Q) and for Q+G for comparison.

Based on the inversion method to reconstruct the spectral shape of the UVB from metal absorbers at  $1.8 < z < 2.9$ , Agafonova et al. (2007) claimed that the intergalactic He II Ly $\alpha$  absorption modulates and fluctuates the UVB spectral shape from a QSO-dominated UVB without a need of additional sources such as starburst galaxies. However, their reconstruction was mostly based on border-line Lyman limit systems at  $\log N_{\text{H I}} \geq 16.7$ , where a radiative transfer effect by the internal He II Ly $\alpha$  absorption is important with their estimate on  $N_{\text{He II}}/N_{\text{H I}}$  of 50–150. By comparison, all of our sample but one have  $\log N_{\text{H I}} \leq 15.2$ . In addition, at  $2.2 < z < 2.8$  where most of our sample belong to,  $N_{\text{He II}}/N_{\text{H I}}$  has been found to be 50–80 (Reimers et al. 1997; Shull et al. 2010; Syphers & Shull 2013). Therefore, the internal He II Ly $\alpha$  absorption would not change the spectral shape of the UVB significantly in our case. Although the intensity and spectral shape of the UVB are likely to fluctuate, we assume that a uniform UVB is a good approximation to our optically-thin C III absorbers. Moreover, Bolton & Viel

(2011) found that any realistic UVB fluctuations would not have a significant effect on the intergalactic C IV and Si IV from a variety of toy UVB models.

Figure 12 shows the fiducial UVB and the two other UVBs at  $z = 2.4620$ . The intensity of the HM Q+G 2012 is about 20 times lower than the HM Q+G 2005, but their overall spectral shapes are similar. On the other hand, the HM Q+G 2005 and HM Q 2005 have different spectral shapes, especially at  $\leq 1$  Ryd around the H I ionisation edge, since the galaxy contribution is predominantly low-energy photons with energies  $< 1$  Ryd. Although the intensity of the HM Q+G 2012 is likely to be a factor of 3 to 5 too low at  $z \sim 0$ , it is consistent with other measurements at  $z \sim 2-3$ , the redshift range of our interest (Kollmeier et al. 2014; Shull et al. 2015).

The degree of ionisation depends on the intensity and spectral shape of the UVB as well as the density of the gas. The ionisation level depends mainly on the ionisation parameter  $U = n_{\gamma}/n_{\text{H}}$ , where  $n_{\gamma}$  is the number density of (hydrogen) ionising photons and  $n_{\text{H}}$  is the total (neutral and ionised) hydrogen volume density. For a chosen UVB and the observed  $N_{\text{H I}}$  as the stopping criterion of Cloudy, a determination of  $U$  is sufficient to derive the hydrogen density. In the low-density limit, the metallicity does not strongly affect the ionisation structure, but becomes important for the thermal balance since cooling is then dominated by the atomic line cooling rather than the recombination or bremsstrahlung. In the low-metallicity limit, the relative ionic ratio is independent of the metallicity (Osterbrock 1974).

We generated a grid of models for each H I+C IV+C III component trio. We varied  $[\text{C}/\text{H}]$  and  $n_{\text{H}}$  with a logarithmic step size of 0.1 or 0.05. For each absorber, the observed column densities with their fit errors and the Cloudy-predicted

column densities were compared for a given  $[C/H]$  and ionisation parameter  $U$  in order to find the best-fit model.

Figure 13 shows three such examples. The left panel shows a typical absorber in our sample, for which a well-measured single  $U$  matches  $N_{C_{IV}}$  and  $N_{C_{III}}$  simultaneously. All of our H I+C IV+C III sample without C II have a well-determined  $U$  and  $[C/H]$  regardless of a given UVB. Unsurprisingly, whenever C II is included, the Cloudy solution is not as good as the C II-free trios since the ionisation is now set by two ratios rather than one, so a single ionisation parameter may not provide an adequate description, if the spectral shape assumed for the ionising flux is incorrect, or if we are dealing with a multiphase medium. The middle and right panels of Fig. 13 show two of such examples under the HM Q+G 2012 UVB. In the middle panel, a single  $U$  matches the observed column density of C IV, C III and C II within errors. On the other hand, the right panel shows the worst case in our sample, in that no single best-fit  $U$  is found to reproduce the observation within errors. This absorber is fit slightly better for the HM Q 2005, but not significantly.

#### 4.3 Caveats

In the presence of the UV background, when a metal-enriched hot gas cools down or is mixed with the low-density H I, these processes result in a change in the thermal and ionisation states of the metal-enriched gas, a departure from an equilibrium state. As a result, even for the same H I column density ranges at  $\log N_{H I} \in [13, 15]$ , C IV-enriched H I is expected to have a higher gas temperature and a higher  $[C/H]$  than the typical Ly $\alpha$  forest, whether C IV is collisionally ionised or photoionised (Cen & Chisari 2011; Shen et al. 2013). However, the degree of this departure from photoionisation equilibrium in the metal-enriched forest gas is not observationally constrained (Haehnelt et al. 1996; Oppenheimer et al. 2012), and this is one of our objectives in this study.

At  $z \sim 2.4$  and at the cosmic mean density,  $\log n_H \sim -6.72 + 3 \times \log(1+z) \sim -5.13$  (Wiersma et al. 2009). For an absorber below this density, the Hubble expansion should be taken into account. The density of most C III absorbers in our sample is  $-5 < \log n_H < -4$  as shown in Section 5.1. For most C III absorbers, the Hubble expansion does not play a significant role.

In addition, for the HM Q+G 2012, the photoionisation time scale is  $1/\Gamma_{H I} \sim 1.04 \times 10^{12} \text{ sec} \sim 3.3 \times 10^4 \text{ yrs}$ , where  $\Gamma_{H I}$  is the H I photoionisation rate (Haardt & Madau 2012). The dynamical time scale is  $t_{\text{dyn}} = 1/\sqrt{G\rho} \sim 1.16 \times 10^{10} \text{ yrs}$ , where  $G$  is the gravitational constant and  $\rho$  is the gas mass density (Schaye 2001). The photoionisation time scale is much shorter than the dynamical time scale. Therefore, we ignore the Hubble expansion and any dynamical evolution in the photoionisation model, i.e. assuming a static absorber.

Of 32 tied trios, 4 trios are found to be associated clearly with C II  $\lambda 1334$  or  $\lambda 1036$  or both. While 20 C III absorbers have absorption-free C II regions, therefore, a reliable  $N_{C_{II}}$  upper limit, 8 C III absorbers have the C II region of  $\lambda 1334$  and  $1036$  blended or unreliable, as noted in Table A2. Four trios with C II have highest  $N_{C_{III}}/N_{C_{IV}}$  values as well as the lower gas temperature at  $\log T_b \leq 4.17$ . There are no other clear distinctions between C II absorbers and upper-limit- $N_{C_{II}}$  absorbers. Since 8 C III absorbers with a blended C II

region have a lower  $N_{C_{III}}/N_{C_{IV}}$  and higher  $T_b$ , we expect them to have  $N_{C_{II}}$  similar to our assumed  $N_{C_{II}}$  detection limit of  $\log N_{C_{II}} \sim 12.0$ , if they are associated with C II.

#### 4.4 Results and systematic uncertainties

The Cloudy results of the 32 tied components are tabulated in Table A2 for the HM Q+G 2012, including the observed column densities with their fit errors.

Yielding a formal  $1\sigma$  error of Cloudy-predicted parameters is not trivial, since they are correlated without errors. Instead, we use a rough acceptable ranges of  $[C/H]$  and  $\log U$  as a  $[C/H]$  error and as a *relative* error substitute for other parameters. As seen in Fig. 13, the predicted column density has an upward parabola curve as a function of  $\log U$ . When an observed column density error is small and the intercepting  $U$  is located in the steeper side of the parabola curve, both  $[C/H]$  and  $\log U$  can be estimated within 0.05 dex. On the other hand, when the observed column density error is large and the intercepting  $U$  occurs at near the flatter top of the upward parabola curve,  $\log U$  is less sharply estimated, with larger than 0.1 dex for an acceptable  $\log U$  range. In general,  $[C/H]$  is better estimated than  $U$ . About 47% of the sample under the HM Q+G 2012 have both  $[C/H]$  and  $\log U$  estimates within 0.05 dex.

In the following analysis, the plotted error on the Cloudy-predicted parameters except  $[C/H]$  are *not real*  $1\sigma$  errors, but just an illustration based on the uncertainty on  $\log U$ , i.e. a larger acceptable  $\log U$  range translates into a larger, *assumed* relative error.

#### 4.5 The UV backgrounds

Figure 14 presents the comparisons of the predicted parameters  $[C/H]$  and  $T$  between the three UVBs used. Any differences in the inferred carbon abundance or the temperature are effectively just a small rescaling, with the absorbers having C II being somewhat discrepant in the HM Q+G 2005 and the HM Q 2005 cases. When considered only C IV and C III excluding C II,  $[C/H]$  and  $\log U$  of the 4 C IV+C III+C II absorbers are lower by  $\sim 0.2$  dex and higher by  $\sim 0.3$  dex, respectively. Their Cloudy-predicted parameters (sky-blue squares) are also perfectly on the one-to-one relation with other C II-free absorbers. Other parameters such as the total hydrogen volume density and the line-of-sight length also have a similar behaviour. In short, the predicted physical parameters for one of the UVBs can be roughly scaled from the ones for the other two UVBs. As long as each absorber is exposed to a similar UVB (one of our assumptions), the evidence for bimodal distributions of observed and derived physical parameters does not depend on which of the three HM UVBs is used, though the absolute values of each derived parameter do.

We note that the 4 C II absorbers fit slightly better to the HM Q 2005 background than both HM Q+G UVBs, in particular, the  $z = 2.462044$  absorber toward Q0002-422. However, this does not necessarily imply that all tied C III absorbers are exposed to the UVB similar to the HM Q 2005. Considering that the shape of the UVB at high redshifts is not observationally well constrained, all the assumed UVBs are equally adequate for our data within more realistic errors.

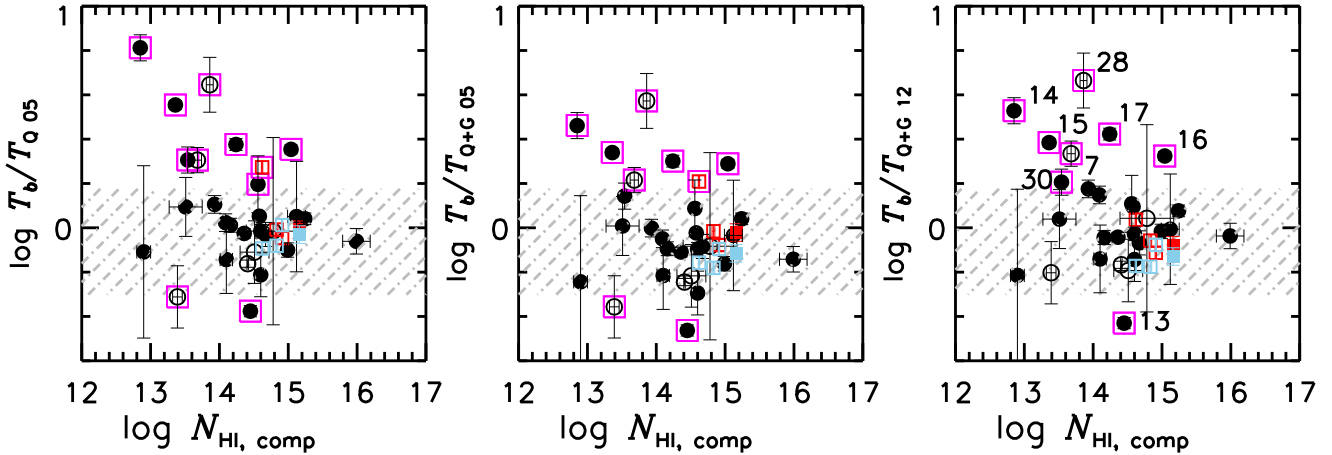


**Figure 15.** Ratio of the VPFIT-derived temperature  $T_b$  based on Eq. 1 to the Cloudy-predicted temperature  $T_{Q\ 05}$ ,  $T_{Q+G\ 05}$  and  $T_{Q+G\ 12}$  for the HM Q 2005 (left panel), the HM Q+G 2005 (middle panel) and the HM Q+G 2012 (right panel) as a function of  $N_{\text{HI}}$  of a HI component. Symbols are the same as in Fig. 14. Errors on the ratio are based only on the  $T_b$  errors. The gray-shaded region indicates the difference between  $T_b$  and Cloudy-derived  $T_{\text{PIE}}$  less than 50%. Data points embedded in a magenta open square are the absorbers which have more than 50% difference between the two temperatures. In the right panel, a number noted next to the data points embedded in a magenta open square is an absorber number listed in Tables A2 and A3.

#### 4.6 Validity of the photoionisation modelling

A way to check whether or not C III absorbers are in photoionisation equilibrium (PIE) is to compare the VPFIT-derived gas temperatures  $T_b$  from Eq. 1 and the Cloudy-predicted temperatures. Figures 15 and 16 present the ratio of  $T_b$  and Cloudy-predicted temperatures  $T_{\text{PIE}}$  as a function of  $N_{\text{HI}}$ , and of  $z$  and  $T_b$ , respectively.

In Fig. 15, most data points are reasonably close to the  $T_b/T_{\text{PIE}} = 1$  line, but there are some outliers, with about 25% of the C III absorbers having a temperature difference  $T_b - T_{\text{PIE}}$  larger than 50% of the Cloudy model temperature  $T_{\text{PIE}}$ . The absorbers with a large temperature difference have a higher  $N_{\text{C IV}}$  than the one with a similar  $N_{\text{HI}}$ . For  $\log N_{\text{HI}} \geq 14$ , in most cases  $T_b/T_{\text{PIE}} \sim 1$ , implying that the absorbers are roughly in PIE. It is not straightforward to draw any clear conclusions at  $\log N_{\text{HI}} \leq 14.0$  as there are only a few data points, but they seem to show larger departures from PIE.

In most cases, C III absorbers with a large departure from PIE show a higher  $T_b$  than the PIE-predicted  $T_{\text{PIE}}$ . As the PIE temperature is determined by photoionisation heating and atomic line cooling in the low-density limit, a higher observed temperature  $T_b$  compared to  $T_{\text{PIE}}$  strongly suggests that these absorbers are exposed to additional heating source compared to other absorbers having  $T_b$  more closer to their PIE temperature.

The median temperature ratio is  $(T_b/T_{Q\ 05})_{\text{med}} = 1.03$ ,  $(T_b/T_{Q+G\ 05})_{\text{med}} = 0.92$  and  $(T_b/T_{Q+G\ 12})_{\text{med}} = 0.97$ , respectively. The mean temperature ratio is  $\langle T_b/T_{Q\ 05} \rangle = 1.46 \pm 1.26$ ,  $\langle T_b/T_{Q+G\ 05} \rangle = 1.11 \pm 0.74$  and  $\langle T_b/T_{Q+G\ 12} \rangle = 1.31 \pm 0.90$ , respectively. These values indicate that overall in our sample, the HM Q+G 2012 produces the predicted temperature similar to the observed  $T_b$ , while the HM Q 2005 has the largest number of the discrepant absorbers, 10 out of 32 absorbers. This is why the HM Q+G 2012 was taken as a fiducial UVB. However, we note that the HM Q

2005 predicts a better match for the cluster of data points at  $\log N_{\text{HI}} \in [14, 15]$ .

The left panel of Fig. 16 shows that the VPFIT and Cloudy temperatures differ most often at lower  $z$ , though the small number of components at  $z > 2.6$  means that we cannot draw any firm conclusions. The right panel of Fig. 16 implies that most absorbers have  $\log T_{Q+G\ 12} \sim 4.5$  due to the imposed PIE condition at low  $[\text{C}/\text{H}]$  (see Section 5.2). Absorbers with a large temperature discrepancy tend to have a larger  $T_b$ .

The combining results from  $T_b/T_{\text{PIE}}$  as a function of  $N_{\text{HI}}$  and  $z$  suggest that C III component trios with  $\log N_{\text{HI}} \leq 14$  or at lower redshifts are less likely to be in PIE.

#### 4.7 The photoionisation modelling with a fixed temperature

Since the gas temperature derived from the  $b$  parameter is a direct estimate from the observations, the Cloudy-predicted PIE temperature may not be appropriate. Therefore, another set of the Cloudy grid models was run with the fixed constant temperature  $T_b$  for each C III absorber. We used only the HM Q+G 2012 for the fixed  $T_b$  model, since predicted parameters for a different HM UVB can be roughly scaled from the HM Q+G 2012 and any correlations between parameters are not altered significantly due to a different UVB among the three HM UVBs.

Figure 17 compares the carbon abundance  $[\text{C}/\text{H}]$ , ionisation parameter  $U$ , hydrogen density  $n_{\text{H}}$  and line-of-sight length  $L$  for PIE and non-PIE (with a fixed temperature  $T_b$ ) models. As expected, the 8 absorbers embedded in a magenta open square display larger discrepancies, while the remaining 24 absorbers do not show any significant difference. This is due to the fact that for a low-density, low-metallicity PIE gas, the internal thermal balance is independent of  $n_{\text{H}}$  but sensitive to the relative abundance of ions.

The mean departure from PIE is  $\langle \Delta[\text{C}/\text{H}] \rangle = -0.04 \pm$

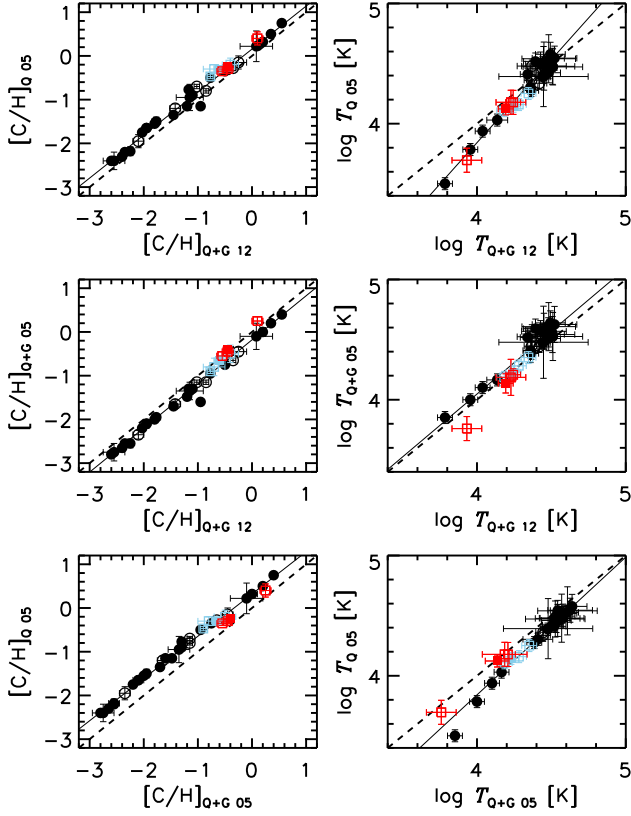


**Figure 14.** Comparisons between the three HM UVBs for the carbon abundance  $[C/H]$  (left panels) and the temperature (right panels). Red squares indicate the 4 C III absorbers with C II, while black circles are the C II-free absorbers. Sky-blue squares indicate the 4 C II absorbers, when only C IV and C III are considered without C II. Filled and open symbols are for the certain and uncertain absorbers listed in Table A1. Only errors larger than the symbol size are plotted. The dashed line represents equality in the quantities, and the thin solid line is a least-square fit to the results:  $[C/H]_{Q05} = 0.16 + 0.98 \times [C/H]_{Q+G12}$ ,  $\log T_{Q05} = -1.69 + 1.38 \times T_{Q+G12}$ ,  $[C/H]_{Q+G05} = -0.18 + 1.00 \times [C/H]_{Q+G12}$ ,  $\log T_{Q+G05} = -0.13 + 1.05 \times T_{Q+G12}$ ,  $[C/H]_{Q05} = 0.32 + 0.97 \times [C/H]_{Q+G05}$ ,  $\log T_{Q05} = -0.74 + 1.15 \times T_{Q+G05}$ , respectively. Refer to the online version for clarity.

$0.16$ ,  $\langle \Delta \log U \rangle = -0.02 \pm 0.14$ ,  $\langle \Delta \log n_H \rangle = 0.02 \pm 0.14$ , and  $\langle \Delta \log L \rangle = 0.05 \pm 0.36$ , respectively. While the mean departure from PIE is negligible, the scatter is not. The line-of-sight length  $L = N_H/n_H$  shows the largest departure, as  $L \propto T^{0.41}$  and other parameters have a smaller  $T$  dependence (Schaye 2001).

## 5 DERIVED PROPERTIES OF THE WELL-ALIGNED H I + C IV + C III COMPONENTS

In this section, we present our main results based on the non-PIE Cloudy modelling with a fixed temperature  $T_b$  for the HM Q+G 2012 UVB. Whenever necessary, the difference from the PIE model is also discussed. Predicted parameters for the PIE assumption, i.e. a free-fit temperature model, are subscripted with “PIE”, while parameters from the non-

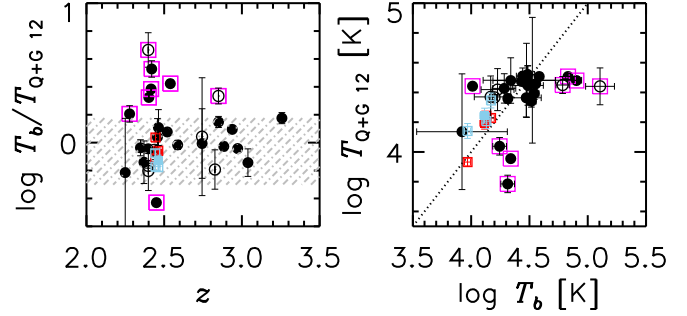


**Figure 16.** The ratio of  $T_b$  and the Cloudy-predicted  $T_{PIE}$  as a function of  $z$  (left panel) and of  $T_b$  (right panel) for the fiducial HM Q+G 2012. All other symbols are the same as in Fig. 15.

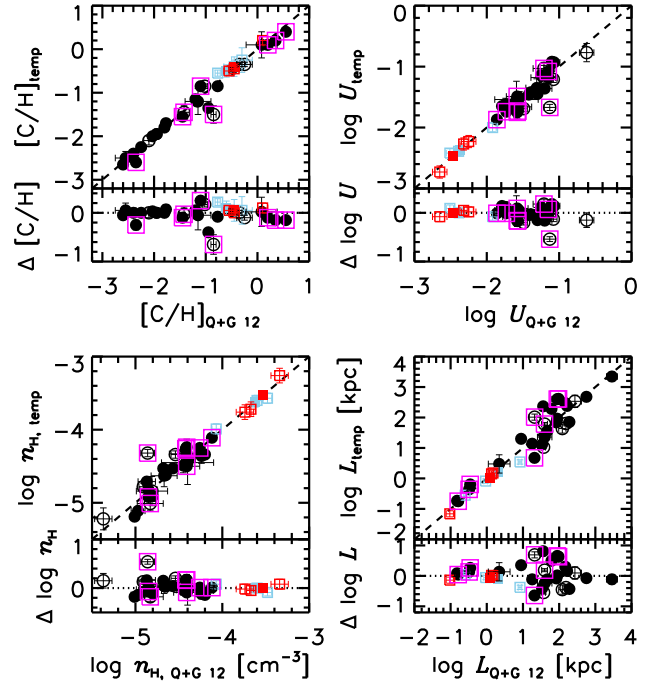


**Figure 17.** Comparisons between the PIE (x-axis) and the non-PIE (y-axis) models for the fiducial HM Q+G 2012 UVB. The non-PIE model is set to have a fixed temperature  $T_b$  derived by VPFIT based on Eq. 1. Filled and open symbols represent the certain and uncertain absorbers. Data points embedded with a magenta open square are the absorbers for which the Cloudy-predicted  $T_{Q+G12}$  is 50% larger or smaller than  $T_b$ . Plotted errors on  $[C/H]$  are an error based on an allowed  $[C/H]$  range, while the ones on other predicted parameters are based on an allowed  $\log U$  range. The difference between the non-PIE  $T_b$  and the PIE models is illustrated in the lower part of each panel. All other symbols are the same as in Fig. 14. Refer to the online version for clarity.

PIE  $T_b$  model are noted with a subscript “temp”. The column density range for the 32 tied H I + C IV + C III component trios is  $\log N_{H1} \in [12.9, 16.0]$ ,  $\log N_{CIV} \in [11.8, 13.8]$  and  $\log N_{CIII} \in [11.7, 13.8]$ , respectively. For the 4 absorbers, C II  $\lambda 1334$  or  $\lambda 1036$  or both is also detected at  $\log N_{CII} \in [12.2, 12.7]$ .

Note that apart from the observed column density and

$b$  value of H I and C IV along with the gas temperature  $T_b$ , all of the parameters presented in this Section are Cloudy-predicted. We also stress that despite all the caveats in the Cloudy-modelling and a choice of the UVB discussed in Section 4, our main results are not altered by them.

### 5.1 Carbon abundance, $N_{\text{H I}}$ , $N_{\text{C IV}}$ and line-of-sight length

Among the correlations between various observed and predicted parameters, two of the most unexpected correlations are presented in Fig. 18. In the upper left panel, the line-of-sight length,  $L = N_{\text{H}}/n_{\text{H}}$ , is shown as a function of  $N_{\text{C IV}}$  for the non-PIE model. The lower left panel presents the same parameter space for the PIE model, with the middle left panel displaying the difference between the two models. As  $L$  is dependent on  $T^{0.41}$  (Schaye 2001), which is also dependent on  $U$  and  $[\text{C}/\text{H}]$ , there is a larger difference between the non-PIE  $T_b$  and PIE models shown in the middle left panel.

In both left panels, despite a few interlopers, the  $N_{\text{C IV}}-L$  plane can be clearly divided into two regions, suggesting that our optically-thin C III absorbers may consist of two distinct populations. 14 absorbers embedded in a green open circle have  $L_{\text{temp}} = 20-480$  kpc, with the median  $L_{\text{temp}}$  of 233 kpc. For these absorbers,  $L_{\text{temp}}$  is a weak function of  $N_{\text{C IV}}$ . On the other hand, 12 absorbers embedded in a blue open circle have  $L_{\text{temp}} \leq 20$  kpc, showing that  $L_{\text{temp}}$  increases rapidly with  $N_{\text{C IV}}$  at  $\log N_{\text{C IV}} \in [12.2, 13.5]$ . The yellow-shaded (gray-shaded) region illustrates a least-square fit to the data points embedded in a blue (green) open circles, and the fit results are tabulated in Table 3.

A similar behaviour is seen in the  $[\text{C}/\text{H}]-N_{\text{C IV}}$  relation in the upper and lower right panels of Fig. 18, where there is a segregation of C III absorbers into two distinct regions as a high- or a low-metallicity branch, divided at  $[\text{C}/\text{H}]_{\text{temp}} \sim -1.0$ . Again, the yellow-shaded (gray-shaded) region shows a fit to the data points embedded in a blue (green) open circles as in the left panels, with the fit results listed in Table 4.

Most C III absorbers having  $L_{\text{temp}} \sim 200$  kpc have  $[\text{C}/\text{H}]_{\text{temp}} \leq -1.0$ , which increases with  $N_{\text{C IV}}$ . As noted in Tables A2 and A3, none of these low-metallicity branch absorbers is associated with Si IV, which is usually found with C IV at  $\log N_{\text{C IV}} \geq 13.0$  (Shen et al. 2013). These low-metallicity branch absorbers have a saturated H I Ly $\alpha$  absorption profile with a weak C IV. The C III components at  $v = 0$  km s $^{-1}$  in the second panel of Fig. 1 provides a good example of low-metallicity branch absorbers.

Absorbers with a higher  $[\text{C}/\text{H}]_{\text{temp}}$  show an opposite trend in that  $[\text{C}/\text{H}]_{\text{temp}}$  anti-correlates with  $N_{\text{C IV}}$ . High-metallicity branch absorbers further seem to be grouped into two subclasses, 1) part of a multi-component, strong C IV complex with a saturated H I Ly $\alpha$  or 2) associated with a strong C IV and unsaturated H I Ly $\alpha$ . Most of the former subclass, complex high-metallicity branch absorbers, are associated with Si IV. The C III components at  $v = +52$  and  $v = -75$  km s $^{-1}$  in the right panel of Fig. 1 are an example of high-metallicity branch absorbers, which is part of a C IV complex. A good example of the latter subclass, simple high-metallicity branch absorbers, is shown in the left panel of Fig. 1. However, on top of a small-number statistics, sim-

**Table 3.** Least-square fit coefficients for the non-PIE  $L_{\text{temp}}$  as a function of  $N_{\text{C IV}}$  and  $N_{\text{H I}}$ :  $\log L_{\text{temp}} = A + B \log N_X$ . The parameters are associated with the left panel of Figs. 18 and 24.

ion $X$	$A$	$B$	Branch
C IV (yellow)	$-28.11 \pm 1.88$	$2.17 \pm 0.52$	High-metallicity
C IV (gray)	$-4.67 \pm 1.42$	$0.55 \pm 0.40$	Low-metallicity
H I (all)	$-10.71 \pm 0.95$	$0.84 \pm 0.25$	
H I (yellow)	$-6.86 \pm 0.91$	$0.50 \pm 0.24$	High-metallicity
H I (gray)	$-0.78 \pm 1.01$	$0.20 \pm 0.26$	Low-metallicity

ple high-metallicity branch absorbers sometimes occur in the vicinity of complex high-metallicity branch absorbers. Therefore, our data cannot clearly distinguish the two subclasses, however, suggest that high-metallicity branch absorbers could be a mixed bag of more kinematically complex absorbers than low-metallicity branch ones.

In Fig. 18, 4 sky-blue circles are C II absorbers when  $N_{\text{C II}}$  is excluded, i.e. C II absorbers are treated as C II-free absorbers. No significant difference is found between the two subsamples, in that no C II high-metallicity branch absorbers become low-metallicity branch absorbers even if C II was ignored. This implies that the overall observational trends would hold, even if some of upper-limit- $N_{\text{C II}}$  or blended-C II absorbers are in fact associated with C II. Since a similar behaviour is found for other correlations, no further consideration on possibly missed C II above the C II detection limit is included. However, we present the Cloudy-predicted parameters of 4 C II absorbers when excluded C II as sky-blue symbols if appropriate.

For high-metallicity branch absorbers, as there are correlations between  $[\text{C}/\text{H}]_{\text{temp}}$  and  $N_{\text{C IV}}$  as well as  $L_{\text{temp}}$  and  $N_{\text{C IV}}$ , a correlation between  $[\text{C}/\text{H}]_{\text{temp}}$  and  $L_{\text{temp}}$  is also expected. This is shown in the left panel of Fig. 19. Although overall an anti-correlation can be assumed, low-metallicity branch absorbers show a large spread of 1 dex in  $\log L_{\text{temp}}$  for a given  $[\text{C}/\text{H}]_{\text{temp}}$  at  $[\text{C}/\text{H}]_{\text{temp}} \leq -1.0$ . Due to the large scatter, low-metallicity branch absorbers at  $[\text{C}/\text{H}]_{\text{temp}} \leq -1.0$  can be viewed as having almost a constant  $L_{\text{temp}}$  at  $L_{\text{temp}} \sim 200$  kpc, in good agreement with the conclusion from the  $N_{\text{C IV}}-L_{\text{temp}}$  relation. The 4 C II-free super-solar- $[\text{C}/\text{H}]_{\text{temp}}$  absorbers including the 3 absorbers with a highest  $T_b - T_{\text{PIE}}$  value have a smallest  $L_{\text{temp}} \leq 1$  kpc. They are all simple high-metallicity branch absorbers, characterised by a stronger C IV than typical H I absorbers with a similar  $N_{\text{H I}}$ .

The right panel of Fig. 19 presents  $L_{\text{temp}}$  as a function of total (neutral + ionised) hydrogen volume density  $n_{\text{H, temp}}$ . Low-metallicity branch absorbers have a lower  $\log n_{\text{H, temp}} \in [-5.2, -4.3]$  with a mean of  $\langle \log n_{\text{H, temp}} \rangle = -4.70 \pm 0.28$ , slightly higher than the cosmic mean number density at  $z \sim 2.4$ . High-metallicity branch absorbers have a higher  $n_{\text{H, temp}}$  ranged at  $\log n_{\text{H, temp}} \in [-4.5, -3.3]$ . Compared to the warm ionised gas in the Milky Way with a comparable temperature range, our C III absorbers have about two orders of magnitude lower  $n_{\text{H, temp}}$  (Haffner et al. 2009). The 4 C II-free absorbers with  $L_{\text{temp}} \leq 1$  kpc, marked with an absorber number next to the data points, have a smaller  $L_{\text{temp}}$  than expected from the fit for  $\log n_{\text{H, temp}} \sim -4.2$ .

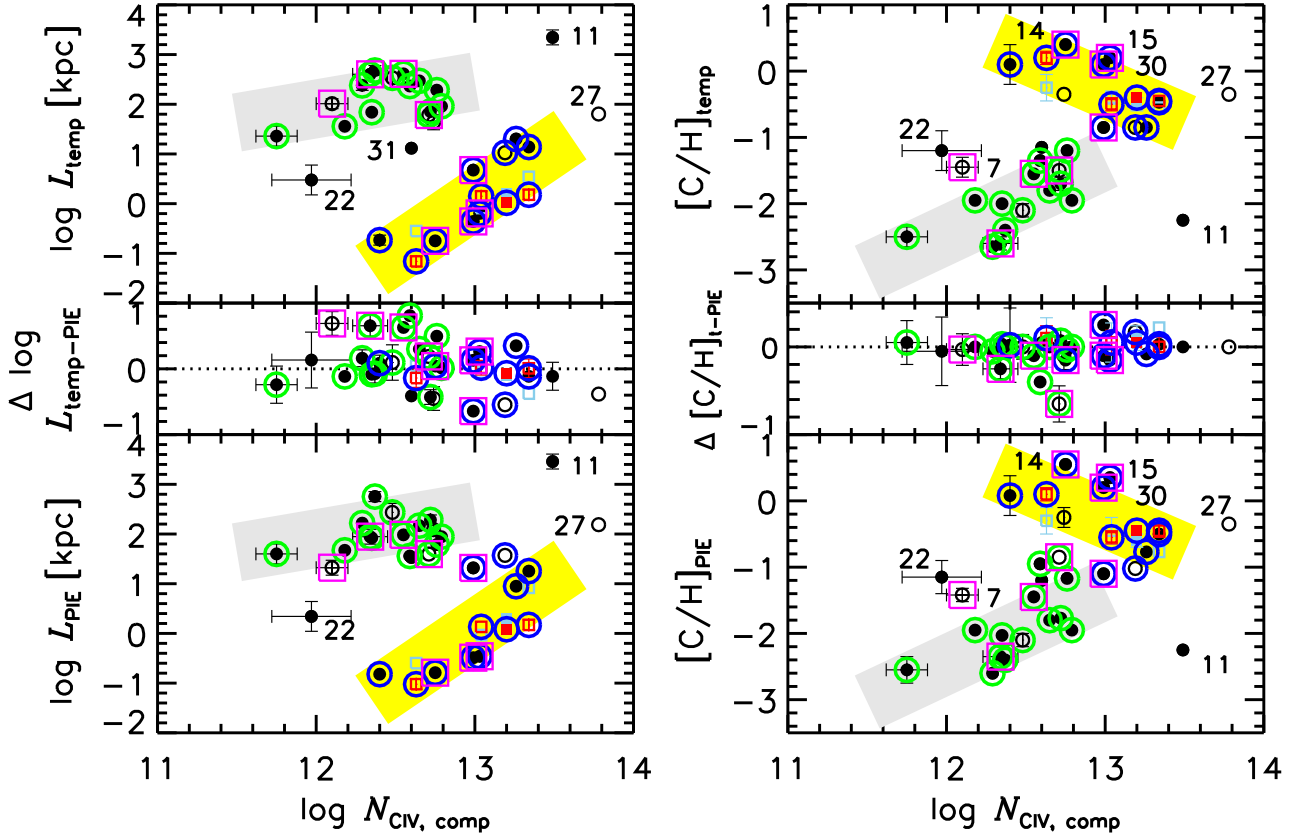


**Figure 18.** *Upper panels:* the line-of-sight length  $L_{\text{temp}}$  (left) and  $[C/H]_{\text{temp}}$  (right) as a function of  $N_{\text{CIV}}$  of 32 tied components. All the symbols are the same as in Fig. 17. Errors on  $\log L_{\text{temp}}$  and  $[C/H]_{\text{temp}}$  are the allowed  $\log U$  and  $[C/H]_{\text{temp}}$  range, respectively, and are shown only when they are larger than the symbols. The yellow-shaded (gray-shaded) region represents the fit to the data points embedded in a blue (green) open circle for the non-PIE model. An absorber number next to the data points is the same one listed in Tables A2 and A3. *Middle panels:* the difference between the non-PIE  $T_b$  and PIE models for the HM Q+G 2012. *Lower panels:* for the PIE model. The yellow-shaded and gray-shaded regions are the same ones as in the upper panels. Refer to the online version for clarity.

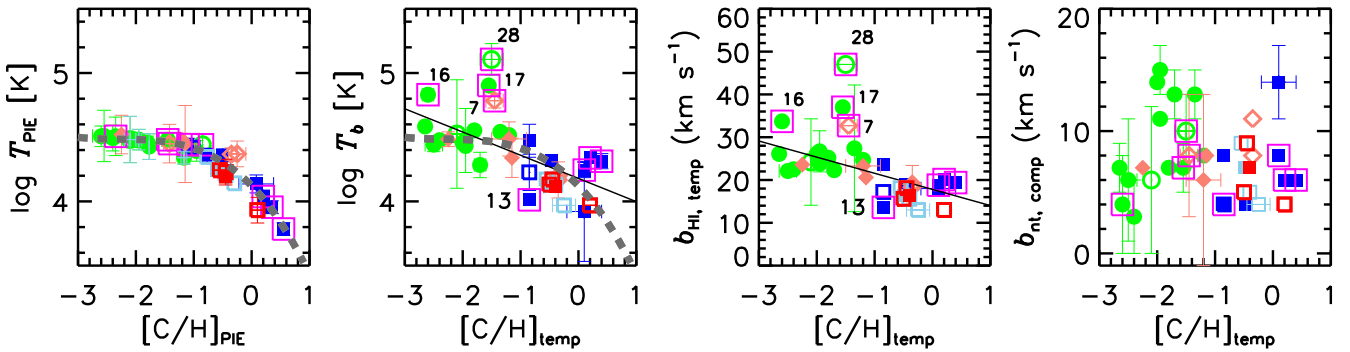


**Figure 20.** *Left panel:* the PIE temperature  $T_{\text{PIE}}$  versus  $[C/H]_{\text{PIE}}$  for the fiducial HM Q+G 2012. The overlaid dark gray dashed curve is a polynomial fit to the temperature vs metallicity,  $T_{\text{PIE}} = 4.12 - 0.46 \times [C/H]_{\text{PIE}} - 0.20 \times [C/H]_{\text{PIE}}^2 - 0.03 \times [C/H]_{\text{PIE}}^3$ . Plotted errors on  $[C/H]_{\text{PIE}}$  are an error based on an allowed  $[C/H]$  range, while the ones on other predicted parameters are based on an allowed  $\log U$  range. All the symbols are the same as in Fig. 19. *Second panel:* the predicted carbon abundance  $[C/H]_{\text{temp}}$  for the non-PIE model with a fixed temperature  $T_b$  versus  $T_b$ . The solid line is the least-square-fit to the data:  $\log T_b = (4.18 \pm 0.06) + (-0.18 \pm 0.04) \times [C/H]_{\text{temp}}$ . The dark gray dashed curve is the PIE relation shown in the left panel. *Third panel:* the observed total (thermal and non-thermal) line width of H I as a function of  $[C/H]_{\text{temp}}$ . The solid line is the least-square fit:  $b_{\text{HI}} = (17.80 \pm 1.78) + (-3.77 \pm 0.76) \times [C/H]_{\text{temp}}$ . *Right panel:* the derived non-thermal line width  $b_{\text{nt}}$  as a function of  $[C/H]_{\text{temp}}$ . Refer to the online version for clarity.

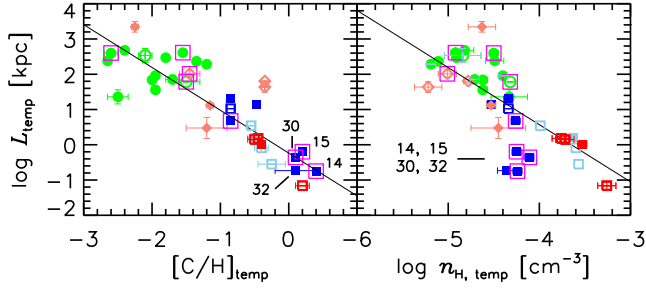


**Figure 19.** *Left panel:* the line-of-sight length  $L_{\text{temp}}$  as a function of  $[C/H]_{\text{temp}}$ . Green circles and blue squares indicate low-metallicity and high-metallicity branch absorbers, with filled and open symbols being for certain and uncertain absorbers. C III absorbers which do not clearly belong to either branch are shown as filled and open orange diamonds. Red squares are for C II absorbers (belonging to high-metallicity branch absorbers), while sky-blue squares are the same C II absorbers when C II is excluded in the Cloudy modelling. The solid line is a least-square fit to the full sample,  $\log L_{\text{temp}} = -0.24 - 1.21 \times [C/H]_{\text{temp}}$ . *Right panel:*  $L_{\text{temp}}$  as a function of a total (neutral + ionised) hydrogen volume density  $n_{\text{H}, \text{temp}}$ . The least-square fit is  $\log L_{\text{temp}} = -5.91 - 1.62 \times \log n_{\text{H}, \text{temp}}$ . Refer to the online version for clarity.

**Table 4.** Least-square fit coefficients for the non-PIE  $[C/H]_{\text{temp}}$  as a function of  $N_{\text{CIV}}$  and  $N_{\text{HI}}$ :  $[C/H]_{\text{temp}} = A + B \log N_X$ . The parameters are associated with the right panel of Figs. 18 and 24.

ion $X$	$A$	$B$	Branch
C IV (yellow)	$13.19 \pm 1.30$	$-1.04 \pm 0.36$	High-metallicity
C IV (gray)	$-16.01 \pm 1.19$	$1.13 \pm 0.34$	Low-metallicity
H I (all)	$10.04 \pm 0.72$	$-0.78 \pm 0.19$	
H I (yellow)	$5.39 \pm 0.50$	$-0.40 \pm 0.13$	High-metallicity
H I (gray)	$11.39 \pm 0.59$	$-0.91 \pm 0.15$	Low-metallicity

## 5.2 Carbon abundance, temperature, $b_{\text{HI}}$ , $b_{\text{nt}}$ , $N_{\text{CIV}}/N_{\text{HI}}$

Relations between the carbon abundance  $[C/H]_{\text{temp}}$  and various parameters are shown in Fig. 20. The left panel illustrates a PIE gas for the HM Q+G 2012 background. For a low-density gas in the presence of a UVB, the ratio of ionic abundances does not depend on the metallicity at less than  $10^{-1}$  solar, i.e.  $[C/H]$  does not play a significant role in the internal ionisation structure. A gas at higher temperature cools to an equilibrium temperature  $T_{\text{eq}}$  and a gas at lower temperature gets heated to  $T_{\text{eq}}$ . This temperature for the HM Q+G 2012 is  $\log T_{\text{eq}} \sim 4.5$ , as clearly seen in the left panel. As expected, low-metallicity branch absorbers marked as green symbols have a temperature around  $T_{\text{eq}}$ . When the metallicity is higher than  $10^{-1}$  solar, the radiative metal line cooling becomes important, which decreases  $T_{\text{eq}}$ . A slight departure from the general trend by C II-enriched absorbers is due to their higher  $n_{\text{H}}$ .

In the second panel of Fig. 20, the relation between  $[C/H]_{\text{temp}}$  and  $T_b$  is not as clear as in the left panel, due to the non-PIE condition. A large departure from the  $[C/H]_{\text{PIE}}-T_{\text{PIE}}$  relation occurs for C III absorbers with a large temperature difference between  $T_b$  and  $T_{\text{PIE}}$ . The

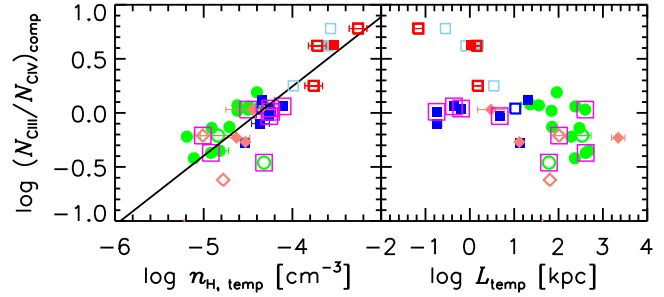


**Figure 21.** The ratio of observed C III column density and C IV column density as a function of the total hydrogen volume density (left panel) and  $L_{\text{temp}}$  (right panel). Symbols are the same as in Fig. 20. The least-square fit in the left panel is  $\log N_{\text{CIII}}/N_{\text{CIV}} = 2.81 + 0.64 \times \log n_{\text{H}, \text{temp}}$ . Refer to the online version for clarity.

higher  $T_b$  than  $T_{\text{eq}}$  for all but one of these absorbers suggests that they have a higher heating rate, i.e. experiencing a recent cooling from a hotter gas or exposed to additional radiation.

The observed total (thermal and non-thermal)  $b_{\text{HI}}$  increases weakly as  $[C/H]_{\text{temp}}$  decreases, as seen in the third panel. Naturally, absorbers with a higher  $T_b$  tend to have a higher  $b_{\text{HI}}$ , as the non-thermal contribution to the observed line width is not significant. There is no clear trend between  $[C/H]_{\text{temp}}$  and non-thermal motion  $b_{\text{nt}}$  in the right panel.

The left panel of Fig. 21 implies that  $N_{\text{CIII}}/N_{\text{CIV}}$  increases with the total hydrogen volume density. On the other hand, the right panel shows that the line-of-sight length of high-metallicity branch absorbers is mostly independent of  $N_{\text{CIII}}/N_{\text{CIV}}$  at  $L_{\text{temp}} \leq 20$  kpc. Low-metallicity branch absorbers at  $L_{\text{temp}} \geq 20$  kpc tend to be  $N_{\text{CIII}}/N_{\text{CIV}} \leq 1$ , simply because that they have  $\log N_{\text{CIV}} \leq 13$  (Fig. 6). When combined the left panel with the right one, low-metallicity branch absorbers tend to have a lower  $n_{\text{H}, \text{temp}}$  at a larger  $L_{\text{temp}}$ , a good agreement with what simulations have predicted (Cen & Chisari 2011; van de Voort et al. 2011; Shen et al. 2013).

## 5.3 Redshift evolution of carbon abundance

Despite the small number of absorbers at  $z > 2.6$ , we checked whether there is noticeable redshift evolution in the  $[C/H]_{\text{temp}}$  distribution. Figure 22 shows the redshift distribution of  $[C/H]_{\text{temp}}$ , and, to represent it in another way, the number of C III absorbers as a function of  $[C/H]_{\text{temp}}$  for redshift ranges  $2.1 < z < 2.6$  and  $2.6 < z < 3.4$  as well as for the whole sample.

At  $z \sim 2.4$  in the upper left panel, the C III absorbers display a large range of the carbon abundance at  $[C/H]_{\text{temp}} \in [-2.7, 0.4]$ . The mean  $[C/H]_{\text{temp}}$  is  $-1.0 \pm 1.0$ . On the other hand, at  $z \sim 2.9$ , the C III absorbers show a smaller  $[C/H]_{\text{temp}}$  range at  $[C/H]_{\text{temp}} \in [-2.1, -0.9]$ , with  $\langle [C/H]_{\text{temp}} \rangle = -1.6 \pm 0.4$ . At both redshifts, the  $[C/H]_{\text{temp}}$  distribution is not Gaussian. The two-sided Kolmogorov-Smirnov statistic gives the significance level of 0.02, implying that the  $[C/H]_{\text{temp}}$  distribution at the two redshift ranges is significantly different.

At  $z \sim 2.9$ , a lack of data points at  $[C/H]_{\text{temp}} \leq -2$

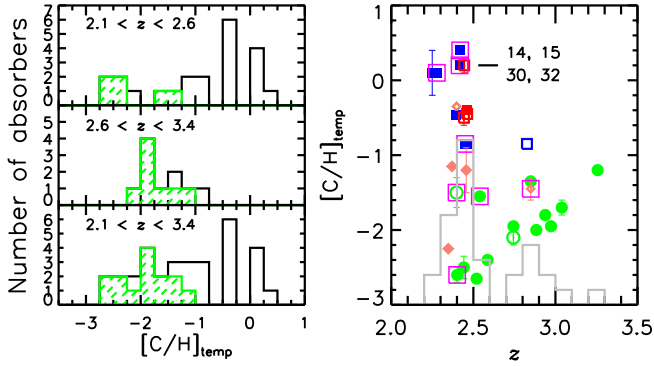


**Figure 22.** *Left panel:* the number of absorbers as a function of  $[C/H]_{\text{temp}}$  at the three different redshift bins. The green-shaded region is for low-metallicity branch C III absorbers. *Right panel:* the redshift distribution of  $[C/H]_{\text{temp}}$ . The overlaid gray histogram based at  $-3$  in the y-axis is the number of absorbers in  $\Delta z = 0.1$  bins. Symbols are the same as in Fig. 21.

is probably due to lower-S/N data and a smaller number of sightlines. However, a lack of absorbers at  $[C/H]_{\text{temp}} \in [-0.8, 0.4]$  is not an observational bias, since these absorbers have a stronger C IV compared to a typical absorber with a similar  $N_{\text{HI}}$ , thus easy to detect. At  $z \sim 2.4$ , high-metallicity branch absorbers account for about 50% of C III absorbers. If a relative fraction of  $[C/H]_{\text{temp}}$  is similar at both redshift ranges,  $5 \pm 2$  absorbers with  $[C/H]_{\text{temp}} \in [-0.8, 0.4]$  are expected at  $z \sim 2.9$ . Therefore, this lack of high-metallicity branch absorbers at  $z \sim 2.9$  is probably real. In short, the  $[C/H]_{\text{temp}}$  distribution is more skewed toward a higher  $[C/H]_{\text{temp}}$  at lower  $z$ , implying a metallicity evolution.

The simulated temperature distribution by Cen & Chisari (2011) is similar to the observed one shown in Section 3.3. The same simulation predicts that for  $\log N_{\text{CIV}} \in [12, 14]$ , the metallicity distribution has a narrow (broad) Gaussian distribution covering  $-3.0 \sim -1.0$  ( $-3.0 \sim -0.5$ ) with a peak at  $-2.1$  ( $-2.0$ ) at  $z = 4$  ( $z = 2.6$ ). This is roughly consistent with the Cloudy-predicted  $[C/H]$  distribution, except that the same simulation does not reproduce absorbers with  $[C/H] \geq -0.5$  at  $\log N_{\text{CIV}} \in [12, 14]$ . A similar discrepancy is also seen in Figs. 1 and 3 by Shen et al. (2013). Considering that the line-of-sight length of C III absorbers with  $[C/H]_{\text{temp}} \geq -0.5$  is less than 1 kpc (Fig. 19), the discrepancy may be due to an insufficient resolution to resolve these absorbers in simulations.

#### 5.4 Total hydrogen volume density, total hydrogen column density and $N_{\text{HI}}$

Correlations between the observed HI column density, the total hydrogen volume density and the total hydrogen column density are presented in the upper panels of Fig. 23. In the upper left panel, the dashed line shows the  $N_{\text{HI}}-n_{\text{H}}$  relation derived by Schaye et al. (2000) for a self-gravitating, photoionised HI gas in local hydrostatic equilibrium. The Schaye  $N_{\text{HI}}-n_{\text{H}}$  relation requires the HI photoionisation rate, the gas temperature and the gas mass fraction. We used the HI photoionisation rate  $\Gamma = 9.575 \times 10^{-13} \text{ sec}^{-1}$  for our fiducial HM Q+G 2012 UVB at  $z = 2.4$ . The gas temperature was calculated using Cloudy as a function of

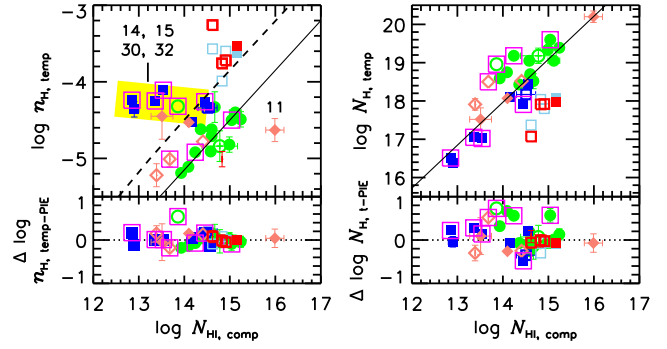


**Figure 23.** *Upper panels:* the total hydrogen density  $n_{\text{H,temp}}$  as a function of  $N_{\text{HI}}$  (left panel) and the total hydrogen column density ( $N_{\text{HI}} + N_{\text{HII}}$ ) as a function of  $N_{\text{HI}}$  (right panel), respectively. All the symbols are the same as in Fig. 21. In the left panel, the dashed line indicates the Schaye  $N_{\text{HI}}-n_{\text{H}}$  relation at  $z = 2.4$ ,  $n_{\text{H,temp}} = -13.65 + 0.65 \times N_{\text{HI}}$ , while the solid line is the Schaye relation shifted down by 0.6 dex to match low-metallicity branch absorbers noted as green symbols. The yellow-shaded region indicates a fit to the high-metallicity branch absorbers when 4 absorbers with  $\log n_{\text{H}} \geq -4$  (C II-enriched absorbers) are excluded,  $\log n_{\text{H,temp}} = -3.49 - 0.06 \times \log N_{\text{HI}}$ . In the right panel, the solid line shows the least-square fit:  $\log N_{\text{H,temp}} = 2.25 + 1.12 \times \log N_{\text{HI}}$ . *Lower panels:* the difference between the non-PIE  $T_b$  and PIE models for the HM Q+G 2012 UVB. Refer to the online version for clarity.

$N_{\text{HI}}$  for the HM Q+G 2012 at  $z = 2.4$ , while the gas mass fraction was used as his default value.

Unlike the theoretical prediction, the observed and predicted parameters indicate no well-defined relation between  $n_{\text{H,temp}}$  and  $N_{\text{HI}}$  for the full sample. This departure from the Schaye relation is not due to the fact that the observed data cover an extended redshift range  $2.1 < z < 3.4$ , while the calculated Schaye relation is at  $z = 2.4$ , since input parameters do not change significantly at  $2.1 < z < 3.4$ . Nor is it due to the imposed non-PIE condition, since the difference between the non-PIE and PIE models is negligible.

If the 4 C II-enriched absorbers at  $\log n_{\text{H}} \geq -4$  are excluded, the  $N_{\text{HI}}-n_{\text{H}}$  plane is reminiscent of the  $N_{\text{CIV}}-[C/H]_{\text{temp}}$  plane in Fig. 18. The total hydrogen density  $n_{\text{H}}$  of low-metallicity branch absorbers (green symbols) increases with  $N_{\text{HI}}$ , while  $n_{\text{H}}$  of high-metallicity branch absorbers in the yellow-shaded region is almost independent of  $N_{\text{HI}}$ . Interestingly, if the Schaye relation is shifted down by 0.6 dex, it matches low-metallicity branch absorbers. The shift in the normalisation from the Schaye equation can be caused by many factors, such as an incorrect temperature dependence. For example, the metal cooling in the gas could change the internal ionisation and thermal structure, while the Schaye relation does not account for any metals associated with the forest.

A group of absorbers at  $(\log N_{\text{HI}}, \log n_{\text{H,temp}}) \sim (13.2, -4.3)$ , marked with an absorber number, is simple high-metallicity branch absorbers characterised by a higher  $N_{\text{CIV}}$  rather than typical HI with a similar  $N_{\text{HI}}$ . If these absorbers are excluded, high-metallicity branch absorbers including 4 C II absorbers in red roughly follow the Schaye relation. In fact, C III absorbers can be viewed to be confined by the dashed (the Schaye relation) and solid lines on

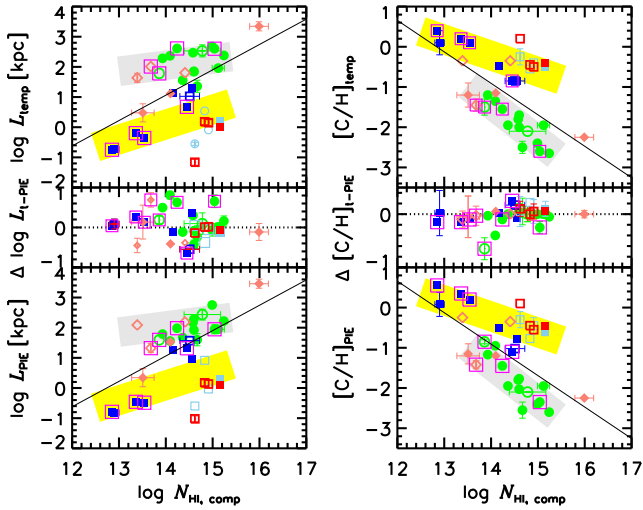


**Figure 24.** *Upper left panel:* the line-of-sight length  $L_{\text{temp}}$  as a function of  $N_{\text{H I}}$ . All the symbols are the same as in Fig. 23. The solid line, yellow-shaded and gray-shaded regions are the least-square fit to the full sample, high-metallicity branch and low-metallicity branch absorbers, respectively. *Upper right panel:*  $[\text{C}/\text{H}]_{\text{temp}}$  as a function of  $N_{\text{H I}}$ . *Middle panels:* the difference between the non-PIE  $T_{\text{b}}$  and PIE models for the HM Q+G 2012 UVB. *Lower panels:* for the PIE model. The yellow-shaded and gray-shaded regions are the same ones as in the upper panels. Refer to the online version for clarity.

the  $\log N_{\text{H I}} - \log n_{\text{H, temp}}$  plane. This suggests that overall the basic assumptions of the Schaye relation are not far-fetched despite being too simplistic and that the individual absorber differs from each other, having an intrinsic scatter in the gas temperature, the gas density and the metallicity even at the same overdensity.

A non-PIE condition introduces a large scatter on the  $N_{\text{H I}} - N_{\text{H, temp}}$  plane in the upper right panel, although a general trend exists. A large scatter at  $\log N_{\text{H I}} \sim 14.5$  is due to the large scatter in  $n_{\text{H}}$  for the same  $N_{\text{H I}}$  range. Due to a higher  $n_{\text{H, temp}}$ , the 4 C II-enriched absorbers have a lower  $N_{\text{H}}$  compared to C II-free absorbers with a similar  $N_{\text{H I}}$ . Again, there is a suggestion that high-metallicity and low-metallicity branch absorbers follow a different scaling relation. The difference between the non-PIE and PIE models is  $\langle \Delta \log N_{\text{H}} \rangle = 0.07 \pm 0.30$ , implying that on average there is no significant systematic difference in  $N_{\text{H}}$  between PIE and non-PIE models.

### 5.5 Carbon abundance, line-of-sight length and $N_{\text{H I}}$

In Subsection 5.1, we suggested that C III absorbers consist of 2 distinct populations based on the  $N_{\text{C IV}} - [\text{C}/\text{H}]_{\text{temp}}$  and  $N_{\text{C IV}} - L_{\text{temp}}$  relations. In Subsections 5.2–5.4, these two populations are shown to follow their own scaling relations between various observed and predicted physical parameters. In this Subsection, we present similar relations to those explored in Subsection 5.1, but here for  $N_{\text{H I}}$  instead of  $N_{\text{C IV}}$ .

In Fig. 24, the entire  $N_{\text{H I}} - L_{\text{temp}}$  plane can be viewed as a scatter plot, with a spread of 2–3 dex in  $L_{\text{temp}}$  for a given  $N_{\text{H I}}$ . However, only a few data points are clustered

around a least-square fit to the full sample, shown as a solid line. Indeed, except at  $\log N_{\text{H I}} \sim 14.5$ , no C III absorbers are along the  $\log L_{\text{temp}} \sim 1.4$  line at other  $N_{\text{H I}}$ , implying that the  $N_{\text{H I}} - L_{\text{temp}}$  plane is also interpreted better in terms of two populations. For both branch absorbers,  $L_{\text{temp}}$  increases as  $N_{\text{H I}}$  increases, but with a different scaling relation as tabulated in Table 3. The non-PIE nature disperses low-metallicity branch absorbers in to a wider  $L_{\text{temp}}$  range.

Similarly, tied C III absorbers on the  $N_{\text{H I}} - [\text{C}/\text{H}]_{\text{temp}}$  plane tend to lie distinctly above or below the least-square fit line rather than on it, with a division at  $[\text{C}/\text{H}]_{\text{temp}} \sim -1.0$ . For both branch absorbers,  $[\text{C}/\text{H}]_{\text{temp}}$  decreases as  $N_{\text{H I}}$  increases. Table 4 lists the scaling relation for each population. Note that low-metallicity branch absorbers show an anti-correlation between  $N_{\text{H I}}$  and  $[\text{C}/\text{H}]_{\text{temp}}$ , an opposite trend from the  $N_{\text{C IV}} - [\text{C}/\text{H}]_{\text{temp}}$  relation. Since only a few absorbers have a large difference from the PIE model shown in the middle right panel, the non-PIE nature does not alter the relation.

## 6 THE ORIGIN OF THE BIMODALITY OF C III ABSORBERS

### 6.1 Implication from the equivalent width and impact parameter relation

Numerical simulations predict that the *projected*  $N_{\text{H I}}$  around galaxies (the total  $N_{\text{H I}}$  integrated along a sightline long enough to contain galaxies and their surrounding in a simulation box) decreases with a galactocentric distance in a well-defined way, depending on the galaxy potential (Cen & Chisari 2011; Shen et al. 2013; Shull 2014). There is a large scatter, but the observed H I rest-frame equivalent width (REW – used as a proxy for the H I column density) roughly decreases with the galaxy impact parameter both at low redshifts (Chen et al. 2001; Wakker & Savage 2009; Liang & Chen 2014) and at high redshifts (Steidel et al. 2010). The observed C IV REW also decreases with the impact parameters, but much more steeply so that C IV reaches to its detection limit at a smaller impact parameter than H I (Chen et al. 2001; Steidel et al. 2010; Liang & Chen 2014).

A large scatter in the relation is reduced when the impact parameter is normalised with the galaxy luminosity (Chen et al. 2001) or the virial radius (Stocke et al. 2013; Liang & Chen 2014; Shull 2014). Since the H I distribution around galaxies is influenced by the galaxy potential, the projected  $N_{\text{H I}}$  is a better physical parameter than a geometrical impact parameter, i.e. at the same impact parameter, a more massive galaxy has a larger REW. In short, the projected (or integrated)  $N_{\text{H I}}$  is a normalised impact parameter by the galaxy potential, as long as H I gas is not significantly disturbed kinematically, such as nearby supernova explosions. Compared to the impact parameter normalised by a virial radius, the integrated  $N_{\text{H I}}$  is a simple and straightforward parameter, since 1) obtaining an impact parameter requires a time-intensive deep galaxy survey around target QSOs, 2) the galaxy survey is flux-limited, biasing toward brighter galaxies especially at high redshifts and 3) assigning a single galaxy to a single absorber is not unambiguous due to the galaxy clustering or no nearby galaxies above a detection limit (Wakker & Savage 2009; Steidel et al. 2010; Liang & Chen 2014; Savage et al. 2014).

Simulations also predict that the projected gas metallicity (the metal mass density divided by the total mass density) distribution around a star-forming galaxy is bipolar, since metals are transported to galactic halo and the surrounding IGM by galactic outflows which tend to propagate along the minor axis where the ISM density is low. The higher-metallicity gas at  $[Z/H] \geq -0.5$  is close to the minor axis, while the gas at  $[Z/H] \in [-2.5, -1.0]$  is far from the galaxy along the minor axis (i.e. has a larger impact parameter) or is more uniformly distributed along the major axis from a small to large impact parameter beyond the virial radius, cf. Fig. 1 of Shen et al. (2013). For an optically-thin gas at  $\log T \sim 3.9\text{--}5.1$  exposed to the HM Q+G 2012 UVB, the dominant ions of carbon is C III and C IV. Therefore, the projected  $N_{\text{C IV}}$  is roughly proportional to  $[C/H]_{\text{temp}}$ , and the distribution of observed  $N_{\text{C IV}}$  is expected to follow the  $[Z/H]$  distribution predicted by simulations.

## 6.2 Origin of high-metallicity branch absorbers

Based on the observational and theoretical results in Subsection 6.1, including an observational suggestion of bimodal metallicity distribution of Mg II absorbers at  $z < 1$  (Bouché et al. 2012; Lehner et al. 2013), it is not unreasonable that C III absorbers could consist of two populations.

For high-metallicity absorbers, their predicted line-of-sight length increases with observed  $N_{\text{C IV}}$  and  $N_{\text{H I}}$  up to  $\sim 20$  kpc, roughly a size of an extended optical disk or inner halo (Brooks et al. 2011). The positive correlation between the line-of-sight length and the observed column density is reminiscent of high ions, such as C IV, N V and O VI, in the Milky Way, where the column density of high ions increases with the distance to the background hot star in the Milky Way disk (Jenkins 1978; Lehner et al. 2011). This has been interpreted to imply that the number of intervening, randomly distributed, distinct high-ion gas clouds in the Milky Way increases as the distance to the star increases.

Our 12 high-metallicity branch absorbers can be further classified into two subclasses. About 67% (8 out of 12) of high-metallicity branch absorbers are part of a multi-component C IV complex, having several, nearby C IV clumps within  $\sim 200 \text{ km s}^{-1}$ . Therefore, it is not implausible that a seemingly single C IV component is in fact a composite of several smaller gas clouds in extended disks, inner halos or outflowing gas and our  $6.7 \text{ km s}^{-1}$  spectral resolution is not sufficient enough to resolve them. All of them are associated with Si IV, indicative of higher density and higher metallicity, thus closer to galaxies compared to Si IV-free C IV absorbers (Shen et al. 2013).

Simple high-metallicity branch absorbers (the absorber number #14, 15, 30 and 32) are associated with strong C IV and weak H I. They have  $L_{\text{temp}} \leq 1$  kpc and super-solar metallicity. Outliers in several well-characterised correlations presented in Section 5 mostly belong to this subclass. This subclass was studied extensively by Schaye et al. (2007), which characterises this subclass as having a super-solar metallicity, a size of about 100 pc and a life time of  $\sim 6 \times 10^6$  years, i.e. they are not self-gravitating. Schaye et al. (2007) conclude that these absorbers are caught in the process of transporting metals into the IGM. Since there are only 4 absorbers at  $L_{\text{temp}} \leq 0.35$  kpc in this subclass and since they are usually outliers, it is not clear whether sim-

ple high-metallicity branch absorbers are also unresolved multi-component gas clouds in extended disks/inner halos like complex high-metallicity branch absorbers.

From Figs 18 and 24, the carbon abundance of high-metallicity branch absorbers is anti-correlated with  $N_{\text{C IV}}$  and  $N_{\text{H I}}$  with

$$[C/H]_{\text{temp}} \propto -1.04 \times \log N_{\text{C IV}}, \quad (2)$$

and

$$[C/H]_{\text{temp}} \propto -0.40 \times \log N_{\text{H I}}. \quad (3)$$

This implies that  $N_{\text{C IV}}$  and  $N_{\text{H I}}$  of high-metallicity branch absorbers cannot be used as a proxy of impact parameter, which seems to conflict with simulations and observations as discussed above.

This apparent discrepancy is mainly caused by the fact that  $N_{\text{C IV}}$  and  $N_{\text{H I}}$  plotted in Figs 18 and 24 are for an individual *component*. On the other hand, simulations use the projected total column density of H I or C IV, not an individual component, as well as the averaged gas metallicity along the sightline. To be a fair comparison,  $N_{\text{C IV}}$  and  $N_{\text{H I}}$  in Figs. 18 and 24 should be summed up all the components within a given velocity range appropriate for intervening galaxies and  $[C/H]_{\text{temp}}$  should be an average of these individual components. Unfortunately, due to the kinematically complicated component structure of complex high-metallicity absorbers, there is no one-to-one correspondence between H I and C IV components, and it is not possible to derive  $[C/H]_{\text{temp}}$  of all the individual C IV components.

The anti-correlation between  $[C/H]_{\text{temp}}$  and column density can be better understood, when combined with the  $[C/H]_{\text{temp}}\text{--}L_{\text{temp}}$  anti-correlation. Since there is a slight difference between H I and C IV distributions due to non-uniform  $n_{\text{H}}$ , peculiar velocity, UVB and metallicity (Cen & Chisari 2011), the  $L_{\text{temp}}$  dependence on the column density of H I and C IV is expected to be different. From Figs. 18 and 24, for high-metallicity branch absorbers,

$$[C/H]_{\text{temp}} \propto 0.56 \times \log \left( \frac{N_{\text{C IV}}}{N_{\text{H I}}} \right), \quad (4)$$

$$N_{\text{C IV}} \propto L_{\text{temp}}^{0.46}, \quad (5)$$

$$N_{\text{H I}} \propto L_{\text{temp}}^{2.00}, \quad (6)$$

which leads to

$$[C/H]_{\text{temp}} \propto -0.86 \times \log L_{\text{temp}}. \quad (7)$$

This is the anti-correlation between  $[C/H]_{\text{temp}}$  and  $L_{\text{temp}}$  displayed in Fig. 19, caused by the fact that a higher amount of  $N_{\text{H I}}$  is added up along the same line-of-sight than  $N_{\text{C IV}}$ . Due to a higher  $N_{\text{H I}}$  than  $N_{\text{C IV}}$  for a larger- $L_{\text{temp}}$  absorber, even if it is a unresolved component,  $[C/H]_{\text{temp}}$  decreases with  $L_{\text{temp}}$ .

Combined with an anti-correlation between  $L_{\text{temp}}$  and  $[C/H]_{\text{temp}}$ , the anti-correlation between  $[C/H]_{\text{temp}}$  and  $N_{\text{C IV}}$  or  $N_{\text{H I}}$  suggests that  $[C/H]_{\text{temp}}$  decreases when a C IV-enriched gas is dispersed in to a larger distance or expands to be mixed with an adjacent low-metallicity ISM/halo gas.

## 6.3 Origin of low-metallicity branch absorbers

For low-metallicity branch absorbers, the median  $L_{\text{temp}}$  is  $\sim 233$  kpc, ranged from 20 to 480 kpc. In addition to

$[C/H]_{\text{temp}} \leq -1$  and the total hydrogen density at  $n_{\text{H,temp}} \in [-5.2, -4.3]$ , close to the cosmic mean density, the line-of-sight length argument is in favour of their origin as a galactic halo and the surrounding IGM filaments.

Their  $[C/H]_{\text{temp}}$  is  $\propto 1.13 \times \log N_{\text{CIV}}$  and  $\propto -0.91 \times \log N_{\text{HI}}$ . This reflects that  $N_{\text{CIV}}/N_{\text{HI}}$  (a proxy for  $[C/H]_{\text{temp}}$ ) decreases with  $N_{\text{HI}}$ , as  $N_{\text{CIV}}$  is almost independent of  $N_{\text{HI}}$  with a large scatter (Fig. 9). Being almost independent of  $L_{\text{temp}}$  on  $N_{\text{HI}}$  and  $N_{\text{CIV}}$ , the opposite trend of  $[C/H]_{\text{temp}}$  on  $N_{\text{CIV}}$  and  $N_{\text{HI}}$  implies that 1) C IV (and hence C III) is not likely to be homogeneously mixed with H I at the scale of  $\sim 200$  kpc or 2) an expansion of C IV gas into the ambient medium with time increases a line-of-sight length for some gas clouds with a similar  $N_{\text{CIV}}$ .

## 7 SUMMARY

We have analysed the physical properties of 53 intervening, optically-thin C IV+C III systems at  $2.1 < z < 3.4$  in the 19 high-quality optical spectra taken with the UVES at the VLT and HIRES at Keck with  $\sim 6.7 \text{ km s}^{-1}$  resolution. The selected systems have the same velocity structure in both C IV and C III (also C II  $\lambda\lambda 1334, 1036$  if detected), and were fitted with Voigt profiles with the same fixed redshift and line widths (or  $b$  parameters) for each corresponding component when the velocity centroid difference between untied C IV and C III is less than  $1.5 \text{ km s}^{-1}$ . When a clean, separable H I component for each corresponding C IV exists within  $15 \text{ km s}^{-1}$ , the H I component was fitted with the same redshift and appropriate line width to build a sample of tied (aligned) H I+C IV+C III component trios, i.e. kinematically simple absorbers.

The 53 C III systems consists of 155 C IV components. Out of 155, 132 C IV components are associated with the tied C III (104 clean detections, 4 lower limits and 24 upper limits) and 23 C IV components have either blended C III regions or shifted C III. 54 C IV components (35%, 54/155) have the tied H I, while 33 components (21%, 33/155) have both tied H I and C III with well-measured C III column densities.

For the 132 tied C IV+C III components at  $\log N_{\text{CIV}} \in [11.7, 14.1]$  and  $\log N_{\text{CIII}} \in [11.5, 14.0]$  for clean C III:

(i)  $N_{\text{CIII}} \propto N_{\text{CIV}}^{1.42 \pm 0.11}$ , with lower (higher)  $N_{\text{CIII}}$  at  $\log N_{\text{CIV}} \leq 13$  ( $\geq 13$ ). There is a suggestion of the breakdown of this linear relation at higher- $N_{\text{CIV}}$  ends. The mean ratio of  $N_{\text{CIII}}$  and  $N_{\text{CIV}}$  is  $\langle N_{\text{CIII}}/N_{\text{CIV}} \rangle = 1.0 \pm 0.3$ , with a negligible redshift evolution.

(ii) For the C IV+C III components with a tied H I, no systematic trend is found in  $N_{\text{CIII}}/N_{\text{CIV}}$  as a function of  $N_{\text{HI}}$ , implying that both  $N_{\text{CIII}}$  and  $N_{\text{CIV}}$  behave in a similar way to  $N_{\text{HI}}$ .

From the 54 tied H I+C IV component pairs at  $\log N_{\text{HI}} \in [12.2, 16.0]$  and  $\log N_{\text{CIV}} \in [11.8, 13.8]$ :

(i) The tied C IV components cover the wide range of column densities and  $b$  parameters in the  $N_{\text{CIV}} - b_{\text{CIV}}$  plane. On the other hand, most tied H I components are located along the cutoff- $b$  line on the  $N_{\text{HI}} - b_{\text{HI}}$  plane. This suggests that the tied pairs only sample an gas having a specific physical condition, not a representative of the entire low- $N_{\text{HI}}$  absorber.

(ii) The temperature  $T_b$  estimated from the line widths of H I and C IV is well-approximated to a Gaussian peaking at  $\log T_b \sim 4.4 \pm 0.3$  at a range of  $\log T_b \sim 3.5 - 5.5$ , implying that the tied H I+C IV pairs sample both photoionised and collisionally ionised C IV. Excluding 4 pairs non-thermally broadened, the mean and median gas temperatures are  $\langle \log T \rangle = 4.52 \pm 0.33$  and  $\log T_{\text{median}} = 4.48$ .

(iii) The median non-thermal line width and thermal line width are  $b_{\text{nt,median}} = 7$  and  $b_{\text{th,median}} = 22 \text{ km s}^{-1}$ . About 59% (32 out of 54) of the pairs has the non-thermal energy contribution to the total energy less than 10%, meaning that the majority of the pairs near the cutoff- $b_{\text{HI}}$  are thermally broadened.

Including 4 C II-enriched C III absorbers, but excluding one non-thermal absorber, 32 C III absorbers have tied H I, C IV and C III, with  $\log N_{\text{HI}} \in [12.9, 16.0]$ ,  $\log N_{\text{CIV}} \in [11.8, 13.8]$ ,  $\log N_{\text{CIII}} \in [11.7, 13.8]$  and  $\log N_{\text{CII}} \in [12.2, 12.7]$ , respectively. We have built the Cloudy photoionisation models for three theoretical UV background radiation models, the Haardt-Madau (HM) 2005 UV background contributed both by QSOs and galaxies (Q+G) and only by QSOs (Q) as well as our fiducial HM Q+G 2012 model. As the Cloudy-predicted gas temperature for a photoionisation equilibrium (PIE) gas is different from the gas temperature  $T_b$ , the non-PIE Cloudy model with the fixed temperature  $T_b$  was also built for the HM Q+G 2012, which is our fiducial model to derive the physical parameters of 32 tied C III absorbers, subscripted with “temp”.

(i) About 25% of the absorbers has more than 50% difference between  $T_b$  and  $T_{\text{PIE}}$ , with a higher  $T_b$  for all the highly discrepant absorbers but one. This implies that the PIE assumption is not likely to hold in these absorbers, probably due to recent cooling from a hotter gas or additional radiation. There is a suggestion that more absorbers show a larger temperature difference at lower redshifts and at  $\log N_{\text{HI}} \leq 14$ .

(ii) The Cloudy-predicted parameters do not show a strong discrepancy between the non-PIE  $T_b$  and the PIE models for the same UVBs. However, the non-PIE condition increases a scatter in any PIE correlations.

(iii) There is evidence of two populations of kinematically simple, optically-thin C III absorbers, occupied in a distinct region on the various parameter spaces with their own scaling relation. High-metallicity (low-metallicity) branch absorbers have the carbon abundance  $[C/H]_{\text{temp}} \geq -1.0$  ( $\leq -1.0$ ) and a line-of-sight length  $L_{\text{temp}} \leq 20 \text{ kpc}$  ( $\geq 20 \text{ kpc}$ ).

(iv) High-metallicity branch absorbers are either complex with multi-component C IV mostly associated with Si IV, or simple, sometimes having super-solar metallicity, which are characterised by stronger C IV than the usual H I absorbers with a similar  $N_{\text{HI}}$ . Considering their higher  $T_b$  than  $T_{\text{PIE}}$  and higher  $[C/H]_{\text{temp}}$ , simple high-metallicity branch absorbers are likely to be radiatively cooling gas from a higher temperature and/or to be expanding. Outliers from any well-characterised correlations are mostly simple high-metallicity branch absorbers or 4 absorbers associated with C II.

(v) High-metallicity branch absorbers have a lower gas temperature than low-metallicity branch absorbers having  $\log T_b \sim 4.5$ , due to an increased cooling rate by a higher  $[C/H]_{\text{temp}}$ . The total (neutral and ionised) hydrogen volume density is  $\log n_{\text{H,temp}} \in [-4.5, -3.3]$ , about an order

of magnitude higher than low-metallicity branch absorbers. Compared to the warm ionised gas in the Milky Way with a comparable temperature range, high-metallicity absorbers have two orders of magnitude lower  $n_{\text{H, temp}}$ .

(vi) For high-metallicity branch absorbers,  $L_{\text{temp}} \propto N_{\text{C IV}}^{2.17}$  and  $L_{\text{temp}} \propto N_{\text{H I}}^{0.50}$  upto  $L_{\text{temp}} \leq 20$  kpc, roughly a size of intervening disks or inner halos. This trend is similar to what is observed for high ions in the Milky Way. The observations imply that 1) a seemingly single-component profile of C IV and H I is in fact an ensemble average of many components unresolved in our spectra and 2) a larger line-of-sight length passes through more numbers of randomly distributed H I and C IV gas clouds in extended disks or outflowing gas in inner halos.

(vii) For high-metallicity branch absorbers,  $[\text{C}/\text{H}]_{\text{temp}}$  is anti-correlated as  $\propto -1.04 \times \log N_{\text{C IV}}$  and  $\propto -0.40 \times \log N_{\text{H I}}$ , implying that the total  $N_{\text{H I}}$  integrated along the same sightline is larger than the total  $N_{\text{C IV}}$ . Since the relative fraction between C III and C IV for optically-thin gas exposed to the HM Q+G 2012 UVB is similar as a function of  $N_{\text{H I}}$ , a larger  $N_{\text{H I}}$  decreases  $[\text{C}/\text{H}]_{\text{temp}}$ .

(viii) Low-metallicity branch absorbers do not have associated Si IV and have  $\log n_{\text{H, temp}} \in [-5.3, -4.2]$ . This corresponds to a cosmic over-density of 0.3–13, which is for a typical low-density intergalactic H I gas, not in a collapsed object. Their gas temperature is close to the PIE equilibrium temperature at  $\log T_b \sim 4.5$  at the low-metallicity regime, except a few outliers with a higher  $T_b$ , probably due to recent cooling.

(ix) For low-metallicity branch absorbers,  $L_{\text{temp}} \propto N_{\text{C IV}}^{0.55}$  and  $L_{\text{temp}} \propto N_{\text{H I}}^{0.20}$  at  $L_{\text{temp}} \in [20, 480]$  kpc, roughly a size of intervening halos or the surrounding IGM filaments.

(x) For low-metallicity branch absorbers,  $[\text{C}/\text{H}]_{\text{temp}} \propto 1.13 \times \log N_{\text{C IV}}$  and  $\propto -0.91 \times \log N_{\text{H I}}$ . This reflects that  $N_{\text{C IV}}/N_{\text{H I}}$  (a proxy for  $[\text{C}/\text{H}]_{\text{temp}}$ ) decreases with  $N_{\text{H I}}$ , as  $N_{\text{C IV}}$  is almost independent of  $N_{\text{H I}}$  with a large scatter. The opposite trend of  $[\text{C}/\text{H}]_{\text{temp}}$  on  $N_{\text{C IV}}$  and  $N_{\text{H I}}$  implies that 1) C IV and C III are not likely to be homogeneously mixed with H I at the scale of  $\sim 200$  kpc or 2) an expansion of C IV gas into the ambient medium with time increases a line-of-sight length for some gas clouds with a similar  $N_{\text{C IV}}$ .

(xi) At  $2.1 < z < 2.6$ ,  $[\text{C}/\text{H}]_{\text{temp}}$  spans a wide range from  $-2.7$  to  $0.4$ , with the mean value of  $-1.0 \pm 1.0$ . Its distribution has a long Gaussian tail at low carbon abundance. On the other hand, at  $2.6 < z < 3.4$ , C III absorbers have a smaller range of  $[\text{C}/\text{H}]_{\text{temp}}$  at  $-2.1$  to  $-0.9$ , with the mean value of  $-1.6 \pm 0.4$ . There is a lack of data points at  $[\text{C}/\text{H}]_{\text{temp}} \geq -0.8$ , which is not an observational bias as these absorbers are easy to detect.

(xii) The total hydrogen density  $n_{\text{H, temp}}$  does not follow the theoretical  $N_{\text{H I}}-n_{\text{H}}$  relation by Schaye (2001) for a self-gravitating, metal-free PIE gas in local hydrostatic equilibrium, since our C III absorbers sample a gas in a wide range of physical conditions. However, when excluded simple high-metallicity branch absorbers, the remaining high-metallicity branch absorbers satisfy the Schaye relation. Low-metallicity branch absorbers follows the Schaye relation if shifted down by 0.6 dex.

(xiii) The evidence for bimodal distributions in the observed and derived physical parameters for optically-thin C III absorbers is largely independent of the choice of UVB,

as long as all the C III absorbers are exposed to a similar UVB.

## ACKNOWLEDGMENTS

TSK appreciates an insightful discussion with B. D. Savage. TSK acknowledges funding support to the European Research Council Starting Grant ‘‘Cosmology with the IGM’’ through grant GA-257670. RFC is also supported by the same grant for his stay at Osservatorio Astronomico di Trieste to carry out part of this work. TSK is also grateful to a travel support by the FP7 ERC Advanced Grant Emergence-320596 to IoA, Cambridge, where part of this work was done. DR was partially supported by the National Science Foundation’s Research Experience for Undergraduates program through NSF Award AST-1004881 to the University of Wisconsin-Madison.

## REFERENCES

- Agafonova I. I., Levshakov S. A., Reimers D., Fechner C., Tytler D., Simcoe R. A., Songaila A., 2007, *A&A*, 461, 893
- Aguirre A., Hernquist L., Schaye J., Weinberg D. H., Katz N., Gardner J., 2001, *ApJ*, 560, 599
- Barai P., Viel M., Borgani S., Tescari E., Tornatore L., Dolag K., Killedear M., Monaco P., D’Odorico V., Cristiani S., 2013, *MNRAS*, 430, 3213
- Barger K. A., Haffner L. M., Bland-Hawthorn J., 2013, *ApJ*, 771, 132
- Bergeron J., 1986, *A&A*, 155, L8
- Bergeron J., Stasińska G., 1986, *A&A*, 169, 1
- Boksenberg A., Sargent W. L. W., 2015, *ApJ*, *in press*, astro-ph:
- Bolton J. S., Becker G. D., Haehnelt M. G., Viel M., 2014, *MNRAS*, 438, 2499
- Bolton J. S., Haehnelt M. G., Viel M., Springel V., 2005, *MNRAS*, 357, 1178
- Bolton J. S., Viel M., 2011, *MNRAS*, 414, 241
- Bordoloi R., Tumlinson J., Werk J. K., Oppenheimer B. D., Peebles M. S., Prochaska J. X., Tripp T. M., Katz N., Davé R., Fox A. J. e. a., 2014, *ApJ*, 796, 136
- Bouché N., Hohensee W., Vargas R., Kacprzak G. G., Martin C. L., Cooke J., Churchill C. W., 2012, *MNRAS*, 426, 801
- Brooks A. M., Solomon A. R., Governato F., McCleary J., MacArthur L. A., Brook C. B. A., Jonsson P., Quinn T. R., Wadsley J., 2011, *ApJ*, 728, 51
- Bullock J. S., Kolatt T. S., Sigad Y., Somerville R. S., Kravtsov A. V., Klypin A. A., Primack J. R., Dekel A., 2001, *MNRAS*, 321, 559
- Carswell R. F., Becker G. D., Jorgenson R. A., Murphy M. T., Wolfe A. M., 2012, *MNRAS*, 422, 1700
- Carswell R. F., Webb J. K., 2014, VPFIT, Astrophysics Source Code Library, record ascl:1408.015
- Cen R., Chisari N. E., 2011, *ApJ*, 731, 11
- Cen R., Miralda-Escudé J., Ostriker J. P., Rauch M., 1994, *ApJL*, 437, L9
- Chen H.-W., Lanzetta K. M., Webb J. K., 2001, *ApJ*, 556, 158

- Chen H.-W., Lanzetta K. M., Webb J. K., Barcons X., 2001, *ApJ*, 559, 654
- Cowie L. L., Songaila A., Kim T., Hu E. M., 1995, *AJ*, 109, 1522
- Davé R., Hernquist L., Katz N., Weinberg D. H., 1999, *ApJ*, 511, 521
- Davé R., Oppenheimer B. D., Katz N., Kollmeier J. A., Weinberg D. H., 2010, *MNRAS*, 408, 2051
- Dutta R., Srianand R., Rahmani H., Petitjean P., Noterdaeme P., Ledoux C., 2014, *MNRAS*, 440, 307
- Ellison S. L., Songaila A., Schaye J., Pettini M., 2000, *ApJL*, 120, 1175
- Faucher-Giguère C., Lidz A., Hernquist L., Zaldarriaga M., 2008, *ApJ*, 688, 85
- Ferland G. J., Porter R. L., van Hoof P. A. M., Williams R. J. R., Abel N. P., Lykins M. L., Shaw G., Henney W. J., Stancil P., 2013, *Rev. Mexicana de Astronomia y Astrofisica*, 49, 137
- Fynbo J. P. U., Laursen P., Ledoux C., Møller P., Durgapal A. K., Goldoni P., Gullger B., Kaper L., Maund J., Noterdaeme P., Östlin G., Strander M. L., Toft S., Vreeswijk P. M., Zafar T., 2010, *MNRAS*, 408, 2128
- Gnat O., Sternberg A., 2007, *ApJS*, 168, 213
- Haardt F., Madau P., 2012, *ApJ*, 746, 125
- Haehnelt M. G. C., Rauch M., Steinmetz M., 1996, *MNRAS*, 283, 1055
- Haffner L.-M., Dettmar R. J., Beckman J. E., Wood K., Slavin J. D., Giammanco C., Madsen G. J., Zurita A., Reynolds R. J., 2009, *RvMP*, 81, 969
- Hellsten U., Davé R., Hernquist L., Weinberg D. H., Katz N., 1997, *ApJ*, 487, 482
- Hu E. M., Kim T., Cowie L. L., Songaila A., Rauch M., 1995, *AJ*, 110, 1526
- Jenkins E. B., 1978, *ApJ*, 220, 107
- Jorgenson R. A., Murphy M. T., Thompson R., Carswell R. F., 2014, *MNRAS*, 443, 2783
- Keres D., Katz N., Weinberg D. H., Davé R., 2005, *MNRAS*, 363, 2
- Kim T.-S., Carswell R. F., Partl A. M., 2015, *MNRAS*, *submitted*
- Kim T.-S., Cristiani S., D’Odorico S., 2001, *A&A*, 373, 757
- Kim T.-S., Partl A. J., Carswell R. F., Müller V., 2013, *A&A*, 731, 6
- Kirkman D., Tytler D., 1997, *ApJ*, 484, 672
- Kollmeier J. A., Weinberg D. H., Oppenheimer B. D., Haardt F., Katz N., Davé R., Fardal M. e., 2014, *ApJ*, 789, L32
- Lanzetta J.-M., Bowen D., 1990, *ApJ*, 357, 321
- Lanzetta K.-M., Bowen D. V., Tytler D., Webb J. K., 1995, *ApJ*, 442, 538
- Le Brun V., Bergeron J., Boisse P., Deharveng J. M., 1997, *A&A*, 321, 733
- Lehner N., Howk J. C., Tripp T. M., Tumlinson J., Prochaska J. X., O’Meara J. M., Thom C., Werk J. K., Fox A. J., Ribaud J., 2013, *ApJ*, 770, 138
- Lehner N. D., Zech W. F., Howk J. C., Savage B. D., 2011, *ApJ*, 727, 46
- Liang C. J., Chen H.-W., 2014, *MNRAS*, 445, 2061
- Martin C. L., 2005, *ApJ*, 621, 227
- Muzahid S., Srianand R., Bergeron J., Petitjean P., 2012, *MNRAS*, 421, 446
- Navarro J. F., Frenk C. S., White S. D. M., 1996, *ApJ*, 462, 563
- Oppenheimer B. D., Davé R., 2009, *MNRAS*, 395, 1875
- Oppenheimer B. D., Davé R., Katz N., Kollmeier J. A., Weinberg D. H., 2012, *MNRAS*, 420, 829
- Oppenheimer B. D., Schaye J., 2013, *MNRAS*, 434, 1043
- Osterbrock D. E., 1974, *Astrophysics of Gaseous Nebulae*
- Rauch M., Haehnelt M. G., Steinmetz M., 1997, *ApJ*, 481, 601
- Rauch M., Sargent W. L. W., Womble D. S., Barlow T. A., 1996, *ApJ*, 467, L5
- Reimers D., Köhler S., Wisotzki L., Groote D., Rodriguez-Pascual P., Wamsteker W., 1997, *A&A*, 327, 890
- Ricotti M., Gnedin N. Y., Shull J. M., 2000, *ApJ*, 534, 41
- Rudie G. C., Steidel C. C., Pettini M., 2012, *ApJ*, 757, 30
- Rudie G. C., Steidel C. C., Shapley A. E., Pettini M., 2013, *ApJ*, 769, 146
- Rupke D. S. N., Veilleux S., 2013, *ApJ*, 768, 75
- Savage B. D., Kim T. S., Wakker B. P., Keeney B. A., Shull J. M., Stocke J. T., Green J. C., 2014, *ApJS*, 212, 8
- Savage B. D., Narayanan A., Lehner N., Wakker B. P., 2011, *ApJ*, 731, 14
- Savage B. D., Sembach K. R., 1991, *ApJ*, 379, 245
- Schaye J., 2001, *ApJ*, 559, 507
- Schaye J., Aguirre A., Kim T., Theuns T., Rauch M., Sargent W. L. W., 2003, *ApJ*, 596, 768
- Schaye J., Carswell R. F., Kim T., 2007, *MNRAS*, 379, 1169
- Schaye J., Rauch M., Sargent W. L. W., Kim T.-S., 2000, *ApJL*, 541, L1
- Schaye J., Theuns T., Rauch M., Efstathiou G., Sargent W. L. W., 2000, *MNRAS*, 318, 817
- Shapley A. E., Steidel C. C., Pettini M., Adelberger K. L., Erb D. K., 2006, *ApJ*, 651, 688
- Shen S., Madau P., Guedes J., Mayer L., Prochaska J. X., J. W., 2013, *ApJ*, 765, 89
- Shull J. M., 2014, *ApJ*, 784, 142
- Shull J. M., France K., Danforth C. W., Smith B., Tumlinson J., 2010, *ApJ*, 722, 1312
- Shull J. M., Moloney J., Danforth C. W., Tilton E. M., 2015, *arXiv150200637*
- Siana B., Teplitz H. I., Ferguson H. C., Brown T. M., Gialalisco M., Dickinson M., Chary R.-R. e. a., 2010, *ApJ*, 723, 241
- Simcoe R. A., Sargent W. L. W., Rauch M., 2004, *ApJ*, 606, 92
- Songaila A., 1998, *AJ*, 115, 2184
- Steidel C. C., Erb D. K., Shapley A. E., Pettini M., Reddy N., Bogosavljević M., Rudie G. C., Rakic O., 2010, *ApJ*, 717, 289
- Steidel C. C., Hamilton D., 1992, *AJ*, 104, 941
- Stocke J. T., Keeney B. A., Danforth C. W., Shull J. M., Froning C. S., Green J. C., Penton S. V., Savage B. D., 2013, *ApJ*, 763, 148
- Strickland D., Heckman T. M., 2009, *ApJ*, 697, 2030
- Strickland D. K., Heckman T. M., Colbert E. J. M., Hoopes C. G., Weaver K. A., 1998, *ApJ*, 606, 829
- Syphers D., Shull J. M., 2013, *ApJ*, 765, 119
- Theuns T., Leonard A., Efstathiou G., 1998, *MNRAS*, 297, L49
- Tumlinson J., Thom C., Werk J. K., Prochaska J. X., Tripp T. M., Weinberg D. H., Peebles M. S., O’Meara J. M., Oppenheimer B. D., Meiring J. D., Katz N. S., Davé R.,

Ford A. B., Sembach K. R., 2011, *Science*, 334, 948  
van de Voort F., Schaye J., Booth C. M., Haas M. R., Dalla  
Vecchia C., 2011, *MNRAS*, 414, 2458  
Wakker B. P., Savage B. D., 2009, *ApJS*, 182, 378  
Werk J. K., Prochaska J. X., Thom C., Tumlinson J., Tripp  
T. M., O’Meara J. M., Peebles M. S., 2013, *ApJS*, 204, 17  
Wiersma R. P. C., Schaye J., Dalla Vecchia C., Booth  
C. M., Theuns T., Aguirre A., 2010, *MNRAS*, 409, 132  
Wiersma R. P. C., Schaye J., Smith B. D., 2009, *MNRAS*,  
393, 99

## APPENDIX A: PREDICTIONS BY CLOUDY

Table A1. The tied H I+C IV components

QSO	$z_{\text{abs}}$	$b_{\text{H I}}$ (km s <sup>-1</sup> )	$\log N_{\text{H I}}$ [cm <sup>-2</sup> ]	$b_{\text{C IV}}$ (km s <sup>-1</sup> )	$\log N_{\text{C IV}}$ [cm <sup>-2</sup> ]	Temperature (K)	$b_{\text{nt}}$ (km s <sup>-1</sup> )	Notes
Q0055–269	3.257359	24.7±0.9	13.93±0.02	10.8±0.8	12.76±0.03	32860±3012	8±1	certain
Q0055–269	3.038795	22.3±1.2	14.60±0.04	14.4±1.4	12.72±0.04	19220±4373	13±2	certain
Q0055–269	2.744100	26.7±4.8	15.12±0.13	16.3±1.9	12.79±0.05	29830±17130	15±2	certain
Q0055–269	2.743720	24.2±10.1	14.78±0.39	8.8±2.3	12.48±0.09	33490±32600	6±6	uncertain
PKS2126–158	2.973015	23.8±0.2	14.36±0.01	12.5±0.7	12.18±0.03	27020±1355	11±1	certain
HS1425+6099	3.024719	21.8±1.0	14.75±0.04	11.2±2.0	12.11±0.06	23210±4140	10±3	certain
Q0636+6801	3.018604	28.9±14.8	13.97±0.31	14.7±2.7	12.29±0.06	41160±56860	13±5	uncertain
Q0420–388	2.849598	27.4±0.7	14.09±0.02	15.0±1.5	12.59±0.04	34780±3185	13±2	certain
Q0420–388	2.849229	32.7±1.6	13.68±0.06	12.3±2.9	12.10±0.10	60880±7971	8±5	uncertain
HE0940–1050	2.937755	25.2±0.3	14.58±0.02	9.7±0.4	12.65±0.02	35740±996	7±1	certain
HE0940–1050	2.937304	42.6±1.5	14.23±0.03	42.6±4.3	12.66±0.04	≤ 92	43±5	certain
HE0940–1050	2.883509	26.1±0.3	14.60±0.01	15.8±0.8	12.35±0.03	28560±2009	15±1	certain
HE0940–1050	2.826555	17.2±2.4	14.51±0.21	6.4±0.2	13.19±0.02	16840±5478	4±1	uncertain
HE2347–4342	2.787112	23.6±0.1	14.58±0.00	23.2±4.2	12.22±0.06	≤ 12880	23±5	uncertain
HE2347–4342	2.572434	29.0±0.2	15.02±0.01	9.2±3.4	11.88±0.12	49890±4252	4±9	uncertain
HE2347–4342	2.488605	34.4±0.6	14.81±0.01	11.9±0.8	12.52±0.02	68600±3143	7±2	certain
HE2347–4342	2.347467	23.6±1.3	15.99±0.20	9.7±0.1	13.49±0.00	30490±4035	7±0	certain
HE0151–4326	2.519825	26.1±0.5	15.24±0.02	10.2±1.1	12.29±0.04	38340±2344	7±2	certain
HE0151–4326	2.468096	22.9±1.0	12.84±0.02	6.6±0.1	12.96±0.01	31730±2820	0±0	certain
HE0151–4326	2.449902	13.6±0.3	14.45±0.02	5.5±0.2	12.99±0.01	10280±599	4±0	certain
HE0151–4326	2.419676	19.4±1.1	12.85±0.04	8.0±0.3	12.75±0.01	20570±2785	6±1	certain
HE0151–4326	2.415718	20.1±0.4	13.36±0.01	8.5±0.2	13.03±0.01	21850±963	6±0	certain
HE0151–4326	2.401315	33.7±0.7	15.04±0.02	10.7±1.4	12.34±0.11	67770±3127	4±4	certain
Q0002–422	2.539455	37.0±1.0	14.24±0.03	12.8±0.8	12.55±0.02	79970±4910	7±2	certain
Q0002–422	2.463222	23.6±2.8	14.56±0.06	10.3±0.5	13.26±0.01	29670±8781	8±1	certain
Q0002–422	2.462358	16.3±0.5	15.16±0.02	8.3±0.3	13.20±0.01	13020±1186	7±0	certain
Q0002–422	2.462044	18.1±0.3	14.83±0.02	10.1±0.7	13.34±0.02	14800±932	9±0	uncertain
PKS0329–255	2.587085	45.7±1.9	14.82±0.04	13.2±6.1	12.00±0.18	126700±22160	0±1	certain
PKS0329–255	2.586757	22.5±0.7	14.99±0.03	7.3±1.2	12.37±0.06	29980±2246	3±3	certain
PKS0329–255	2.456581	23.3±2.1	13.51±0.24	9.0±4.7	11.97±0.25	30640±9385	6±7	certain
PKS0329–255	2.456208	25.4±4.4	14.13±0.15	25.4±8.5	12.64±0.09	≤ 538	25±8	certain
Q0453–423	2.444109	13.0±0.4	14.62±0.01	5.2±0.7	12.63±0.06	9308±566	4±1	uncertain
Q0453–423	2.443509	21.4±4.2	14.14±0.14	8.5±0.2	13.38±0.01	25450±8891	6±1	uncertain
Q0453–423	2.442644	15.6±0.5	14.91±0.01	6.2±0.4	13.04±0.03	13500±796	5±1	uncertain
Q0453–423	2.441813	22.1±0.7	14.67±0.01	8.4±3.8	11.75±0.13	27670±3464	6±5	certain
Q0453–423	2.398159	19.0±1.9	13.39±0.07	11.7±1.1	12.74±0.04	14700±4761	11±1	uncertain
Q0453–423	2.397801	18.3±0.2	14.41±0.01	9.7±0.1	13.78±0.01	15860±595	9±0	uncertain
Q0453–423	2.397447	47.0±5.9	13.86±0.05	16.7±1.4	12.71±0.03	127500±36360	10±3	uncertain
Q0453–423	2.396755	19.0±0.6	14.16±0.03	6.9±0.1	13.34±0.01	20640±1491	4±0	certain
Q0453–423	2.277569	18.8±0.9	13.54±0.03	9.5±0.2	12.99±0.01	17540±2380	8±0	certain
Q0453–423	2.169936	59.1±1.9	13.30±0.02	17.7±2.2	12.27±0.04	210300±15510	5±9	certain
Q0453–423	2.169418	35.9±3.9	13.36±0.12	14.7±1.1	12.45±0.03	70900±18650	11±2	certain
HE1347–2457	2.370003	20.6±2.8	14.10±0.09	9.6±0.7	12.60±0.03	21860±7694	8±1	certain
Q0329–385	2.372835	75.7±0.8	14.66±0.02	21.9±4.6	12.38±0.09	347700±26610	0±0	certain
Q0329–385	2.363795	25.9±0.6	14.33±0.05	10.8±1.8	12.35±0.05	36870±3179	8±3	certain
Q0329–385	2.314255	22.7±0.8	13.68±0.03	6.6±1.1	12.29±0.05	31120±2825	0±0	certain
Q0329–385	2.313933	21.9±2.9	13.60±0.10	9.2±2.8	12.02±0.10	26240±8935	7±4	uncertain
Q0329–385	2.249389	18.0±2.7	12.90±0.10	14.1±2.3	12.40±0.06	8344±7476	14±3	certain
Q0329–385	2.248824	52.2±5.3	13.40±0.05	18.8±6.0	12.29±0.12	157100±42970	12±11	certain
Q0329–385	2.248307	8.5±4.1	12.21±0.31	8.5±2.3	12.29±0.12	≤ 385	8±3	certain
HE1122–1648	2.339275	26.7±0.1	14.26±0.00	8.1±1.5	11.81±0.06	42870±1645	3±5	certain
HE1122–1648	2.206364	23.4±0.9	14.86±0.04	11.1±0.9	12.13±0.03	27980±3005	9±1	certain
HE0001–2340	2.163416	24.2±0.5	14.64±0.02	8.2±6.0	11.89±0.22	34320±6670	4±12	certain
PKS1448–292	2.167959	24.2±1.6	13.26±0.05	7.0±3.0	11.86±0.14	35500±6438	0±1	certain

**Table A2.** Cloudy PIE prediction for the tied H I+C IV+C III components for the HM Q+G 2012 UVB

#	QSO	$z_{\text{abs}}$	Observed				$\log T_b$ [K]	Predicted							Notes <sup>a</sup>
			$\log N_{\text{H I}}$ [cm <sup>-2</sup> ]	$\log N_{\text{C IV}}$ [cm <sup>-2</sup> ]	$\log N_{\text{C III}}$ [cm <sup>-2</sup> ]	$\log N_{\text{C II}}$ [cm <sup>-2</sup> ]		$\log U$	$\log n_{\text{H}}$ [cm <sup>-3</sup> ]	[C/H]	$\log N_{\text{H}}$ [cm <sup>-2</sup> ]	$\log T_{\text{PIE}}$ [K]	$\log L$ [kpc]	$\log P/k$ [K cm <sup>-3</sup> ]	
1	Q0055-269	3.257359	13.93±0.02	12.76±0.03	12.54±0.06	≤ 12.30	4.517±0.040	-1.10±0.05	-5.01	-1.17±0.05	18.27	4.341	1.788	-0.306	Low
2	Q0055-269	3.038795	14.60±0.04	12.72±0.04	12.59±0.15	≤ 12.70	4.284±0.099	-1.20±0.10	-4.87	-1.77±0.08	18.90	4.427	2.283	-0.080	Low
3	Q0055-269	2.744100	15.12±0.13	12.79±0.05	12.98±0.06	bl <sup>b</sup>	4.475±0.249	-1.63±0.08	-4.39	-1.95±0.05	19.04	4.481	1.946	0.450	Low
4	Q0055-269	2.743720	14.78±0.39	12.48±0.09	12.27±0.19	bl <sup>b</sup>	4.525±0.422	-1.21±0.18	-4.81	-2.10±0.10	19.11	4.482	2.435	0.031	Low
5	PKS2126-158	2.973015	14.36±0.01	12.18±0.03	12.25±0.03	≤ 11.45	4.432±0.022	-1.40±0.05	-4.66	-1.95±0.05	18.50	4.474	1.672	0.178	Low
6	Q0420-388	2.849598	14.09±0.02	12.59±0.04	12.17±0.06	bl <sup>c</sup>	4.541±0.040	-1.07±0.08	-4.97	-0.95±0.05	18.08	4.393	1.558	-0.213	Low
7	Q0420-388	2.849229	13.68±0.06	12.10±0.10	11.89±0.14	bl <sup>c</sup>	4.784±0.057	-1.21±0.15	-4.83	-1.42±0.10	17.98	4.450	1.322	-0.016	Low
8	HE0940-1050	2.937755	14.58±0.02	12.65±0.02	12.51±0.01	≤ 11.95	4.553±0.012	-1.25±0.05	-4.80	-1.80±0.05	18.86	4.458	2.169	0.016	Low
9	HE0940-1050	2.883509	14.60±0.01	12.35±0.03	12.37±0.02	≤ 12.25	4.456±0.031	-1.39±0.05	-4.65	-2.03±0.05	18.76	4.483	1.923	0.192	Low
10	HE0940-1050	2.826555	14.51±0.21	13.19±0.02	13.23±0.03	≤ 12.00	4.226±0.141	-1.49±0.05	-4.54	-1.02±0.05	18.52	4.419	1.570	0.238	High, Si IV, comp
11	HE2347-4342	2.347467	15.99±0.20	13.49±0.00	13.26±0.22	≤ 11.75	4.484±0.057	-1.31±0.15	-4.67	-2.25±0.05	20.27	4.521	3.458	0.215	bl
12	HE0151-4326	2.519825	15.24±0.02	12.29±0.04	12.35±0.06	≤ 11.70	4.584±0.027	-1.55±0.08	-4.45	-2.60±0.05	19.26	4.507	2.219	0.423	Low
13	HE0151-4326	2.449902	14.45±0.02	12.99±0.01	12.96±0.04	≤ 12.20	4.012±0.025	-1.57±0.05	-4.42	-1.10±0.05	18.39	4.442	1.318	0.384	High, Si IV, comp
14	HE0151-4326	2.419676	12.85±0.04	12.75±0.01	12.76±0.02	bl <sup>d</sup>	4.313±0.059	-1.58±0.05	-4.41	0.55±0.05	16.29	3.785	-0.790	-0.260	High, simp
15	HE0151-4326	2.415718	13.36±0.01	13.03±0.01	13.07±0.02	bl <sup>d</sup>	4.339±0.019	-1.73±0.05	-4.26	0.35±0.05	16.77	3.955	-0.459	0.057	High, simp
16	HE0151-4326	2.401315	15.04±0.02	12.34±0.11	12.37±0.06	bl <sup>e</sup>	4.831±0.020	-1.58±0.15	-4.41	-2.35±0.05	19.03	4.507	1.947	0.463	Low
17	Q0002-422	2.539455	14.24±0.03	12.55±0.02	12.18±0.06	≤ 11.95	4.903±0.027	-1.15±0.05	-4.85	-1.45±0.05	18.62	4.480	1.983	-0.006	Low
18	Q0002-422	2.463222	14.66±0.06	13.26±0.01	13.38±0.02	≤ 11.75	4.472±0.128	-1.79±0.05	-4.20	-0.77±0.05	18.24	4.364	0.949	0.524	High, Si IV, comp
19	Q0002-422	2.462358	15.16±0.02	13.20±0.01	13.83±0.03	12.60±0.03	4.115±0.040	-2.46±0.05	-3.53	-0.45±0.05	18.04	4.193	0.084	1.016	High, Si IV, comp, error
20	Q0002-422	2.462044	14.83±0.02	13.34±0.02	13.59±0.02	12.19±0.08	4.170±0.027	-2.25±0.10	-3.74	-0.45±0.10	17.92	4.228	0.172	0.844	High, Si IV, comp, no
21	PKS0329-255	2.586757	14.99±0.03	12.37±0.06	12.02±0.11	≤ 11.90	4.477±0.033	-1.15±0.10	-4.85	-2.40±0.05	19.39	4.493	2.753	0.003	Low
22	PKS0329-255	2.456581	13.51±0.24	11.97±0.25	12.00±0.29	≤ 12.30	4.486±0.133	-1.59±0.30	-4.40	-1.15±0.25	17.43	4.447	0.342	0.409	Low
23	Q0453-423	2.444109	14.62±0.01	12.63±0.06	13.41±0.08	12.66±0.11 <sup>f</sup>	3.969±0.026	-2.65±0.10	-3.34	0.10±0.10	17.13	3.932	-1.022	0.944	High, Si IV, comp, no
24	Q0453-423	2.442644	14.91±0.01	13.04±0.03	13.66±0.07	12.18±0.07	4.130±0.026	-2.32±0.05	-3.67	-0.55±0.10	17.95	4.243	0.132	0.930	High, Si IV, comp, error
25	Q0453-423	2.441813	14.67±0.01	11.75±0.13	11.83±0.14	≤ 11.65	4.442±0.054	-1.58±0.20	-4.41	-2.55±0.20	18.68	4.510	1.600	0.462	Low
26	Q0453-423	2.398159	13.39±0.07	12.74±0.04	11.69±0.25	≤ 12.05	4.167±0.141	-0.62±0.10	-5.37	-0.25±0.15	18.21	4.370	2.088	-0.634	Low
27	Q0453-423	2.397801	14.41±0.01	13.78±0.01	13.16±0.02	≤ 11.70	4.200±0.016	-1.08±0.05	-4.91	-0.35±0.05	18.77	4.367	2.188	-0.177	Low
28	Q0453-423	2.397447	13.86±0.05	12.71±0.03	12.25±0.09	≤ 11.80	5.106±0.124	-1.13±0.08	-4.86	-0.85±0.05	18.23	4.441	1.596	-0.053	Low
29	Q0453-423	2.396755	14.16±0.03	13.34±0.01	13.06±0.04	≤ 11.60	4.315±0.031	-1.42±0.05	-4.57	-0.50±0.05	18.17	4.359	1.254	0.154	High, Si IV, comp
30	Q0453-423	2.277569	13.54±0.03	12.99±0.01	13.05±0.05	bl <sup>g</sup>	4.244±0.059	-1.86±0.05	-4.12	0.20±0.05	16.88	4.038	-0.488	0.277	High, Si IV, simp/comp
31	HE1347-2457	2.370003	14.10±0.09	12.60±0.03	12.33±0.04	≤ 11.55	4.340±0.153	-1.30±0.05	-4.68	-1.20±0.05	18.33	4.480	1.528	0.157	Low
32	Q0329-385	2.249389	12.90±0.10	12.40±0.06	12.30±0.34	≤ 12.55	3.921±0.389	-1.74±0.07	-4.24	0.08±0.30	16.43	4.136	-0.820	0.257	High, simp/comp

<sup>a</sup> *High*: high-metallicity branch absorbers. *Low*: low-metallicity branch absorbers. *blank*: not classified. *Si IV*: associated Si IV is detected. *bl*: Si IV region is blended. *comp*: part of a multi-component C IV complex. *simp*: high-metallicity branch absorbers with a simple, isolated C IV. *simp/comp*: simple high-metallicity branch absorbers close to a separate C IV complex. *error*: the predicted column densities are within the observed errors. *no*: no single  $U$  matches all the observed column densities within errors.

<sup>b</sup> A weak H I Ly $\alpha$  absorption at  $z = 3.109959$  exists at  $-16$  km s<sup>-1</sup>, while C II  $\lambda$  1334 is expected at  $-30$  km s<sup>-1</sup> and 0 km s<sup>-1</sup>. At  $-30$  km s<sup>-1</sup> and 0 km s<sup>-1</sup>, a negligible absorption is due to the wing of the aforementioned H I. Therefore, C II  $\lambda$  1334, if exists, would be very weak.

<sup>c</sup> At the expected C II  $\lambda$  1334 position, an absorption feature by Si IV  $\lambda$  1402 at  $z = 2.662123$  and at  $z = 2.662294$  exists, while C II  $\lambda$  1036 is blended. Since the Si IV  $\lambda\lambda$  1393, 1402 doublet falls on the absorption-free region without any hint of additional absorption features, C II  $\lambda$  1334, if exists, would be very weak.

<sup>d</sup> Despite the normalised flux being less than 1, the expected C II  $\lambda$  1334 spectral region is flat, which does not suggesting any additional absorption feature.

<sup>e</sup> Both C II  $\lambda\lambda$  1334, 1036 regions are severely blended.

<sup>f</sup> The column density of C II is from C II  $\lambda$  1036 in an absorption-free region.

<sup>g</sup> At the expected position of C II  $\lambda$  1334, a narrow absorption feature exists, but it over-produces a C II  $\lambda$  1036 absorption which is located in a region deblended reliably. In addition, this narrow feature occurs at  $+3$  km s<sup>-1</sup> away from its supposed position, it is likely to be a unidentified metal line.

**Table A3.** Non-PIE Cloudy-prediction for the tied H I+C IV+C III components for the HM Q+G 2012 UVB at a fixed temperature

#	QSO	$z_{\text{abs}}$	Observed					Predicted							Notes <sup>b</sup>
			$\log N_{\text{H I}}$ [cm <sup>-2</sup> ]	$\log N_{\text{C IV}}$ [cm <sup>-2</sup> ]	$\log N_{\text{C III}}$ [cm <sup>-2</sup> ]	$\log N_{\text{C II}}^{\text{a}}$ [cm <sup>-2</sup> ]	$\log T_{\text{b}}$ [K]	$\log U$	$\log n_{\text{H}}$ [cm <sup>-3</sup> ]	[C/H]	$\log N_{\text{H}}$ [cm <sup>-2</sup> ]	$\log L$ [kpc]	$\log P/k$ [K cm <sup>-3</sup> ]		
1	Q0055–269	3.257359	13.93±0.02	12.76±0.03	12.54±0.06	≤ 12.30	4.517±0.040	-0.92±0.05	-5.19	-1.20±0.05	18.59	2.284	-0.309	Low	
2	Q0055–269	3.038795	14.60±0.04	12.72±0.04	12.59±0.15	≤ 12.70	4.284±0.099	-1.36±0.05	-4.71	-1.70±0.10	18.64	1.854	-0.065	Low	
3	Q0055–269	2.744100	15.12±0.13	12.79±0.05	12.98±0.06	bl	4.475±0.249	-1.62±0.05	-4.40	-1.95±0.05	19.05	1.960	0.434	Low	
4	Q0055–269	2.743720	14.78±0.39	12.48±0.09	12.27±0.19	bl	4.525±0.422	-1.18±0.20	-4.84	-2.10±0.10	19.18	2.531	0.045	Low	
5	PKS2126–158	2.973015	14.36±0.01	12.18±0.03	12.25±0.03	≤ 11.45	4.432±0.022	-1.44±0.05	-4.62	-1.95±0.05	18.43	1.557	0.174	Low	
6	Q0420–388	2.849598	14.09±0.02	12.59±0.04	12.17±0.06	bl	4.541±0.040	-0.93±0.05	-5.11	-1.35±0.05	18.75	2.367	-0.205	Low	
7	Q0420–388	2.849229	13.68±0.06	12.10±0.10	11.89±0.14	bl	4.784±0.057	-1.03±0.10	-5.01	-1.45±0.15	18.50	2.012	0.140		
8	HE0940–1050	2.937755	14.58±0.02	12.65±0.02	12.51±0.01	≤ 11.95	4.553±0.012	-1.14±0.05	-4.91	-1.80±0.05	19.05	2.470	0.003	Low	
9	HE0940–1050	2.883509	14.60±0.01	12.35±0.03	12.37±0.02	≤ 12.25	4.456±0.031	-1.42±0.05	-4.62	-2.00±0.05	18.70	1.840	0.193	Low	
10	HE0940–1050	2.826555	14.51±0.21	13.19±0.02	13.23±0.03	≤ 12.00	4.226±0.141	-1.69±0.05	-4.34	-0.85±0.05	18.17	1.024	0.241	High, Si IV, comp	
11	HE2347–4342	2.347467	15.99±0.20	13.49±0.00	13.26±0.22	≤ 11.75	4.484±0.057	-1.35±0.15	-4.63	-2.25±0.05	20.20	3.345	0.212	bl	
12	HE0151–4326	2.519825	15.24±0.02	12.29±0.04	12.35±0.06	≤ 11.70	4.584±0.027	-1.51±0.10	-4.49	-2.65±0.05	19.39	2.380	0.459	Low	
13	HE0151–4326	2.449902	14.45±0.02	12.99±0.01	12.96±0.04	≤ 12.20	4.012±0.025	-1.73±0.05	-4.26	-0.85±0.05	17.91	0.675	0.112	High, Si IV, comp	
14	HE0151–4326	2.419676	12.85±0.04	12.75±0.01	12.76±0.02	bl	4.313±0.059	-1.75±0.05	-4.24	0.40±0.05	16.51	-0.748	0.438	High, simp	
15	HE0151–4326	2.415718	13.36±0.01	13.03±0.01	13.07±0.02	bl	4.339±0.019	-1.74±0.05	-4.25	0.20±0.05	17.05	-0.197	0.454	High, simp	
16	HE0151–4326	2.401315	15.04±0.02	12.34±0.11	12.37±0.06	bl	4.831±0.020	-1.49±0.05	-4.50	-2.60±0.10	19.60	2.602	0.696	Low	
17	Q0002–422	2.539455	14.24±0.03	12.55±0.02	12.18±0.06	≤ 11.95	4.903±0.027	-1.08±0.05	-4.92	-1.55±0.05	19.18	2.612	0.347	Low	
18	Q0002–422	2.463222	14.56±0.06	13.26±0.01	13.38±0.02	≤ 11.75	4.472±0.128	-1.65±0.05	-4.34	-0.85±0.05	18.45	1.300	0.493	High, Si IV, comp	
19	Q0002–422	2.462358	15.16±0.02	13.20±0.01	13.83±0.03	12.60±0.03	4.115±0.040	-2.46±0.05	-3.53	-0.40±0.05	17.97	0.017	0.937	High, Si IV, comp, error	
20	Q0002–422	2.462044	14.83±0.02	13.34±0.02	13.59±0.02	12.19±0.08	4.170±0.027	-2.23±0.10	-3.76	-0.45±0.05	17.91	0.180	0.766	High, Si IV, comp, no	
21	PKS0329–255	2.586757	14.99±0.03	12.37±0.06	12.02±0.11	≤ 11.90	4.477±0.033	-1.18±0.10	-4.82	-2.40±0.05	19.34	2.679	0.015	Low	
22	PKS0329–255	2.456581	13.51±0.24	11.97±0.25	12.00±0.29	≤ 12.30	4.486±0.133	-1.54±0.30	-4.45	-1.20±0.30	17.52	0.476	0.398		
23	Q0453–423	2.444109	14.62±0.01	12.63±0.06	13.41±0.08	12.66±0.11	3.969±0.026	-2.73±0.10	-3.26	0.20±0.10	17.07	-1.162	1.060	High, Si IV, comp, no	
24	Q0453–423	2.442644	14.91±0.01	13.04±0.03	13.66±0.07	12.18±0.07	4.130±0.026	-2.27±0.10	-3.72	-0.50±0.10	17.92	0.149	0.768	High, Si IV, comp, error	
25	Q0453–423	2.441813	14.67±0.01	11.75±0.13	11.83±0.14	≤ 11.65	4.442±0.054	-1.66±0.20	-4.33	-2.50±0.15	18.52	1.359	0.475	Low	
26	Q0453–423	2.398159	13.39±0.07	12.74±0.04	11.69±0.25	≤ 12.05	4.167±0.141	-0.77±0.15	-5.22	-0.35±0.05	17.91	1.637	-0.687		
27	Q0453–423	2.397801	14.41±0.01	13.78±0.01	13.16±0.02	≤ 11.70	4.200±0.016	-1.21±0.05	-4.78	-0.35±0.05	18.52	1.804	-0.214		
28	Q0453–423	2.397447	13.86±0.05	12.71±0.03	12.25±0.09	≤ 11.80	5.106±0.124	-1.67±0.05	-4.32	-1.50±0.20	18.96	1.784	1.152	Low	
29	Q0453–423	2.396755	14.16±0.03	13.34±0.01	13.06±0.04	≤ 11.60	4.315±0.031	-1.46±0.05	-4.53	-0.47±0.05	18.11	1.140	0.149	High, Si IV, comp	
30	Q0453–423	2.277569	13.54±0.03	12.99±0.01	13.05±0.05	bl	4.244±0.059	-1.87±0.05	-4.11	0.10±0.05	17.02	-0.358	0.494	High, Si IV, simp/comp	
31	HE1347–2457	2.370003	14.10±0.09	12.60±0.03	12.33±0.04	≤ 11.55	4.340±0.153	-1.45±0.05	-4.53	-1.15±0.05	18.07	1.116	0.167	Low	
32	Q0329–385	2.249389	12.90±0.10	12.40±0.06	12.30±0.34	≤ 12.55	3.921±0.389	-1.62±0.10	-4.36	0.10±0.30	16.39	-0.734	-0.079	High, simp/comp	

<sup>a</sup> See Table A2 on  $N_{\text{C II}}$ .<sup>b</sup> See Table A2 for notes.